Analysis of Quasar Images

The Luminosity Function of AGN Host Galaxies

Dissertation
zur Erlangung des Doktorgrades
des Fachbereichs Physik
der Universität Hamburg

vorgelegt von
Björn Kuhlbrodt
aus Hamburg

Hamburg, 2003

Gutachter der Dissertation:	PD Dr. Lutz Wisotzki
	Prof. Dr. Dieter Reimers
Gutachter der Disputation:	Prof. Dr. Dieter Reimers
	Prof. Dr. Peter Hauschildt
Datum der Disputation:	26. Juni 2003
Vorsitzender des Prfungsausschusses:	Dr. habil. Franz-Josef Zickgraf
Vorsitzender des Promotionsausschusses:	Prof. Dr. Roland Wiesendanger
Dekan des Fachbereichs Physik:	Prof. Dr. Günter Huber

Abstract

In the current standard model a quasar is a massive black hole which accretes matter and resides in the centre of a galaxy. Thus the analysis of host galaxies is a key issue in understanding the quasar phenomenon. But it is often complicated by the presence of the quasar which can practically outshine the galaxy.

To tackle this task, an algorithm has been developed to decompose quasar images, taken in the optical and near-infrared wavebands, into nuclear and host galaxy components. Key features of the method are: (semi-)analytic representation of a possibly spatially variable point-spread function; full two-dimensional convolution of the model galaxy using gradient-controlled adaptive subpixelling; multiple iteration minimization scheme. The code is computationally efficient and versatile for a wide range of applications. The quantitative performance is measured by analysing simulated imaging data.

This method is applied to several complete samples of quasars in order to investigate host galaxy properties and their relation to nuclear properties. Two samples are presented in detail: a set of 12 nearby Seyfert galaxies and a sample of 44 quasars at redshifts $z < 0.35$. Both samples are drawn from the Hamburg/ESO-Survey. In both samples quasars radiate below 10% of the maximum Eddington luminosity and reside predominantly ($\gtrsim 60$ %) in disk-like galaxies. For the Seyfert samples, the rate of tidal interaction is suspiciously high.

In order to assess the properties of the quasar host galaxy population, the concept of luminosity functions – established for quasar and galaxies – is extended onto host galaxies and a bivariate quasar/host galaxy luminosity function. With this innovative and versatile approach, dependencies between quasar and the host galaxy can easily be implemented. Several such dependencies are tested with two samples of altogether 110 low to medium redshift quasars. Only weak indication for dependencies other than Eddington limit are found. The recovered host galaxy luminosity function greatly resembles a scaled field galaxy luminosity function with the exception that fewer host galaxies are found at the faint end. From the fraction of host galaxies to field galaxies, the minimal dutycylce of a quasar can be estimated to be 2 Myr $\lesssim t_{\rm accr} \lesssim$ 40 Myr.

Finally, for high-redshift quasar a new algorithm to evaluate possible host galaxy detections made with adaptive optics in the near-infrared is presented. Instead of concentrating on point spread function (PSF) removal, the fluctuations of the PSF are investigated and mapped. The PSFs underlying the object images can be described by a statistical approach and simulated objects created which are matched to the different atmospheric conditions. It is shown that a single host galaxy model adequately can represent the distribution of individual object images. Three bright quasars at $z \sim 2.2$ were subjected to the statistical analysis procedure resulting in host galaxy detection together with simultaneous rejection of the non-detection case for all objects. The hosts are bright with a mean absolute magnitude of $R = -27.2$, and have scale lengths amounting to typically $4-7$ kpc.

Zusammenfassung

Nach gegenwärtigem Standardmodell bestehen Quasare aus einem massiven Schwarzen Loch, das Materie absorbiert und sich in der Mitte einer Galaxie befindet. Die Untersuchung dieser Host(Mutter)-Galaxien nimmt eine Schlüsselposition zum Verständnis der Quasare ein. Erschwert wird sie häufig durch den Quasar selbst, da dieser die Galaxie praktisch überstrahlen kann.

Für diese Aufgabe wurde ein Algorithmus entwickelt, der optische und nah-infrarote Quasarbilder in Kern- und Galaxienkomponenten zerlegt. Wesentliche Eigenschaften der Methode sind: Eine (semi-)analytische Darstellung der gegebenenfalls räumlich variablen Abbildungsfunktion, eine vollständige zweidimensionale Faltung des Modells unter Verwendung einer Gradienten-kontrollierten Pixel-Unterteilung und ein iteratives Minimierungsschema. Der Programmcode ist auf Geschwindigkeit optimiert und für eine Vielzahl von Anwendungen nutzbar. Die Genauigkeit der Anpassung wird mit simulierten Bilddaten gemessen.

In der vorliegenden Arbeit wird die Methode auf mehrere vollständige Datensätze von Quasaren angewandt, um die Eigenschaften von Host-Galaxien und ihre Beziehung zu Quasareigenschaften zu bestimmen. Zwei Datensätze werden detailliert vorgestellt: Ein Satz von zwölf nahen Seyfert-Galaxien und ein Satz von 44 Quasaren mit Rotverschiebungen bis zu $z = 0.35$, beide dem Hamburg/ESO-Survey entnommen. Die Quasarkerne beider Datensätzen strahlen mit weniger als der maximalen (Eddington-)Leuchtkraft und befinden sich hauptsächlich ($\gtrsim 60$ %) in Scheibengalaxien. Unter den Seyfert-Galaxien findet sich eine hohe Rate an Interaktion zu nahen Galaxien.

Um auf die Eigenschaften der Host-Galaxien-Population zugreifen zu können, wird das Konzept der Leuchtkraftfunktionen – gebräuchlich unter anderem bei Galaxien und Quasaren – auf die Host-Galaxien und auf eine bi-variate Quasar/Host-Galaxien-Leuchtkraftfunktion erweitert. Mit diesem neuartigen und vielseiten Ansatz können Abhängigkeiten zwischen Quasar und Galaxie einfach berücksichtigt werden. Mehrere solcher Abhängigkeiten werden an zwei Datensätzen mit zusammen 110 Quasaren getestet. Für Abhängigkeiten, die nicht durch durch das Eddington-Limit verursacht werden, werden nur schwache Anzeichen gefunden. Die berechnete Host-Galaxien-Leuchtkraftfunktion ähnelt stark einer herabskalierten Leuchtkraftfunktion inaktiver Feldgalaxien, mit der Ausnahme, dass am schwachen Ende weniger Host-Galaxien gefunden werden. Aus dem Verhältnis von Feld- zu Host-Galaxien kann die minimale Lebenszeit eines Quasars mit 2 Myr $\lesssim t_{\rm accr} \lesssim$ 40 Myr abgeschätzt werden.

Für hoch-rotverschobene Quasare wird schließlich ein neuer Algorithmus vorgestellt, mit dem Host-Galaxienbilder, die mit adaptiver Optik im nahen Infraroten gemacht wurden, analysiert werden können. Anstatt sich auf die Entfernung der Punktquelle zu konzentrieren, wird die Fluktuation der Abbildungsfunktion untersucht. Die Abbildungsfunktion die den Quasarbildern zugrunde liegt, wird mit diesem statistischen Ansatz beschrieben und simulierte Bilder für die veränderlichen Beobachtungsbedingungen werden erzeugt. Mit *einem* Host-Galaxien-Modell kann auf diese Weise die ganze Bandbreite beobachteter Bilder dargestellt werden. Für drei helle Quasare mit $z \approx 2.2$ wurde diese statistische Analyse durchgeführt. Für alle konnten Host-Galaxien nachgewiesen werden bei gleichzeitiger Rückweisung der Null-Hypothese. Die Host-Galaxien sind hell mit einer mittleren absoluten Leuchtkraft von $R = -27.2$ und haben Skalenlängen von $4-7$ kpc.

Contents

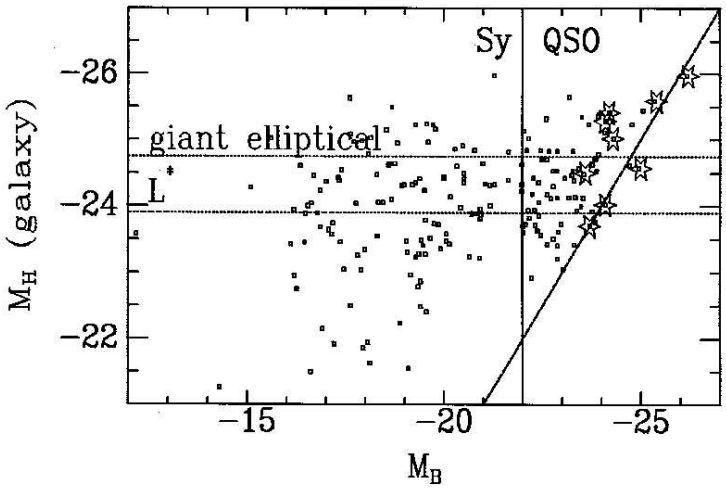

Figure 1.1. Quasar nuclear versus galactic luminosity. No objects are found in a triangular area, though technically possible. The boundary is a line of proportionality between nucleus and host galaxy luminosity. Figure taken from McLeod & Rieke (1995a)

1 Introduction

Quasars are some of the most interesting objects in astronomy. Ever since their detection in 1963 it was clear that they can emit massive amounts of energy – more than any previously known object. But the range of luminosities is large: We now know of quasars with luminosities as low as $M_B = -9.8$ (Filippenko & Sargent 1989) and can find quasars with $M_B < -28$ (e.g. Wisotzki et al. 2000), over 10^7 times brighter than the faintest known quasars. The physical size of the energy source is small, so small that it cannot be resolved with optical instruments, excludin nuclear fusion as the engine for high-luminosity quasars. Already in 1963 gravitational collapse on a massive object was suggested as engine (Hoyle & Fowler 1963). Later Shields (1978) proposed an accretion disk of a supermassive black hole as source of the quasar continuum. From similarities in spectra, colours and variabilities between quasars and Seyfert galaxies – a long known class of galaxies with 'active', i.e. unusually bright nuclei – Kristian (1973) concluded that quasars are events in the nuclei of galaxies. Support for this theory came 1978, when Morton et al. (1978) and Green et al. (1978) found stellar emission lines around quasars.

Our current standard view of quasars is well described by the unified model by Antonucci (1993). In his model quasars are composed of a central massive black hole residing in the centre of a galaxy. Infalling matter creates an accretion disk around the black hole, which is the source of the continuum. A dust torus surrounds both and obscures the accretion disk depending on the viewing angle. This viewing angle defines what class of 'active galaxy nucleus (AGN)' we see: An AGN type 1 if we see the accretion disk, type 2 if it is hidden and a variety of other classes which for the understanding of this work are not important.

In this model the only difference between a quasar and a Seyfert 1 galaxy is the luminosity. The distinction between both classes is now merely done for historical reason, the transition between quasars and Seyferts is continuous. In this work, both classes will hence be labelled 'quasar'. To emphasise the difference between the quasar and the host galaxy I will also frequently use the term 'nucleus' which refers to the *active* nucleus, the quasar.

The (active) nucleus and the host galaxy are not independent from each other as McLeod & Rieke (1995a) found. Though technically possible they failed to detect bright quasar nuclei in faint galaxies (see Figure 1.1). They conclude that 'there appears to be a linear relation between

nucleus and the minimum host galaxy magnitude' ('McLeod Boundary' in this work). But it must be noted that the Palomar Bright Quasar Survey (BQS Schmidt & Green 1983), which was the basis of the two most critical samples, was shown to be essentially incomplete and misses low-redshift high-luminosity quasars (Köhler et al. 1997). A selection effect is therefore possible. Also their result has been challenged lately by Percival et al. (2001), who find a number of objects, *below* the boundary, i.e. with nuclei *brighter* than allowed by the McLeod boundary, but it is not clear if this effect is real.

In favour for the McLeod boundary is a physical model for the quasar: The luminosity and the mass of the spheroidal part[1] of the galaxy are coupled with the mass-to-light ratio (e.g. Jørgensen et al. 1996). The mass of the spheroid and the black hole mass were found to be correlated (Magorrian et al. 1998) and finally the mass of a black hole and the *maximum* luminosity at which it can radiate before radiation pressure halts the accretion are correlated via the Eddington ratio. The maximum luminosity of a black hole is often called 'Eddington Luminosity' or $L_{\rm edd}$. All this leads to a chain of proportionalities:

$$L_{\rm spher} \propto \mathcal{M}_{\rm spher} \propto \mathcal{M}_{\rm BH} \propto L_{nuc,max} \tag{1.1}$$

As quasars radiating at super-Eddington rates are known (for a discussion see Collin et al. 2002), confirmation of the McLeod boundary is essential to understand the physical principles of the quasar engine. To test this, a view at Figure 1.1 reveals that the most critical objects are bright quasars. To achieve a significant result, a large, complete sample of bright quasars is essential.

Samples like this are most conveniently picked from well defined and flux limited quasars surveys. Quasar surveys which require a point-like appearance of optical images are for example biases against low-redshift quasars where the host galaxy becomes visible. The Hamburg-ESO-Survey (HES; Wisotzki et al. 2000) avoids some of the most notorious selection effects by using low-resolution objective-prism spectra independent from host galaxy properties. In this work samples are mainly selected from the HES consequently selection effects and biasing against low-redshift objects are avoided.

Having unbiased samples, care must be taken to apply unbiased means of analysis. This work features the detailed description of an unbiased, robust and reasonably fast method to decompose images of quasars at various redshifts taken with different instruments into images of the nuclear and galactic parts. This is not a trivial task. Figure 1.2 shows a typical quasar (HE 0956–0720) with a nucleus thirteen times brighter that the host galaxy, not unusual for bright quasars.

To disentangle nuclear and galactic light currently two method are in use: decomposition and deconvolution. In the decomposition two-dimensional models (such as in Figure 1.2, bottom row) are fitted to the quasar image. Deconvolution tries to undo the convolution of the quasar images with the point-spread-function (PSF) which spreads the initially point-like quasar nucleus image due to atmospheric and instrumental widening. This is done in in Figure 1.2, top row, for two different numbers of iterations, i.e. up to a certain final width of the PSF. The further the width is reduced, the more artifacts will occur. In the algorithm of Lucy (1974) the most prominent artifact is 'ringing', seen in Figure 1.2 in the $i = 20$ image.

Deconvolution in the presence of noise is mathematically an ill-posed problem. A number of methods which successfully deal with this problem exist (see Starck et al. 2002, for a review),

[1] I.e. the bulge in spiral galaxies or the entire elliptical galaxy.

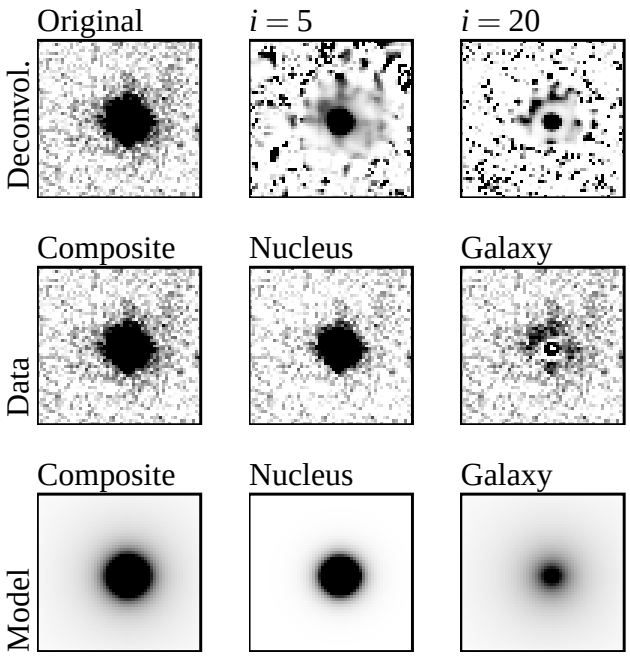

Figure 1.2. Example decomposition of a $z = 0.6$ quasar. In the middle row we show the composite data and the single components after subtraction of the model of the other component. In the bottom row we show the models used. The quasar is almost point-like to the naked eye, but can be decomposed reliably which will be shown in this work. The top-row features deconvolutions of the image at different iteration levels *i* using ESO-MIDAS implementation of the algorithm by Lucy (1974).

but yet no method which is able to deconvolve a point-source within an extended source has established which is fast, robust, flux-conserving, does not produce artifacts and requires only few user interventions. Furthermore, if such a method existed, we still would have to separate nuclear and galactic light, since the resolution after a deconvolution is still final (see Magain et al. 1998, for a detailed discussion), though much better than before.

Decomposition of the images on the other hand can – and will – be shown to be able to recover the host galaxy parameters even for such unfavourable objects like shown in Figure 1.2. Even though the residual images can show artifacts, recovered fluxes and radii are unbiased.

Once nucleus and galaxy are separated, properties of nucleus and galaxy can be compared as done in Figure 1.1. By subtracting the nucleus from the quasar image, we have galaxy images which are undisturbed by the nuclear light (but may contain artifacts in the central few pixels) and can hence easily be classified or compared to those of inactive galaxies. With these information it can investigated if luminous quasars reside predominantly in elliptical galaxies (Bahcall et al. 1997; Boyce et al. 1998; McLure et al. 1999; Dunlop et al. 2003) or if there is a large fraction of disk-like galaxies (McLeod & McLeod 2001; Percival et al. 2001) hosting luminous nuclei.

It is also important to search the galaxy images for deviations from the ideal light distribution. Asymmetries, multiple nuclei, tidal wisps and the like are indicators of ongoing or recent tidal interaction which play an important role in theories of the black hole feeding mechanism. If the triggering of quasars is done by major (Cattaneo 2001; Kauffmann & Haehnelt 2000) oder minor merger (Hernquist & Mihos 1995), signs of them should be visible, though Corbin (2000) did not find higher rates of asymmetries in quasar host galaxies in a comparative study of active and inactive local galaxies.

To answer the question which galaxies are able to host a quasar, we need to know the properties of the *population* of quasar host galaxies, derived from a *complete* sample in order to make general statements. If we have a complete sample of quasars with images decomposed in an unbiased fashion, we can compute the luminosity function of quasar host galaxies and compare

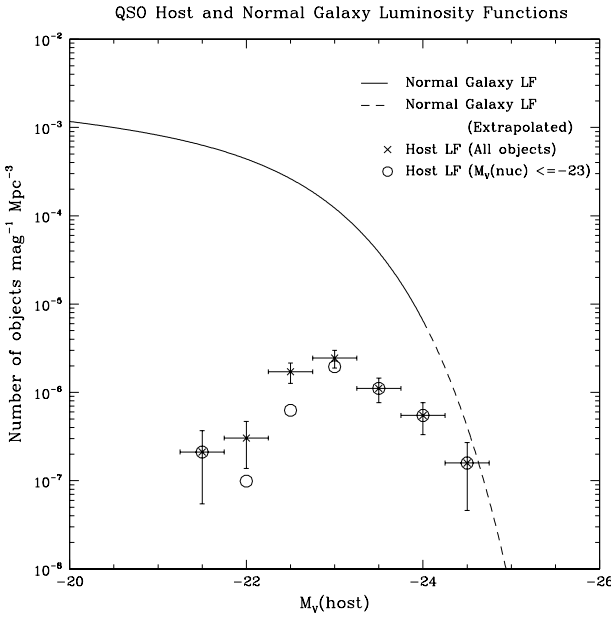

Figure 1.3. The quasar host galaxy luminosity function from Hamilton et al. (2002) (data points) and the normal field galaxy LF from Metcalfe et al. (1998). Note that *all* galaxies seem to have a quasar.

this to the field galaxy population.

Such a host galaxy luminosity function has already been computed by Hamilton et al. (2002) (Figure 1.3). They find that the (extrapolated) luminosity function of active and inactive galaxy *cross* at high-luminosity galaxies. This implies that *all* bright galaxies have a quasar. Furthermore, with the argument 'ensemble average = time average' the quasar dutycycle can be computed, which in this case means: Quasars in bright galaxies are turned on *permanently*. This result, if confirmed, would dramatically constrain models of the growth of black holes. Hamilton et al. however did not have a complete sample but used a complicated correction.

We plan to extend this concept to a bi-variate quasar/host galaxy luminosity function in which dependencies between galaxy and nucleus such as the McLeod boundary can easily be implemented. With a complete sample and an unbiased decomposition method, we can test the claim by Hamilton et al. and look for relations between quasar luminosity and host galaxy properties in the low-redshift regime, where host galaxy imaging is well-established.

In the high-redshift regime ($z > 2$) the situation is more complex. Detailed analysis of hosts at these redshifts requires both deep and highly resolved images. Even then, detections are often marginal. In the few, small samples investigated so far, host galaxies have luminosities from a few L^* (Kukula et al. 2001; Ridgway et al. 2001; Hutchings et al. 2002) up to $15 - 45L^*$ (Aretxaga et al. 1998,?; Lehnert et al. 1992) and seem generally more compact than present-day hosts (Falomo et al. 2001; Ridgway et al. 2001; Aretxaga et al. 1998). These are valuable inputs to any evolution model for both galaxies and quasars.

Here, the technique of adaptive optics shows an improvement over traditional imaging in combining resolution and light-gathering power. But the number of sources available to AO is small, as a bright guide star close to quasar is required for all systems. Probing quasar catalogues for suitable pairs of a high-redshift quasars and a guides star will therefore extend the available sample significantly.

The goal of this work is to develop a set of methods to analyse quasar images in a robust and unbiased way in order to address several questions:

- What is the influence of the PSF on the standard 2d-modelling approach of quasar image decomposition?
- Are there quasars beyond the McLeod boundary?
- Does the host galaxy Hubble type depend on quasar luminosity?
- What is the luminosity function of quasar host galaxies?
- Is there a relation between quasar nucleus and galaxy properties except the McLeod boundary?
- What is the dutycycle of quasars?
- What are the properties of high-redshift quasar host galaxies?

In Chapter 2 a method to decompose quasar images into nuclear and multiple galaxy components will be described in detail. I will also show that the influence of the PSF on the reconstruction of the host galaxy is larger then previously assumed. A special emphasis will therefore be put on the determination of the PSF.

This method will be used in Chapter 3 to analyse a sample of relatively nearby Seyfert galaxies with respect to various interests. As the sample is small ($N = 13$), this was mostly intended as a first test and demonstration of the decomposition method, but it is also suitable to give constraints on the properties of local quasars.

A larger sample of bright quasars with redshifts $z < 0.35$, selected to test the McLeod boundary, is presented in Chapter 4. This sample is also the basis of the luminosity function analysis.

Two other works which made use of the method are briefly described in Chapter 5.

The computation of the luminosity function of quasars and their host galaxies is finally the topic of Chapter 6. Here, we will also give a solid lower boundary for the quasar dutycycle.

Finally, an analysis of high-redshift quasar images and unforeseen problems are described in Chapter 7.

2 Decomposition of quasar images

2.1 Introduction

The properties of black holes in galactic nuclei are probably closely linked to the global properties of the galaxies in which they reside. Fuelling these black holes leads to the AGN and quasar phenomenon; investigating AGN host galaxies for various degrees of AGN activity is therefore a necessary step to understand the physical links, and the role of AGNs in galaxy evolution. Because of the high luminosities of the central region – being effectively a point source in optical and near-infrared wavelengths – which often outshines the entire galaxy, quantitative study of quasar hosts is fraught with technical difficulties. New instrumentation has made this task somewhat more feasible. In particular HST with its high spatial resolution has contributed significantly to the study of quasar hosts both at low redshifts (McLure et al. 1999; Schade, Boyle & Letawsky 2000; McLeod & McLeod 2001) and in the early universe (Kukula et al. 2001; Ridgway et al. 2001; Lehnert et al. 1999). However, ground-based imaging under excellent conditions will remain to be competitive, especially with the new 8–10 m class telescopes (e.g. Falomo, Kotilainen & Treves 2001) using their large photon-collection area and high resolution.

While the mere detection of QSO hosts often requires no more than elementary and intuitive methods such as azimuthal averaging and PSF subtraction, such procedures have repeatedly been suspected of producing quantitatively biased results (e.g., Abraham, Crawford & McHardy 1992; Ravindranath et al. 2001). Quite certainly, they take insufficient advantage of the full spatial image information content. In recent years, some groups have started to develop two-dimensional model fitting codes addressing these issues, with the goal to simultaneously decompose deep QSO images into nuclear and host components in a more objective and unbiased way (e.g., McLure, Dunlop & Kukula 2000; Wadadekar, Robbason & Kembhavi 1999; Schade, Lilly, Le Fevre, Hammer & Crampton 1996). Ideally, such a method should provide the flexibility to be used with a wide range of ground- and space-based datasets, account for non-ideal detector properties, and require no more than standard computing resources.

In this chapter we describe our own approach to tackle this task. We first outline some key features of the algorithm, and then discuss the performance of our method as applied to simulated imaging data.

In Chapters 3 and 4 we will present two samples of low- and intermediate-redshift QSOs to underline the method's usefulness. The method is currently used extensively on various large datasets of QSOs, achieving high data throughput for the modelling which is one of the aims for our code. We will report in detail on these projects briefly in Chapter 5.

2.2 Overview

Optical and near-infrared images of quasars are always compounds of a more or less extended host galaxy (which morphologically may be as simple or as complicated as any 'normal' galaxy), plus an embedded point source. Analytic models of such configurations invariably require several approximations and simplifications, which in our approach can be summarised as follows:

- The overall surface brightness distribution of the host galaxy can be described by smooth and azimuthally symmetric profiles, modified to allow for a certain degree of ellipticity.

- Host galaxy components and active nucleus (in the following: ‘nucleus’ or ‘AGN’) are concentric.
- The solid angle subtended by a given quasar+host is significantly smaller than the field of view.
- The point-spread function (PSF) is either shift-invariant over the field of view, or else its spatial change can be described by low-order multivariate polynomials.

These assumptions are adequate for the type of distant AGN that we are chiefly interested in, but some will break down for very nearby galaxies with highly resolved structural features; such objects are not our primary targets, and we do not consider their specialities in the following.

The model-fitting process can be split up into several distinct tasks, to be executed subsequently:

1. Construction of a variance frame quantifying individual pixel weights, usually by applying Poisson statistics and standard error propagation to object and background counts. This step includes the creation of an optional mask to exclude foreground stars, companion galaxies, cosmics, etc.
2. Identification of stars in the field to be used as PSF references. As the PSF description is fully analytic, even stars fainter than the quasar can yield useful constraints.
3. Determination of an analytic PSF model for the entire field of view, accounting for spatial variability. An optional empirical lookup table can complement this if required.
4. Establishing initial guess parameters for the AGN+host galaxy model.
5. Computation of the actual multiparameter fit by minimising χ^2 iteratively, including multiple restarts to avoid trapping in local minima.
6. Estimation of statistical uncertainties by running the model-fitting code on dedicated simulations mimicking the actual data.

We give details on each of these steps in the following sections.

The software was developed under the ESO-MIDAS[1] environment with all computing intense tasks coded in C. The code itself is still being optimised and adapted to various telescopes and configurations (including HST), we hence do not plan to publish it for the time being.

2.3 PSF Modelling

2.3.1 Strategy

Knowledge of the point-spread function (PSF) is important in two aspects of the decomposition. First, it is obviously needed to describe the light distribution of the unresolved AGN itself. Any mismatch here could lead to a misattribution of AGN light to the host galaxy or vice versa. Second, for the typical objects of interest the apparent host galaxy structure will strongly depend

[1] http://www.eso.org/projects/esomidas/

on the degree of PSF blurring. This process needs somehow to be inverted in order to determine the corresponding structural parameters. In extreme cases, e.g. when even a marginal detection of a faint high-redshift host would be considered a success, accurate PSF control becomes the most important part of the entire analysis.

As long as the image formation process can be approximated by a shift-invariant linear system, the straightforward and most frequently adopted way of obtaining the PSF is to use the image of a bright star in the field of view. However, even within this approximation using a single star has some non-negligible drawbacks, mainly associated with the problem of rebinning: Unless the PSF is strongly oversampled, shifting an observed stellar image to a different position invariably leads to image degradation and consequently to AGN/PSF mismatch. Ironically, at a given spatial sampling this effect is largest for a very narrow PSF, thus for the best seeing. Furthermore, a single PSF star of sufficient brightness to constrain also the low surface brightness wings of the PSF is not always available, an effect which can render entire images effectively useless. Finally, in a few cases even the only available PSF star could be contaminated by a companion star or galaxy, which would introduce severe artefacts into the analysis.

A simple averaging of stellar images to increase the S/N is often prevented by the fact that several large-field imagers, even modern ones, show spatial variations in the imaging properties; in the above terminology, the system may still be linear but not shift-invariant any more. Within the simple approach of resampling PSF reference stars to the AGN position, there is only one possible solution to this problem, namely limiting the allowable distance AGN–PSF star to a minimum, and thereby often discarding the brightest stars in the field.

To overcome this we adopted the alternative to describe the PSF by an analytical expression, producing an essentially noise-free PSF at any desired location with respect to the pixel grid. An obvious advantage of this approach is the fact that once a good analytical description for a single star is found, averaging over several stars is straightforward. In fact, since the main PSF parameters can be measured confidently even at moderate S/N ratio, the number of potential

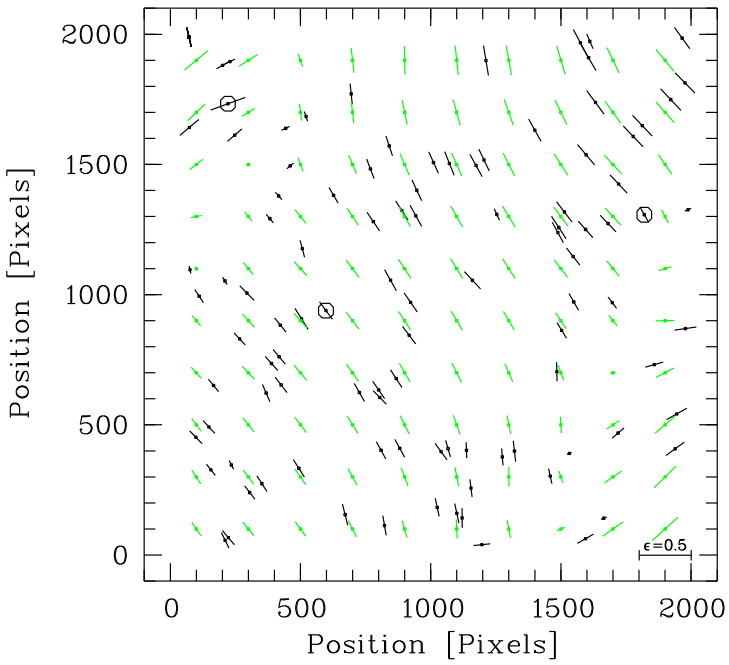

Figure 2.1. Visualisation of a spatially variable PSF. Each vector corresponds to one star found in the image, its length given by the ellipticity and its orientation by the position angle of the major axis. Note the well-ordered pattern which makes analytic modelling straightforward, the resulting model grid is overlaid in light gray. Circles mark the stars of Figure 2.2 in same order from left to right. Image size is 13.′3 across.

PSF stars usable is greatly increased, as now even stars considerably fainter than the AGN can be used to provide constraints.

In a straightforward generalisation of the analytic approach, the PSF parameters can be described as spatially variable across the field. As long as the variation model is adequate, all stars in the field can still be used to trace and constrain the PSF. This is demonstrated in Figures 2.1 and 2.2, taken from our 1998 ESO data documented below, but we have found similar effects with several other instruments: While the ellipticities and orientations of point sources in the field are obviously not constant, there is a discernible variation pattern. Once this pattern has been taken into account, the overall PSF shape can be described by a well-constrained set of parameters.

By choosing this approach, we consciously optimise our algorithm to images with relatively simple PSF shapes, i.e. mainly ground-based data without adaptive optics. For instruments with a more complicated PSF such as HST, a purely analytic point-symmetric PSF is clearly a gross oversimplification. However, departures from the symmetries assumed in the analytic model can be accounted for up to a certain degree by applying a numerical lookup table correction (see Section 2.3.3 below).

Table 2.1. Quality of different PSF models with or without correction of spatial variability, one- and two dimensional LUTs. For the stars shown in Figure 2.2 we tabulate the rms of residuals in per mill of total stellar flux and the reduced χ^2.

Correction			PSF 1		PSF 2		PSF 3	
var.	1d.	2d.	ΔF	$\chi^2_{\rm red}$	ΔF	$\chi^2_{\rm red}$	ΔF	$\chi^2_{\rm red}$
+	+	+	0.66	2.2	0.59	1.6	0.29	1.7
+	+	–	0.95	2.6	0.60	1.7	0.34	1.8
+	–	–	1.01	2.9	0.77	1.8	0.39	2.3
–	–	–	1.66	6.3	0.96	2.2	0.60	3.7

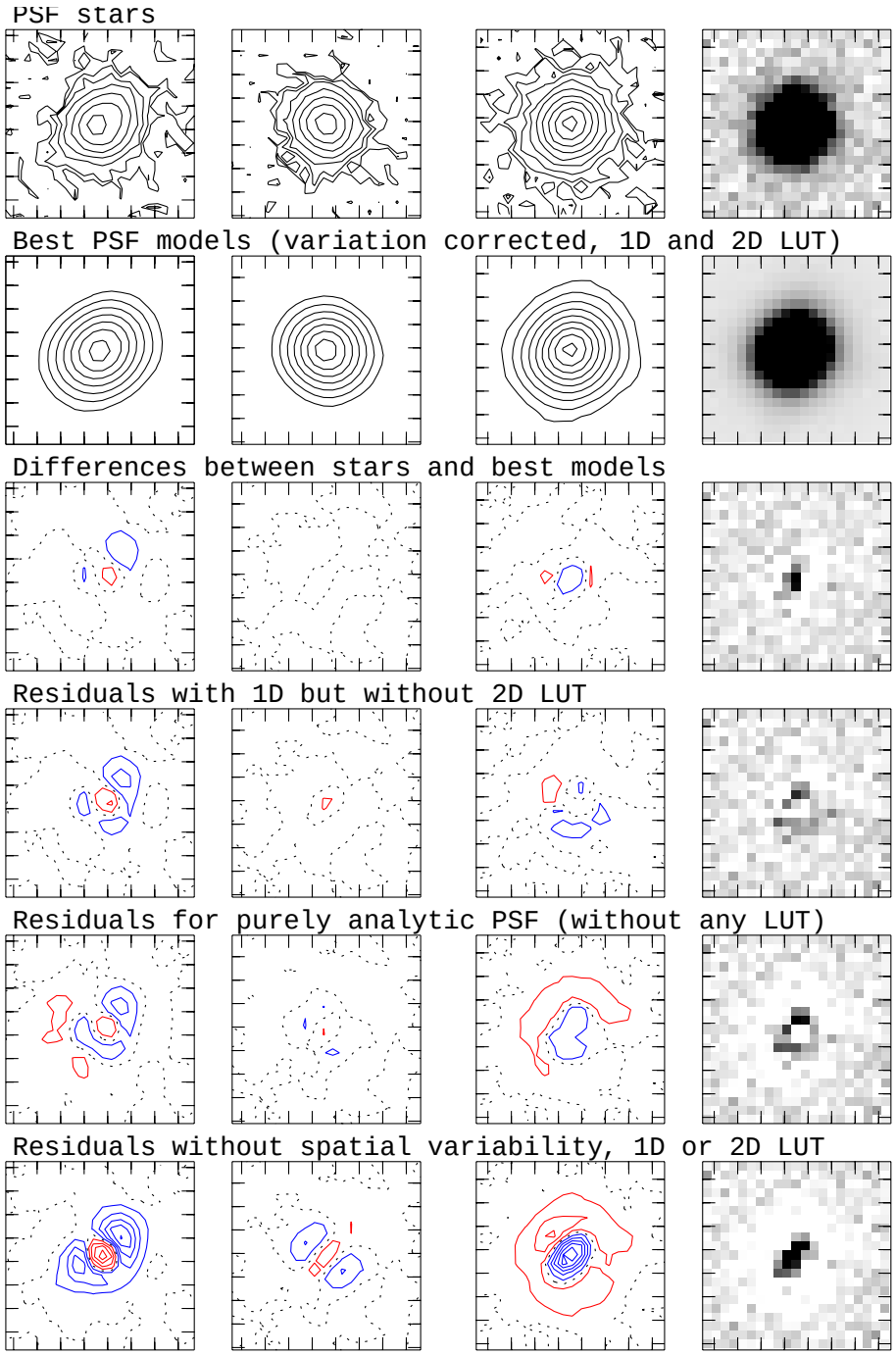

Figure 2.2. Modelling the PSF variations. Top row: Logarithmic contour plots of three example stars taken from different locations in the same image. Slightly varying ellipticities can be traced even by eye. Second row: best models with modelling of spatial variation, one- and two-dimensional lookup table corrections. Third and subsequent rows: Residuals after subtracting decreasingly elaborate PSF models from each star. Contours are linear and symmetric around zero (dotted line). Coordinate tickmarks in all plots are $0\farcs5$ apart. The rightmost column contains grayscale plots of star 3, the best model and the corresponding residuals at constant image cuts.

2.3.2 Analytic models

To describe the radial PSF shape we have adopted Moffat's (1969) PSF parameterisation, given in a modified form in Equation 2.1 below. We find that this profile provides a reasonable fit to the PSF for several different datasets obtained in both optical and NIR domains. Note that the Moffat parameter β, which basically controls the kurtosis of the profile (larger β implying a more peaked profile with weaker wings) has to be included as a free parameter, as we often find best-fit β values significantly different from the canonical value of 2.5. Moffat's original description has been reformulated to use $r_{1/2}$ as the radius which encloses half the total flux:

$$F_{\rm PSF}(r) \quad = \quad F_{0,\rm PSF}\left[1+\frac{r^2}{r_{1/2}^2}\left(2^{1/\beta}-1\right)\right]^{-\beta} \tag{2.1}$$

Other analytic forms are conceivable, though the number of free parameters should not be increased, as this requires to increase the lower flux limit of acceptable stars which in consequence will decrease the number of sampling points of the spatial PSF variation. Instead, deviances between the analytic shape and the moffat can be handled by a lookup table, described in the next section.

The azimuthal PSF shape is assumed to be elliptical, thus requiring a semimajor axis a, a semiminor axis b, and a position angle ϕ as additional parameters to specify the model. We do not use these parameters directly, but transform them into

$$\begin{aligned} a_x^2 &= \frac{a^2(1-\varepsilon)^2}{1-\varepsilon(2-\varepsilon)\cos^2\phi} \\ a_y^2 &= \frac{a^2(1-\varepsilon)^2}{1-\varepsilon(2-\varepsilon)\cos^2(\phi+\pi/2)} \\ a_{xy} &= \frac{2-\varepsilon(2-\varepsilon)\,(1+\sin 2\phi)}{b^2} - \frac{a_x^2+a_y^2}{a_x^2 a_y^2} \end{aligned} \tag{2.2}$$

where $\varepsilon = 1-b/a$. With these provisions and assuming for simplicity the centroid to be at $(0,0)$, the PSF shape in each pixel (x,y) is given by

$$F_{\rm PSF} = F_{0,\rm PSF}\left[1+\left(\frac{x^2}{a_x^2}+\frac{y^2}{a_y^2}+a_{xy}xy\right)(2^{1/\beta}-1)\right]^{-\beta}. \tag{2.3}$$

A similar expression for the PSF was already employed successfully in crowded field photometry packages such as DAOPHOT (Stetson 1987), and we simply adopted that concept to our needs. Its chief benefit lies in the fact that variations in position angle over the field, even a complete flip of orientation, correspond to secular changes in the a_x, a_y, a_{xy} parameters. This fact enables us to use simple bivariate polynomials to describe the variation of parameters over the field of view, i.e. expressions of the form

$$\begin{aligned} a_x(x,y) &= c_0 + c_1 x + c_2 y + c_3 xy + c_4 x^2 + c_5 y^2 + \ldots \\ a_y(x,y) &= d_0 + d_1 x + d_2 y + \ldots \\ a_{xy}(x,y) &= \ldots \end{aligned} \tag{2.4}$$

The actual process to establish a complete PSF model runs as follows: First the suitable stars are selected. The brightest stars are modelled individually with a full five-parameter PSF model (Equation 2.3), with the aim to find a best β for the dataset. Once this is done, β is fixed for all subsequent PSF fits, i.e. we do not allow β to vary spatially.

In a next step we fit four-parameter models to *all* stars, using the modified downhill simplex described in detail in the next section. This results in a table of PSF parameters at various positions (x_i, y_i) in the image frame. If the parameters are consistent with being constant over the frame, or if the scatter is much larger than any possible trend, the simple average is taken, otherwise a least-square bivariate polynomial is computed. We have currently implemented polynomial orders between 1 (bilinear) and 3 (bicubic). The degree which fits best is taken for the final PSF model, with the additional condition that the *gradient* of the polynomial should be small in the vicinity of the AGN. Extremely ill-fitting stars (and undetected binaries, galaxies etc.) are iteratively removed from the table and do not contribute to the variation fit.

In the example of Figure 2.1 we plotted position angle and ellipticity of all usable stars along with a grid of reconstructed values. The number of stars in the example is high, but not exceedingly so. The stability of the process allows us to use stars significantly fainter than the quasar of which we find many thanks to increasing telescope power and detector sizes. In our applications like those presented in Section 7.2 we typically find 20 – 30 or so usable stars per image.

2.3.3 Lookup table correction

For cases where the quality of the PSF determination is critical, i.e. for data with bad seeing or compact hosts, the analytic representation of the PSF may be an over-simplification. Without giving away the advantages of the analytic description, we can apply two second-order corrections in the form of empiric lookup tables (LUTs):

$$F_{\mathrm{PSF,corr.}} = F_{\mathrm{PSF}} + N\,[L_1(r_n) + L_2(x,y)] \tag{2.5}$$

with $r_n = r/r_{1/2}$ being the normalised radius, r the elliptical radius as described in Equation 2.8 and N a scaling factor for the LUTs. Here we distinguish between the case of azimuthally symmetric errors and that of errors with more complicated or no symmetries:

The one-dimensional (radial) LUT L_1 contains those corrections that show the same symmetry and variation as the model PSF itself. It describes the intrinsic radial shape difference between the simple analytical model and the more complicated PSF and can be expressed as an additive term in Equation 2.1.

In practice, $L_1(r_n)$ is obtained by assessing the residuals of PSF stars, normalised to unit integral flux, after subtraction of the best fitting analytic model. Of those we compute radial profiles spaced in equidistant fractions of $r_{1/2}$.

For each radial bin we then average the individual residual profile value for all stars. Due to the previous normalisation and azimuthal averaging, this process is now independent of the spatial PSF variation. The resulting lookup table $L_1(r_n)$ can then be used to correct the symmetric radial errors according to Equation 2.5. In Figure 2.3 we have done this for the image presented in Figure 2.1. The purely analytic model can describe the profile only up to a certain degree. To improve the fit (most conspicuously needed between two and four arcseconds) we add the radial LUT, scaled by the total stellar flux, in a range where it can be determined with high S/N.

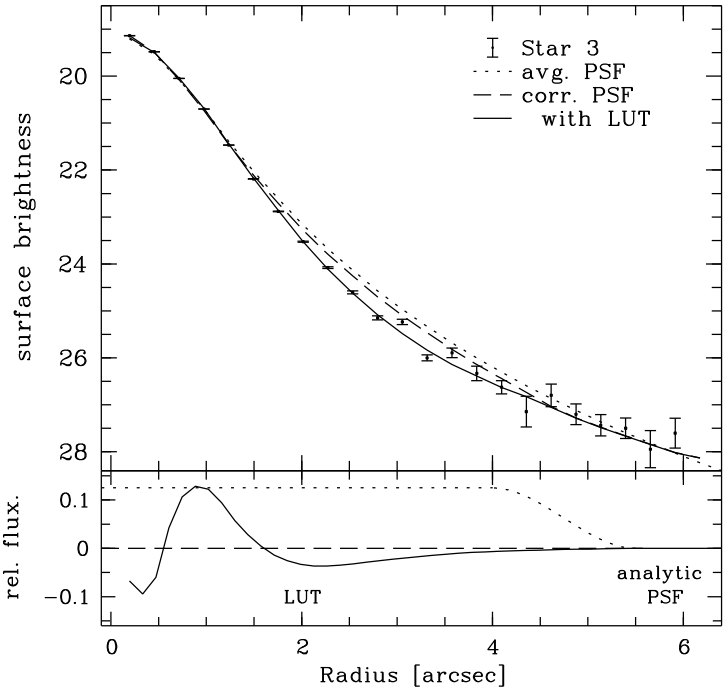

Figure 2.3. Comparison of profiles with and without radial LUT. As example we take star 3 from Figure 2.2. Top panel shows profiles of the star (dots), the best-fitting model with LUT (full line) and without LUT (dashed). Bottom panel shows the radial lookup table (solid line) in per cent of the total flux, together with a scaled transition function $f(r)$ (dotted line) defining the outer LUT boundary.

Note that the scale of the LUT is linear while the profiles are plotted logarithmically, the LUT is hence mostly needed in the centre, not in the wings.

In the next step we apply this global correction to all stellar models, adapted to their individual model geometry, and again record the residual images. Averaging these residuals after flux normalisation yields a two-dimensional array $L_2(x,y)$ which is just the desired lookup table. To avoid sampling errors, the images should be resampled to have the same subpixel centroids.

The quality of both corrections is necessarily a function of the number of stars available, and of their S/N ratios. In any case, for both the one- and two-dimensional LUT there exists a radius beyond which Poisson noise will dominate. The LUTs should be truncated at this radius to avoid the introduction of additional noise. To avoid artefacts at the cut-off radius, we apply a smooth transition. For this we define a transitional annulus $[r_1{:}r_2]$ where $\tilde{L} = f(r)L(r)$ with $f(r)$ a third order polynomial for which holds:

$$\begin{aligned} f(r_1) &= 1 \\ f(r_2) &= 0 \\ f'(r_1) &= f'(r_2) = 0\,. \end{aligned}$$

The transition radii are determined interactively as the range where noise starts to dominate the LUT. An example of the transition function $f(r)$ is shown in Figure 2.3. Up to a radius of $4''$ we have $f(r) = 1$, while within the transition annulus $f(r)$ decreases to 0. The effective $\tilde{L}$ is also plotted.

In Figure 2.2 we show the improvement in PSF fitting with each successive increase in model complexity. In the top three rows we plot logarithmic contours of three stars and the best-fitting models as well as linear contours of the resulting residuals. In the following rows we successively reduce the model complexity which leads to an increase in the residual structure as well as in the rms of the residual as shown in Table 2.1. Taken all corrections together we now have a high S/N-model of the PSF.

2.3.4 Uncertainties

The PSF of an instrument can be very complicated (e.g. in the case of HST). Perfect modelling of the PSF is beyond our scope. Still we have to consider how large the uncertainties in the PSF fitting will be and what will be the impact on the final results.

In our process, we have two different processes witch introduce errors in the PSF determination. First, the fit of a single star will always leave a residual, as can be clearly seen in Figure 2.2. This can be corrected to a certain degree by a LUT, in the case we have sufficient stars in the field. Second, the fitting of the PSF variation can yield incorrect values. This will lead to inaccurate and possibly biased fits. How large the influence will be depends on the quality of the observations and the properties of the observed objects. It can therefore only by estimated in dedicated simulations, like the one done in Section 2.5.2.

In order to estimate the accuracy of the above process, we adopted the 'leaving one out' method from Duda & Hart (1973). We repeat the PSF determination but leave one star out. From the remaining stars we get a prediction of the PSF parameters at the star's position which is independent from the star itself. We do this for all the stars and average the differences between predicted and measured PSF parameters. If the stars cover the field evenly this will be a good estimate for the uncertainty of the QSO PSF.

In order tto detect numerical or computational problems easily, the fitting process is monitored and documentented in diagnostic plots. Figure 2.4 is an example for such a plot. In the bottom-left panel we plot the major axes of the stars used for the spatial variation model with the axes scaled at the respective eccentricities and plotted and measured position angles in order the emphasize the variation of ε and α with position on the detector. A comparison between models predicted from the variation model and models fit individually to the stars can be made in Panel b). For both we plot isophotes at forty times the HWHM radius, predicted in solid black, measured with dashed lines. Any systematic differences should be visible here, but in hardly any case dashed and solid lines do not coincide. In four cases stars were excluded because they showed peculiarities, for those we have no solid lines. A different check is to use Panel f), where we plot histograms of $\chi^2_{\rm red}$ values of individual (dashed) and predicted models. Optimally, the solid (predicted) distributions would be identical the the dashed, as the predicted models cannot be better than the individual. To visualize the quality of the fit we plot contours and profiles for a singe star (marked with a cross in Panels a) and b)). In Panel g) we also plot the radial LUT. The two-dimensional LUT normally plotted in Panel h) is not needed here, as we can see no large non-point-symmetric residuals in Panel d). The numeric values for the PSF at the quasar location are listed in e) with errors computed with the 'leaving one out' method. β is bracketed, because is was a constant.

2.4 Image decomposition

2.4.1 Models

In order to describe the surface brightness distribution of QSO host galaxies we have restricted ourselves to the two most commonly used analytical prescriptions – an exponential Freeman (1970) law describing early type disc galaxies, and a de Vaucouleurs (1948) '$r^{1/4}$' law describing

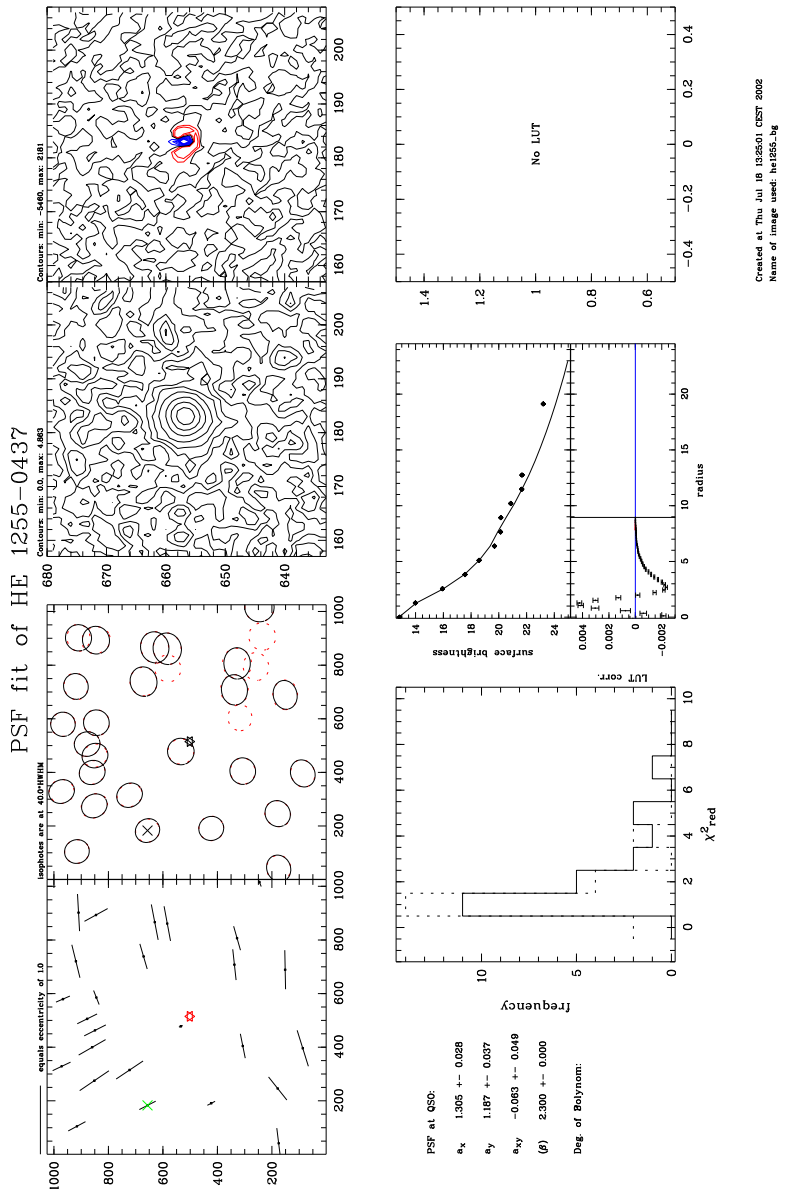

Figure 2.4. Diagnostic plot of the PSF determination. We plot on the left column (bottom to top): a) Eccentricity and position angle of the stars, cross marks the sample star, the star symbol the position of the quasar. b) Isophotes of the stars (solid) and the predicted models (dashed). c) Contourplot of the sample star. d) Contourplot of the residual. Right column: e) Numeric values of the QSO PSF. f) Histograms of χ^2 values of individual (dashed) and predicted models. g) Profiles of the sample star, its model and the 1D LUT. h) grayscale of the 2D LUT.

spheroidals, applicable to elliptical galaxies and disc galaxy bulges:

$$F_{\rm disc}(r) = F_{\rm disc,0} \exp\left(-1.68\,\frac{r}{r_{1/2}}\right) \tag{2.6}$$

$$F_{\rm sph}(r) = F_{\rm sph,0} \exp\left[-7.67\left(\frac{r}{r_{1/2}}\right)^{1/4}\right] \tag{2.7}$$

where the 'radius' r is a function of x and y:

$$r^2 = \frac{1-\varepsilon(2-\varepsilon)\cos^2(\alpha-\phi)}{(1-\varepsilon)2}\left(x^2+y^2\right)\,, \tag{2.8}$$

with $\tan\alpha = y/x$. (Exponential bulges in late-type spirals are currently not modelled as these are not known to harbour significant nuclear activity). Thus, each galaxy model contains four independent parameters: The semimajor axis a for which holds that $r(a) = r_{1/2}$; the ellipticity $\varepsilon = 1-b/a$; the position angle of the major axis, ϕ; and the total flux $F = \int F(r)\,{\rm d}r$. Notice that we avoid to use the ill-constrained central surface brightness as a fit parameter. It is well known that the determination of effective radius and central surface brightness is strongly degenerate in the presence of measurement errors (e.g. Abraham et al. 1992), and that the total flux F_0 is much better constrained than either of these parameters. This issue will be addressed again in Section 2.5 below, in particular in Figs 2.7 and 2.9.

To summarise, a typical model will contain either five or nine parameters: four for each galaxy component, plus a point source scaling factor for the AGN. However, we have also implemented an option to keep individual parameters at a fixed value, so that the above numbers give the *maximum* number of parameters.

2.4.2 Convolution

Although both PSF and galaxy are represented by analytic functions, the nonzero ellipticities demand that the convolution be evaluated numerically. In numerical convolution, sampling plays an important role: strictly speaking, we have to distinguish between (a) the function value at given x,y; (b) the PSF-convolved value; (c) the image value sampled into a rectangular pixel grid. These values will be similar only in areas of small gradients in the surface brightness distribution; close to the centre, the galaxy light has to be sampled on a much finer grid in order to avoid large numerical errors. On the other hand, a highly oversampled pixel grid leads to a substantial increase in computing time and is therefore inefficient. It is also not required in the outer regions.

Our adopted solution uses the local gradient in the unconvolved image to adjust the degree of oversampling, as illustrated in Fig 4. This adaptive subpixel grid is determined at the beginning of each fitting subprocess (see below). Whenever the model parameters change substantially, the grid is recomputed and the fitting process is resumed with this new grid.

2.4.3 The fitting process

The model parameters are iteratively adjusted by minimizing χ^2 with the downhill simplex method (Press et al. 1995). Here, the χ^2 values are based on variance frames associated with

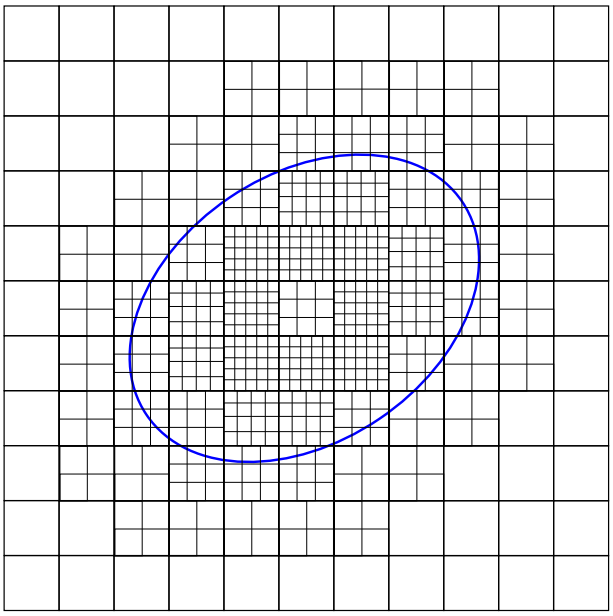

Figure 2.5. Illustration of the adaptive subxpixelling. Each pixel with a gradient larger then a threshold value is divided into subpixels. These subpixels itself are divided as long the gradient is still too large. The size of the original pixels is maintained in the outer parts. The ellipse represents this object's half-light isophote.

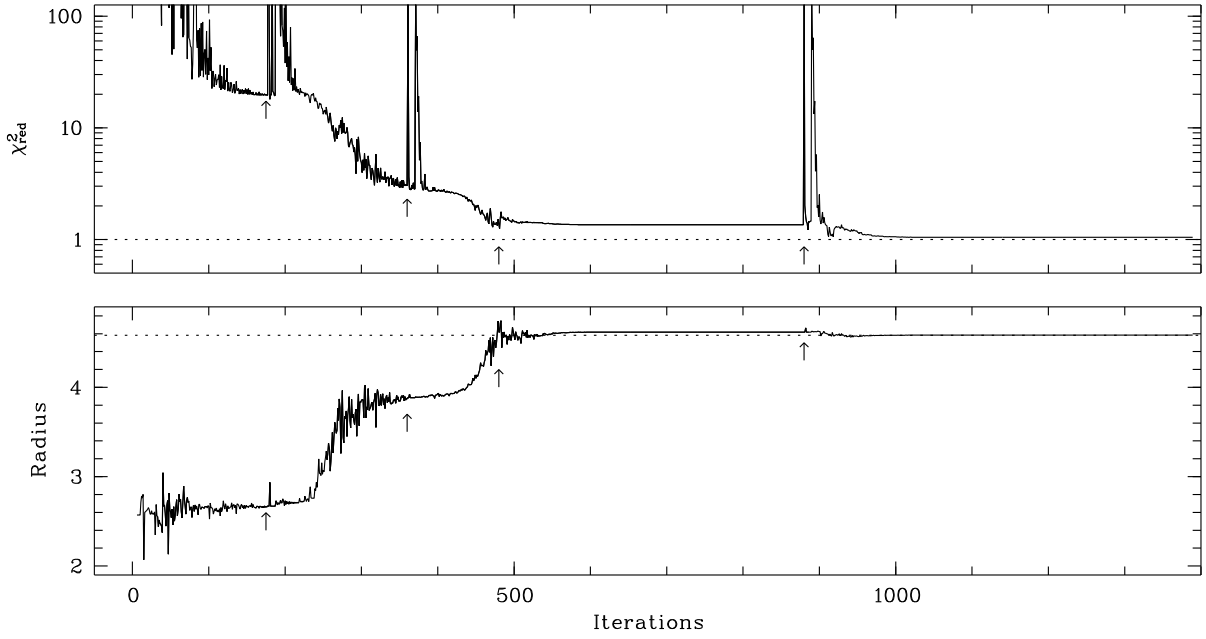

Figure 2.6. Illustration of the fitting process, using one of our simulations. Shown are the variations of half-light radius (bottom) and reduced χ^2 (top) as the iteration proceeds. Arrows indicate points where the iteration was restarted. The true (input) value of the half-light radius is marked with the horizontal dotted line.

each image, which may also contain information about regions that are to be left out of the fitting process.

In order to accelerate and stabilise the minimization, the parameter space is transformed to achieve 'rounder' χ^2 valleys. Long, narrow valleys which occur when the typical range of two parameters are several orders of magnitudes apart (e.g. the flux and the ellipticity) are a major obstacle for the simplex method. We use the following transformation recipes: ε is

substituted by $\varepsilon' \equiv \log(1-\sqrt{1-\varepsilon^2})$, and F is substituted by $F' \equiv \log(F+O)$. As a byproduct, this transformation automatically ensures that F has a lower acceptable bound $-O$. Note that $O = 0$ (i.e. demanding $F > 0$) is not always a good choice; in the case of a faint or undetectable host galaxy and in the presence of noise, slightly negative values of F must be permitted.

Additional boundary conditions can be imposed by artificially setting χ^2 to a very large value for all parameter values outside a set range. In this way we just change the shape of the χ^2 function to be minimized, and we do not have to intervene in the minimization process itself. We use the following conditions: $r_{\rm min} < r < r_{\rm max}$, with typically $r_{\rm min} \simeq 0$ and $r_{\rm max} \simeq 100\,{\rm kpc}$; and $\varepsilon' \leq 0$ in order to have a well-defined major axis.

A crucial part of the algorithm is its subdivision into successive minimization substeps in order to avoid trapping in local minima. Whenever a χ^2 minimum is found, the process is restarted at the same location in parameter space, probing the environment for a further decrease in χ^2-values. Additional restarts are launched when the change in parameters requires a reevaluation of the subpixelling grid. Only when even repeated restarts yield no improvement in χ^2, the entire process is considered to have found a global minimum. This way we can usually avoid to be trapped in shallow local minima or regions of small curvature. An example for a sequence of substeps is given in Figure 2.6, based on simulated data: The top panel shows the variation of $\chi^2_{\rm red}$ (χ^2 per degree of freedom) as a function of the sequence of iterations, while the lower panel monitors the corresponding value of the half light radius. Restarts occured when χ^2 showed little change, or when the radius changed substantially. Since with each restart the computational accuracy is increased, a rapid localisation of the rough region of the minimum is followed by a much slower zooming in on the actual minimum.

Fitting the full set of nine parameters is only useful for data with excellent spatial resolution, providing significant independent constraints for all three components. There are various ways to reduce the number of fitting parameters; besides fitting just one galaxy model, we have included an option to keep parameters at a fixed value. This is useful e.g. in the analysis of multicolour data where certain structural parameters might be well-constrained in one dataset (e.g., HST) which then can be used to increase the modelling fidelity of images taken in other bands.

2.5 Simulations

To test the reliability of the AGN decomposition process, we constructed extensive sets of simulated galaxies. As the multitude of instruments and objects prevents a test for the full range of possible data, we limit the test to two rather different sets which both closely resemble certain observational data recently obtained by us. On the one hand, we consider a set of low redshift AGN observed with a 1.5 m telescope; these simulations resemble the 'test sample' described in Section 3.1 of this thesis. On the other hand, we consider the case of medium to moderately high redshift QSOs (up to $z \simeq 1$), observed with a 4 m class telescope. These two simulated datasets will henceforth be referred to as 'low z' and 'med z'. Input properties are listed in Table 2.2.

We have thus constructed a test bed for two very different configurations. The low-redshift objects were created using various combinations of three components (disc, spheroid and a nuclear source), and among these objects we expect to find and retrieve all Hubble types. For the medium and high redshift data we expect elliptical galaxies to dominate the host galaxy population. In this case the objects are compounds of only a spheroidal and a nuclear component,

Table 2.2. Overview over our simulations. The input parameters are total counts F (in units of detector photoelectrons) and half-light radii r. Corresponding absolute magnitudes M and linear radii r [kpc] are also listed for comparison. For details see text and Table 2.3.

Dataset	$F_{\rm nuc}$ 10^5 [e$^-$]	$F_{\rm disc}$ 10^5 [e$^-$]	$F_{\rm sph}$ 10^5 [e$^-$]	$r_{\rm disc}$ [arcsec]	$r_{\rm sph}$ [arcsec]	$-M_{R,\rm nuc}$	$-M_{R,\rm disc}$	$-M_{R,\rm sph}$	$r_{\rm disc}$ [kpc]	$r_{\rm sph}$ [kpc]
med $z\|_s$	10	–	2.5	–	1.3	24.5	–	23.0	–	10.0
med $z\|_z$	11–7.8	–	11–0.8	–	1.2–4.1	24.5	–	22.0–24.5	–	8.7
med $z\|_e$	10	–	2.5	–	1.3–10.8	24.5	–	23.0	–	10.0–78.4
low $z\|_M$	10	1.0–20	1.0–20	6.0	3.0	24.2	21.7–25.0	20–22.5	5.0	2.5
low $z\|_R$	10	1.0	1.0	3.0–8.0	1.5–6.0	24.2	21.7	21.7	2.5–6.8	1.3–5.0

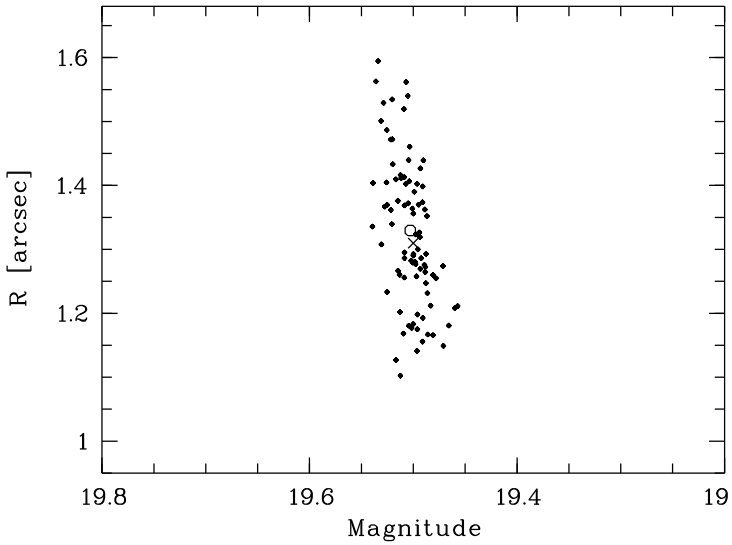

Figure 2.7. Results for the 'med $z|_s$' simulation, featuring different noise realisations and subpixel locations. Each dot represents the result of fitting one particular image. The circle indicates the average of the fitted values, and the cross denotes the 'true' input value. The nucleus is brighter than the host galaxy by 1.5 mag. The scatter of extracted parameter values (1σ) is 0.02 for the magnitude and 9 per cent for the radius.

and we attempt no more than reclaiming the properties of these two components, concentrating on luminosities and scale lengths. Here we do not investigate the influence of inclination on the decomposition process.

Both simulated sets were created using the same radial profiles and isophotal shapes that we used to compute the model galaxies during the fitting process. To account for observational errors we added artificial shot noise. The sets were then treated in the same way as real observational data. In order to avoid confusion between errors in the modelling of the spatial PSF variations and the fitting of galaxy and AGN, we assumed the PSF to be shift-invariant.

2.5.1 Medium-redshift simulations

We start with the medium-redshift simulations as these were fitted with the conceptually simpler two-component models. The first subset contains images of only a single galaxy, but 'observed' numerous times, i.e. with several different noise realisations, and with different centroid positions with respect to the pixel grid (dataset 'med $z|_s$', for 'single redshift', in Table 2.2). The input galaxy is a typical bright elliptical galaxy with half-light radius $r_{1/2} = 10$ kpc, an absolute luminosity of $M_R = -24.5$ at a redshift of $z = 0.6$, with a nucleus four times brighter than the host galaxy.

To compute realistic flux and background levels, we used the exposure time calculator for the ESO-NTT and its multi-mode instrument EMMI, assuming a pixel size of $0\farcs27$ and a total exposure time of 500 s per simulated image. In order to specify the background level, we assumed the data to be obtained in the V band. The adopted PSF has a width of $0\farcs8$ FWHM, compared to $r_{1/2} = 1\farcs33$ for the galaxy.

Fitting the simulated images of this dataset, we found that we are able to reclaim the original host galaxy magnitude with an uncertainty of only 0.02 (1σ). This is shown in more detail in Figure 2.7, which also illustrates the well-known fact that the half-light radius is less accurately recovered. However, with an uncertainty of 9 per cent in $r_{1/2}$ we are still able to give a solid estimate of the galaxy size, even at this redshift and with a host galaxy only slightly more extended than the PSF.

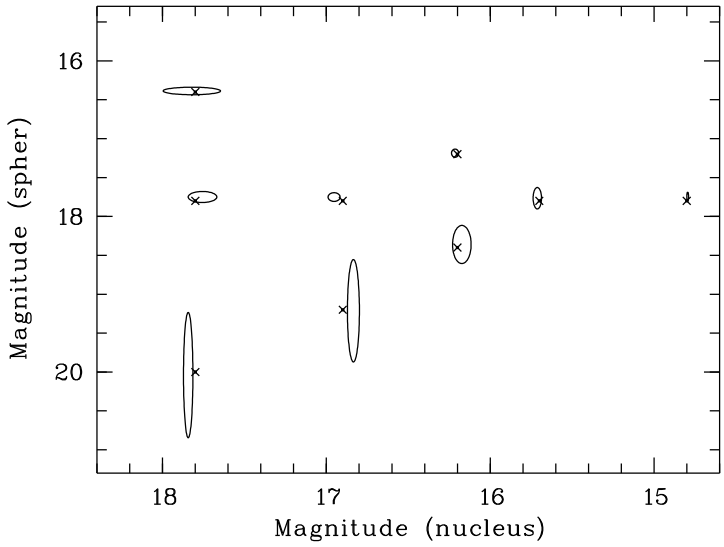

Figure 2.8. Results for the 'med $z|_m$' simulation, a set of models with different N/H ratios. Crosses represent the input values, and the ellipses approximately delineate the scatter of the extracted parameter values, with a minor semiaxis of 2σ in magnitude.

The second dataset ('med $z|_m$', for 'multiple magnitudes') was tailored to match a sample of $z < 0.35$ galaxies we acquired with the ESO-NTT in H band which we describe in detail in Chapter 4. The models were created to match the data in apparent diameter, counts and background noise with various the nuclear-to-host flux relations (N/H) and consist of a nuclear and a spheroidal component. As redshifts and exposure times vary, no underlying physical model can be defined, but by selecting measured values we assured that the models are both realistic and close to the data. Figure 2.8 shows that the accuracy of the decomposition depends on both N/H and total luminosity with the host galaxy luminosity generally much less confined. By choosing the spheroidal model we overestimate the errors for the less concentrated exponential components, errors shown are hence a cautious estimation.

In the second dataset ('med $z|_z$', for 'multiple redshifts'), we placed the galaxy featured in the $z|_s$ sample moved at four different redshifts ($z = 0.1$, 0.2, 0.4, 1.2) and changed the galaxy flux such that the ratio nucleus/galaxy takes three different values (10:1, 4:1, 1:1). To enable a fair comparison, the exposure time in each case was adjusted to yield the same S/N for all redshifts (cf. Table 2.3), and the underlying spectrum was assumed to be flat, i.e. we have the same luminosity in all the spectral bands. This latter assumption is obviously unphysical, but acceptable for our illustration purposes as the main free input parameters are the nuclear flux and the N/H.

For each configuration we generated images with several different noise realisations and fitted those independently. The results show clearly and not surprisingly that the accuracy of recovering the input parameters depends on redshift (see Figure 2.9). But even in the case of the most unfavourable redshift, $z = 1.2$ and the highest nuclear/host ratio, the reconstructed host galaxy luminosity has an rms scatter of less than 0.15 mag (1σ). Again, the half-light radii are less accurately determined

2.5.2 Influence of external parameters

In the simulations we assumed that we know the true value of the sky background and the PSF parameters. In reality all of these are afflicted with uncertainties. To test their influence we

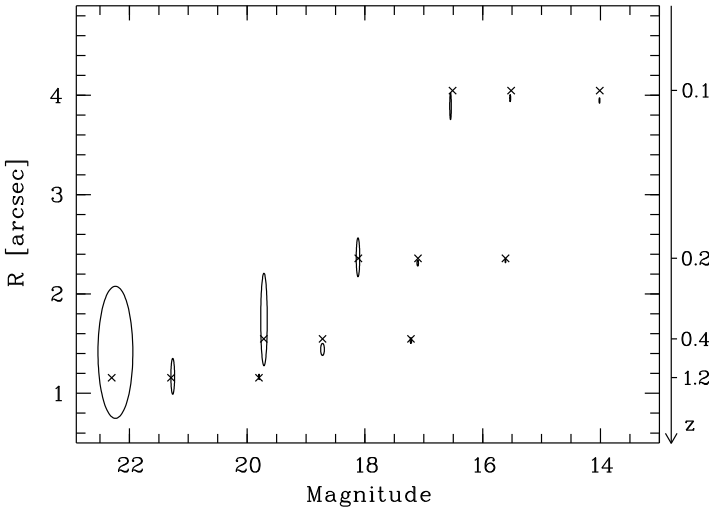

Figure 2.9. Results for the 'med $z|_z$' simulations, involving four different redshifts. Crosses represent the input values, and the ellipses approximately delineate the scatter of the extracted parameter values, with a minor semiaxis of 2σ in magnitude and a major semiaxis of 1σ in radius. The magnitude of the nuclear component is equal to that of the brightest host galaxy at each redshift. Values are given in arcseconds and *R*-band apparent magnitudes.

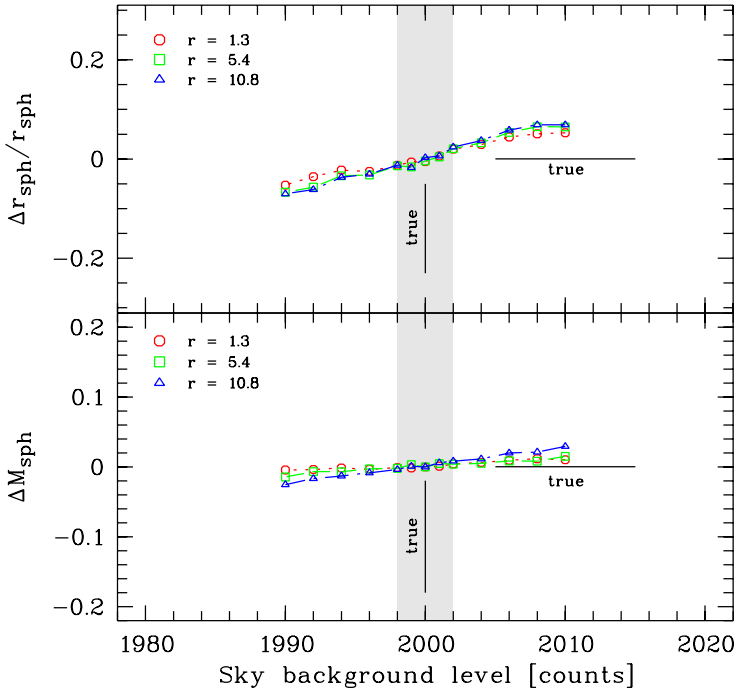

Figure 2.10. Dependence of recovered radii (top) and magnitudes of the galaxy (bottom) on the background determination. Instead of using the true value (marked with a vertical bar) we used offset values for the sky background to fit the data. The shaded area is the range of typical accuracy.

created a set of models ('med $z|_e$', for 'external) similar to the 'med $z|_s$' simulations but with three different galaxy radii ($r_{1/2} = 1\farcs33, 5\farcs4, 10\farcs8$). These models were fitted using deliberately wrong values (one at a time) for the sky background, which is notorious for influencing the results, and the PSF radius which appeared to be the most critical parameter.

In Figures 2.10 and 2.11 the results can be compared. While in the typical range of errors the uncertainties induced by an uncertain background are almost negligible for the magnitude and below 5 per cent for the radius, the accuracy of the determined PSF radius is essential. Errors are as large as 0.5 magnitudes or 50 per cent for the radius here.

Increasing the accuracy of the PSF parameters and knowledge of their uncertainties has been one goal of Section 2.3. With this and the simulations we get realistic estimates of the uncertainties of the final host galaxy parameters.

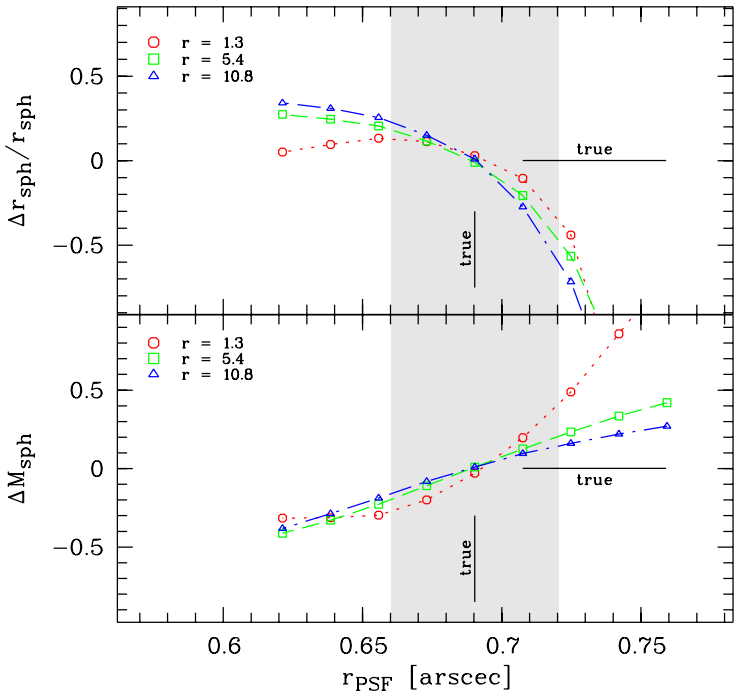

Figure 2.11. Dependence of recovered radii (top) and magnitudes of the galaxy (bottom) on accuracy of the radius of the PSF.

Set	z	V	t_{exp} [s]	BG [e$^-$/Pixel]
low z	0.02	14.0	840	800
med z	0.1	14.3	10	40
med $z\|_e$	0.1	14.3	10	40
med $z\|_m$	0.3	[1]) 16.5	10	13100
med z	0.2	15.9	44	176
med z	0.4	17.5	200	800
med z	0.6	18.4	500	2000
med z	1.2	20.1	3100	12400

Table 2.3. Redshifts, apparent nuclear magnitudes, exposure times and resulting sky background contribution adopted as input for the simulations. [1])H Band magnitude.

2.5.3 Low-redshift simulations

For well resolved AGN host galaxies a three-component fit may be more appropriate. In our low-redshift sample, the host galaxies are of all Hubble types and their morphology can be easily resolved even with small telescopes as we will show in the next section. To test the three component fitting, we generated a dataset to match those observations.

We simulated galaxies with both a disc and a spheroid and a bulge-to-total (b/t) flux ratio between 0.1 and 0.9. The ratio between nuclear and galactic light was varied between 5:1 and 1:4 (set 'low $z|_M$' for 'magnitude variation' in Table 2.2). The half-light radii were set to typical values found in our observed sample. All galaxies are azimuthally symmetric, no late-type features like bars or spiral arms were added.

Note that the simulations were designed to match the observations in integrated flux and apparent radii. Values in the table are given for a template observation of 840 s exposure time (on a 1.5 m telescope) and a redshift of 0.019, which was also used to compute the level of noise

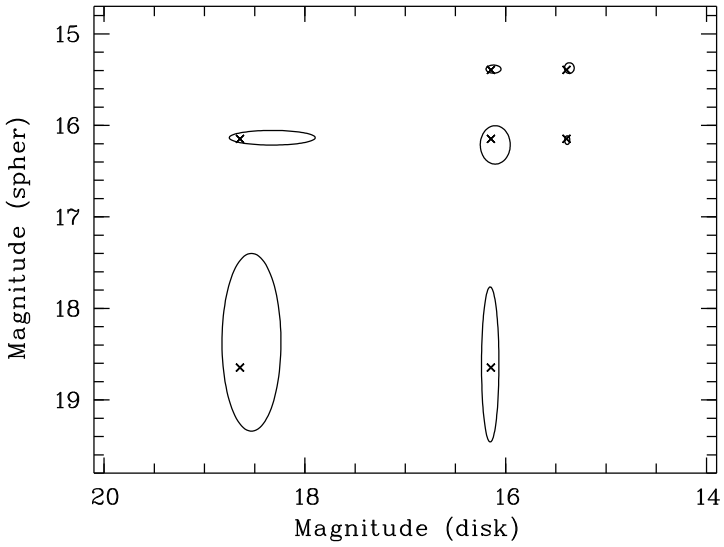

Figure 2.12. Results for the 'low $z|_M$' simulation, showing the accuracy of reclaiming component luminosities in three-component fits. The error ellipses have semiaxes of 2σ in magnitude. The nuclear component has a magnitude of 16.15 for all objects.

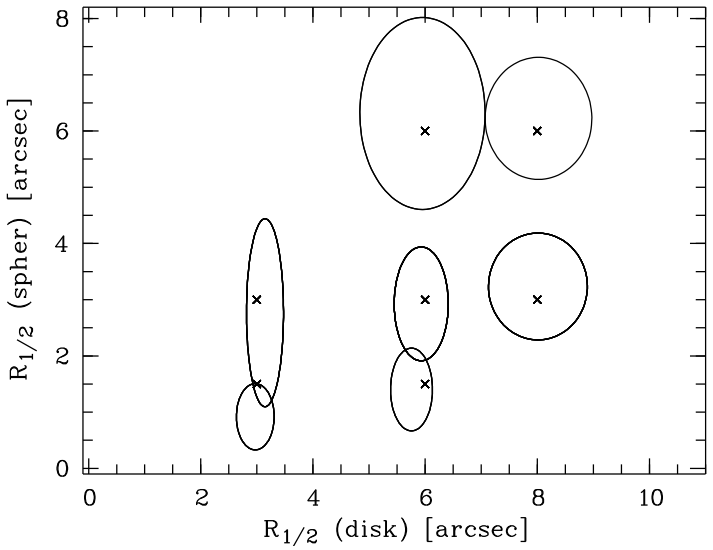

Figure 2.13. Results for the 'low $z|_R$' simulation, featuring three-component models with different half-light radii. Error ellipses have semiaxes of 2σ of the radius (in arcseconds). All objects have a nuclear to total galactic flux ratio of 5:1 and a b/t of 0.5. Radii are given in arcseconds.

of 800 e^-/Pixel at a pixel size of $0\farcs39$. We assumed a seeing of $1\farcs6$ (FWHM), which is rather poor but unfortunately was typical for our observations.

Figure 2.12 shows the results of the fits. The property dominating the uncertainty is the flux ratio between nuclear component and the galaxy (moving from lower left to upper right in Figure 2.12 decreases this ratio). The bulge magnitude is more affected by this than the disc magnitude, which is easily explained by the lower half-light radii of the bulge component, which is thus harder to be distinguished from the nucleus. The 1σ uncertainty grows from 0.03 mag for a ratio of 1:2 (nuclear to spheroidal flux) to 0.46 mag for a ratio of 10:1); the corresponding values for the disc component are 0.02 mag at 1:2 and 0.2 mag at 10:1.

In order to probe how well galaxy sizes can be recovered with these multicomponent fits, we varied the radii of both components between $1\farcs5$ and $6\farcs0$ (bulge) and $3\farcs0$ and $8\farcs0$ (disc) but left the fluxes unchanged, with the flux ratio set to the worst-case value of 10:1 for each component (dataset 'low $z|_R$', for 'radius variation'). Figure 2.13 shows that even when the nucleus dominates over the galaxy, the relative error in the determination of the half-light radius

is reasonably low (~ 5 per cent for the disc and ~ 20 per cent for the spheroidal component).

No special simulations were done for ellipticity and position angle. Within the above simulation, where both had constant values ($\varepsilon = 0.33$, $\alpha_{\rm sph} = 22$ degree, $\alpha_{\rm dis} = 37$ degree), they were on average fitted well with scatters below 2 per cent resp. 2 degree. Again for the faintest galaxies the scatter rose to 6 percent resp. 4 degree and 25 percent resp. 6 degree if the galaxy component was hidden by both a bright nucleus and a bright second galaxy component. We did not do specific simulations for other values of ε and α, but tests suggest, that for larger values both are determined even better, while for smaller values no large differences are expected, as the above case is already almost circular.

We conclude by stating that our simulations have yielded encouraging results. Total host galaxy luminosities can be reclaimed with high fidelity, and although half-light radii are less accurately constrained, there is no evidence for systematic errors. Recall that noise level, pixel sampling, and in particular seeing in these simulations were matched to our already existing data. It would be easy to design additional datasets obtained under better conditions, in which case a substantial improvement of measurement accuracy can be expected. We stress, however, the importance of individually tailored simulations in order to assess the potential and limitations of each observed dataset.

This and the following chapters are based on a submitted paper written by Björn Kuhlbrodt, Lutz Wisotzki and Knud Jahnke

3 Optical imaging of local Seyfert galaxies

3.1 Sample definition and observations

As a first test case with real data, we have investigated a small but statistically complete sample of low-redshift Seyfert galaxies. The objects form a subsample from the Hamburg/ESO survey (HES, Wisotzki et al. 2000) and constitute *all* identified Seyfert 1 galaxies with redshifts $0.01 < z < 0.05$ that are found within a well-defined survey area. Typical nuclear absolute magnitudes are around $M_B \simeq -21$, so these objects are representative for the vast majority of moderate-luminosity AGN found at low redshifts.

All 13 objects were observed in the *R* band using the ESO/Danish 1.54 m telescope on La Silla and its multi-purpose instrument DFOSC. The seeing during the three nights of observation was rather poor (1.″3–1.″8), but due to their low redshifts all of our objects were spatially well resolved.

The images were reduced with standard procedures (debiasing, flatfielding) and flux-calibrated using standard star sequences taken in the same nights. The resulting uncertainty of the apparent magnitudes is 0.04, mainly determined from the zeropoint errors. For computation of absolute magnitudes we used galactic extinctions from Schlegel, Finkbeiner & Davis (1998) and a cosmology of $h = 0.5$, $q_0 = 0.5$ and $\Omega_\Lambda = 0$.

3.2 Modelling

The fitting of the data followed the procedure laid out in Sections 2.3 and 2.4. The PSF determination for the observation was straightforward, as with the large field of view of the DFOSC detector ($13.'3 \times 13.'3$) always a large number of stars were available in the image, at least 20 or 30. Depending on the image, a second or third order polynomial could usually represent the variation to sufficient accuracy. Figures 2.1 and 2.2 were actually created from data presented in this section.

Some preparatory work before the host galaxy modelling involved fine-tuning of the local sky background near each AGN using growth curves, and masking all features in the frames that clearly do not belong to the object. The maximum fitting radius was set to an ellipse containing 99.5 per cent of the total object flux. The contour plots in Figure 3.5 have been made just large enough for this ellipse to fit in.

Good initial parameter estimation is very important to avoid local χ^2 minima located at parameter combinations very different from those near the global minimum. At least with the simplex method it is difficult to leave such a minimum, once trapped in it. We estimated initial parameters in the following way: We first determined the isophotal shape of the disc component (nearly always the most extended component) by fitting ellipses to the outermost isophotes. The scale length and total flux was then obtained from fitting an exponential law to the outermost part of the surface brightness profile. The determination of the bulge parameters was done likewise, but using the original image with a convolved disc component subtracted. Finally the remaining central flux was attributed to the nucleus. If any of these steps led to unsatisfactorily strong residuals, the process was repeated in a different order (first spheroid, then disc). The parameter values obtained from this procedure were used as initial guesses, enabling us to start the full

Table 3.1. The low-redshift Seyfert sample. Columns are: Name in the Hamburg-ESO Survey, alternative name, redshift, total apparent magnitude in *R*, seeing in arcseconds, absolute *R*-band magnitudes of nucleus, spheroid and disc (please note the change of signs), bulge-to-total flux ratio, half-light radii of the spheroid and the disc in kpc, Hubble type (E: E–S0, S: Sa–c, SB: barred, S*B* marginal detection of a bar) and signs of interaction (m = merger, t = tidal features).The second row of each object lists the nominal 2σ error derived from the simulations.

HES Name	alt. name	z	R_T	s	$-M_{\rm nuc}$	$-M_{\rm sph}$	$-M_{\rm disc}$	b/t	$r_{\rm sph}$	$r_{\rm disc}$	T	I
HE 0949−0122	MRK 1239	0.019	13.59	1.38	21.02	21.49	21.55	0.49	1.2	14.6	E	
						0.03	0.03					
HE 1017−0305	MRK 1253	0.048	14.26	1.68	22.10	22.30	23.07	0.33	9.0	17.8	SB	t
						0.07	0.05					
HE 1029−1831	IRAS 10295−1831	0.039	14.16	1.60	21.38	22.57	22.51	0.51	1.3	11.9	S*B*	
						0.20	0.09					
HE 1143−1810	IRAS F11431−181	0.033	13.91	1.73	22.82	<21.54	22.53	<0.29		26.6	S	m
							0.03					
HE 1310−1051	PG 1310−108	0.034	14.59	1.37	22.38	<19.81	21.80	<0.14		11.3	S	t
							0.09					
HE 1330−1013	MCG –02–35–001	0.022	13.35	1.61	21.12	20.80	22.85	0.13	2.5	21.4	SB	t
						0.02	0.03					
HE 1338−1423	CTS 0023	0.042	13.49	1.83	22.91	22.84	23.44	0.37	7.8	35.8	SB	
						0.03	0.02					
HE 1348−1758	CTS 0103	0.012	13.42	1.31	<17.28	19.66	19.65	0.50	2.1	15.5	E	
						0.07	0.05					
HE 1417−0909		0.044	15.43	1.48	21.16	22.09		1.00	7.9		E	
						0.27						
HE 2231−3722	CTS 0065	0.043	15.67	1.27	21.22	21.63		1.00	8.9		E	
						0.20						
HE 2354−3044	IRAS F23548−304	0.041	14.11	1.54	21.51	<20.86	22.86	<0.14		15.9	SB	m
							0.14					

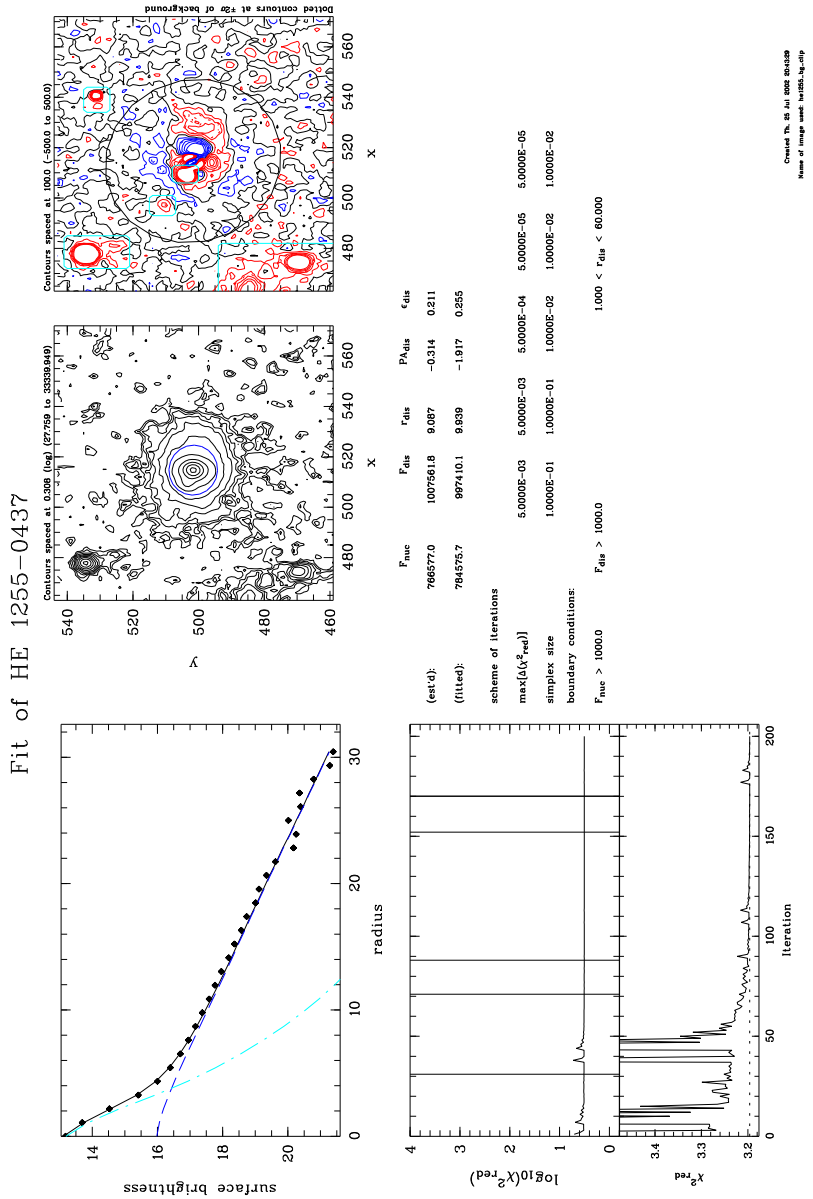

Figure 3.1. Diagnostic plot of the decomposition. We plot (left column, bottom to top): a) Profiles of the data (dots), the nuclear (dash-dot), disk (dash) and spheroid (dotted) models. b) Contour plot of the quasar an one isophote of the galaxy models. c) Contourplots of the residual and the fitting radius, excluded areas are marked by boxes here. Right column: d) Progress of the reduced χ^2 value. e) Estimated and fitted parameters, parameters of the simplex minimization and boundary conditions.

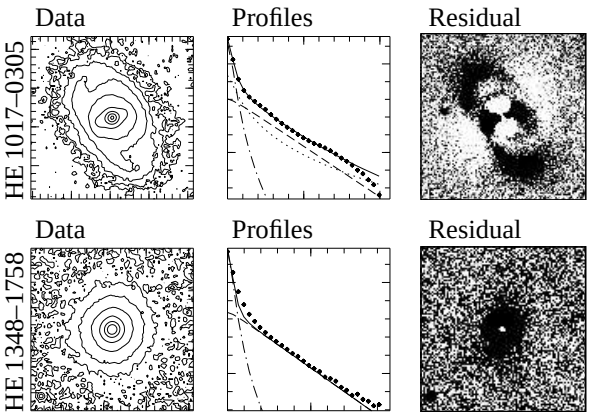

Figure 3.2. Two examples of unsatisfactory fits, requiring user intervention. For HE 1017–0305 a excessively large spheroid is fit due to surplus in surface brightness at 6″ to 9″. For HE 1348–1758 we forced an unresolved nuclear source instead of a spheroid. Notation is as in Figure 3.5.

three component fitting as described above.

The decomposition itself is protocoled in plots like Figure3.1. The main features are the profiles of each used component and the countour plots of object and residual. Any drastic discrepancy between model and data should show up here, e.g. spherical model for disk-like galaxy, wrong ellipticity and angle due to asymmetric features or a strong bar, ... If the fit converged or further tweaking is needed can be seen in Panel d). In e) finally we print the initial estimated parameter values and their final values, the scheme of iterations which defines the way restarts are done and addition boundary conditions.

The quality of each fit was investigated manually by checking the resulting profiles, residual images, the sequence of χ^2 values, and the plausibility of the parameters obtained. If a fit was not satisfactory, i.e. leading to strong residuals or to discrepancies with the object's profile which could not be attributed to prominent features in the galaxy, we spent more effort in estimating good initial conditions, or imposed additional constraints in the form of boundary conditions to ensure that the fitting results corresponded to physically meaningful components. For a few objects the three component fit suggested that two components might be sufficient to model the light distribution. For these we repeated the fit with only two components and selected that if the fit was satisfactory. We comment on a few such cases below.

For the three objects where just a nuclear and a disc component were required we estimated an upper limit for the bulge luminosity by adding compact artificial spheroids ($r_{1/2} = 1, 5, 10$ kpc) with successively decreasing fluxes. These images were fitted with both a nucleus plus disc and with a three components model. The faintest spheroid for which a three component fit is preferred (i.e. has a significantly lower $\chi^2_{\rm red}$) is then taken as limit for the detection of a spheroid in that object. We did not determine limits for the bulge size, as the sensitivity on the size drastically reduces towards low galaxy fluxes (see above).

For one object, HE 1348−1758, which did not show any nuclear component, an upper limit was estimated in a similar fashion by adding an artificial nucleus.

3.3 Results

For all of our objects we were able to obtain satisfactory fits. The objects, profiles, and residual images after subtracting the models are presented in Figure 3.5. The parameters of the best-fitting model are listed in Table 3.1.

In some of the residual images, little or no structure is left at the location of the galaxies.

This is the case for HE 1348−1758, and to lesser extent in HE 2231−3722 and HE 0949−0122. In the majority of the objects, strong features are present, mainly indicating the limitations of the azimuthally symmetric models. These morphological features will also influence the fit itself and may render it less reliable. An example is HE 1017–0305, where a pair of counter-coiled spiral arms, or tidal features, causes a significant surplus of flux at larger radii which mimics the contribution of an unphysically large spheroidal component. The resulting fit is shown in Figure 3.2. A better fit is obtained when the fitting area is restricted to regions unaffected by the extended arms (Figure 3.5, top line). Note that the difference is in the low-flux end, which visible in the profiles, but hardly in the grayscale plot.

3.3.1 Morphological types

The recovered Hubble types range from E to Sc/d, with late Hubble types marginally preferred. This is indicated from visual inspection of the data as well as from using the bulge-to-total flux ratio (b/t) to classifying our eleven objects into spheroid- and disc-dominated systems. We adopt the scheme that $1 \leq b/t < 0.48$ corresponds to E–S0, and that $0.44 \leq b/t < 0.05$ corresponds to Sa–c (Simien & de Vaucouleurs 1986). These classifications have been entered into Table 3.1, supplemented with information about the existence of a stellar bar, which we determined by eye. Note that HE 1029–1831, automatically classified as E–S0, was manually reclassified as Sa, since it clearly has spiral arms.

The frequency of early type galaxies among our sample is 36 per cent. This is less than the fraction of 55 per cent E–S0 galaxies found by Schade et al. (2000) in their sample of X-ray selected AGN with $z < 0.16$. But this may well be an effect of higher nuclear luminosities in their sample; if we apply a redshift cutoff $z < 0.05$ to the Schade et al. sample (which automatically eliminates the more luminous AGN), this fraction drops to 33 per cent which is well consistent with our findings, especially given the small numbers involved.

We can also compare the type distribution to a sample of inactive galaxies. Da Costa et al. (1998) investigated such a sample of over 5400 galaxies for the Southern Sky Redshift Survey 2 (SSRS2) with redshifts comparable to ours. They find 30 per cent E–S0 in a large range of apparent magnitudes. Even if we restrict their sample to galaxies approximately as bright as our, this figure changes little. Thus, judged from their overall morphological types, our galaxies hosting active nuclei are compatible with a random selection from inactive field galaxies.

3.3.2 Companions and evidence for interaction

To check whether the rate of major mergers is conspicuously high we compare our sample to the data by Patton et al. (2000) who investigated the frequency of dynamically close pairs and the merger rate in a subsample of the SSRS2 survey (Yee et al. 2000). The subsample is comparable to our data in both redshift range and the range of absolute magnitudes.

Within our sample we find two galaxy pairs fulfilling Patton's criteria for physical interaction (marked 'm' in Table 3.1). This leads to a rate of close companions N_c of 0.18, compared to $N_c = 0.0226$ for the SSRS2. Thus we formally expect 0.24 pairs where we observe 2. The Poissonian probability of this to occur by chance is only 0.02, but given the small sample size the effect is at best marginally significant.

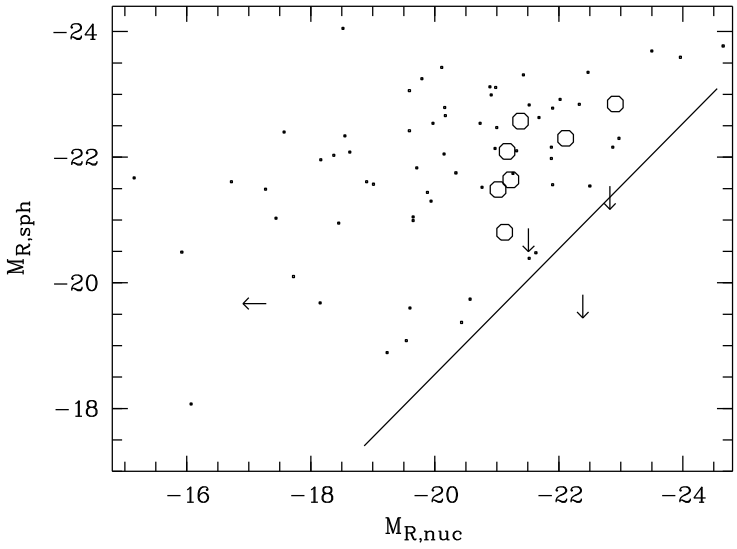

Figure 3.3. Nuclear versus spheroid luminosities. The circles are our values, dots values taken from Schade et al. (2000). Arrows indicate upper limits for one of the components. The line is the predicted upper bound for nuclear luminosities with $L \leq 0.1 L_{\mathrm{Edd}}$.

Increasing the projected radius within which pairs are called 'close' from 40 kpc to 100 kpc reveals further neighbours: A confirmed physical companion for HE 1017−0305 (at 54 kpc and line-of-sight velocity difference 221 km/s, according to NED[1]) and three companions without redshift information for HE 1417–0909. If all are at the AGN redshift, this would lead to a significant overdensity.

In three of the non-interacting galaxies we find signs of tidal interaction: HE 1310−1051 has a long (26 kpc) tidal tail and a low surface brightness companion at $r_p = 17$ kpc projected separation distance; HE 1330−1013 has a strong bar and asymmetric spiral arms, maybe as a result of a close encounter with a low surface brightness companion at $r_p = 60$ kpc and HE 1017–0305 with its tidal arms and the aforementioned companion.

While these are signs for increased gravitational interaction, we also notice that such signs are not mandatory for nuclear activity. With HE 1348−1758 and HE 2231−3722 there are two E–S0 galaxies with no signs of disturbances. HE 1029−1831 is an undisturbed spiral, although it has a pronounced 'type II' disc profile with an inner cut-off radius (as described by Kormendy 1977). But since Baggett et al. (1992) found 25 per cent of 167 spiral galaxies to be inner-truncated, our occurrence rate agrees with the general proportion among inactive galaxies.

Finally we found the frequency of bars within our sample to be 57 per cent (71 per cent if we include HE 1029−1831). This is in good agreement with inactive spiral galaxies of which 65 per cent show strong or weak bars (SB and SAB types in the Third Reference Catalogue of Bright Galaxies RC3; number quoted from Eskridge et al. 2000).

3.3.3 Luminosities

The magnitudes of the components were computed from the best-fitting model parameters, which already contains the total fluxes for each component. Other methods are possible such as using the obtained nuclear model to subtract the nuclear source and then determining the galaxy flux from growth curves of the remaining host galaxy. This method yields a more precise nuclear-to-ratio as it is strictly flux-conserving. For the goal of computing the fluxes of

[1] NASA/IPAC Extragalactic Database

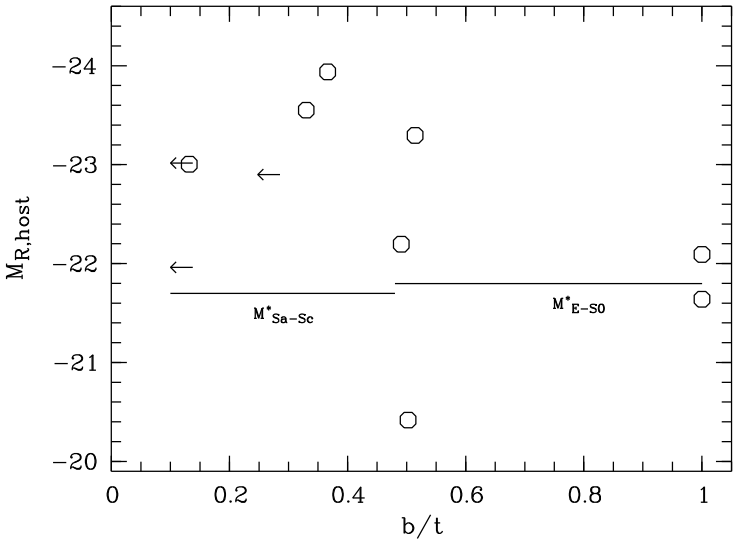

Figure 3.4. Total absolute host luminosity versus bulge-to-total relation. Values of M^* are taken from Lin et al. (1999). For the two E0 ($b/t = 1$) we did not compute upper limits for the disc, the true b/t is therefore expected to be slightly below 1.

several galaxy components separately, this is not as straightforward. For our data we tested and compared both methods and found that they agree extremely well. Fluxes taken from the model parameters are, on average, brighter by 2 per cent, with an rms scatter of $\pm$ 4 per cent. In the following we use the magnitudes derived from the fits.

Magnitude errors were estimated using dedicated simulations (sample 'low z', described in the Section 2.5) by interpolating the uncertainties of the two most similar simulated objects. In the Table 3.1 we did not include the uncertainty of the calibration, as this affects only the total magnitude. For the individual components the error will be of same amount and direction and therefore will not introduce errors in the magnitude relations. We also did not include error estimates concerning the systematic differences between fitted and observed profile.

Plotting the nuclear against the bulge/spheroidal magnitudes reveals positions in a well-known triangular area (e.g. McLeod & McLeod 2001; Kukula et al. 2001; Schade et al. 2000). For our Figure 3.3 we included the objects measured by Schade et al., using their set of transformation formulas between photometric systems:

$$\begin{aligned} B(\mathrm{AB})_{\mathrm{spher}} &= R_{\mathrm{spher}} + 1.41 \\ B(\mathrm{AB})_{\mathrm{disc}} &= R_{\mathrm{disc}} + 0.99 \\ B(\mathrm{AB})_{\mathrm{nuc}} &= R_{\mathrm{nuc}} + 0.55\,. \end{aligned} \tag{3.1}$$

The exclusion area in the lower right has been interpreted as being due to the relation between black hole mass and bulge luminosity found by Magorrian et al. (1998), coupled with the assumption of a maximum fraction of the Eddington luminosity at which an accreting black hole can radiate (McLeod, Rieke & Storri-Lombardi 1999). Adopting the approximate transformations $(R-H)_{\mathrm{sph}} = 2.22$ and $(B-R)_{\mathrm{nuc}} = 0.41$, we obtain a relation between host galaxy and maximal nuclear R band luminosities. This relation is plotted in Figure 3.3 for a maximum Eddington ratio of 0.1 All of our objects except one are consistent with radiating well below 10 per cent of L_{Edd}. Only for HE 1310−1013 the non-detection of a bulge leads to a lower limit of ~ 30 per cent L_{Edd}.

The object HE 1348−1758 is peculiar in the sense that we could not detect a nuclear source at all and concluded it must be fainter than $M_{R,\mathrm{nuc}} = -17.3$. Forcing to fit an unresolved nuclear

component with positive flux either leads to a flux of the nuclear source close this lower limit, or to a fit where the central source is clearly too narrow (see Figure 3.2). We can also exclude that our PSF is too narrow, as our model of spatial PSF variations works well for nearby stars. However, a nucleus as weak a this is not entirely uncommon: Ho et al. (1997) found type 1 AGN in ≈ 10 per cent of all local galaxies with luminosities varying by 4 orders of magnitude. The faintest AGN found has a luminosity of only $M_B = -10$ (NGC 4395, Filippenko & Sargent 1989).

We note that in our sample the disc galaxies with type Sa to Sc ($0.1 < b/t < 0.5$) are on the average 1.1 magnitudes brighter than L^* galaxies with similar redshifts and morphological types as found by Lin et al. (1999). Though the scatter is large ($1\sigma = 0.6$), this could be, together with the high rate of interaction, an indication for ongoing or recent star-forming activity. But without multi-colour or spectral data this cannot be decided.

E-S0 galaxies ($b/t \geq 0.5$) on the other hand agree with their inactive counterparts.

This and the previous chapters are based on a submitted paper written by Björn Kuhlbrodt, Lutz Wisotzki and Knud Jahnke

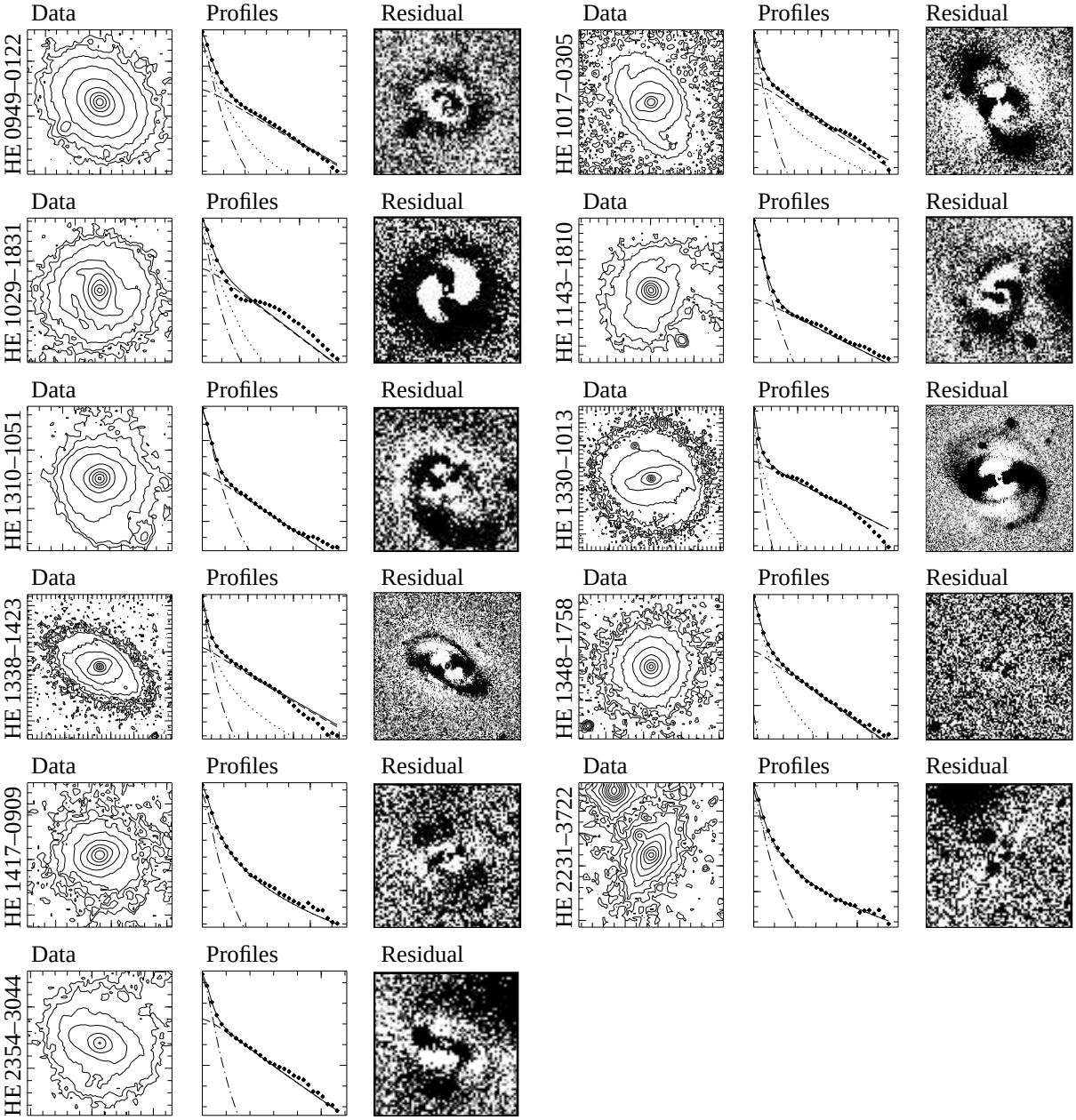

Figure 3.5. The low-redshift test sample. Left columns: contour plots, with contour spacings of one magnitude. Middle: Azimuthally averaged profiles, with dots representing the observed data and the solid line denoting the overall fit. Dashed, dotted, and dashed-dotted lines correspond to the disc, spheroidal, and nuclear model components, respectively. Right column: residual images after subtraction of all model components. Cut levels are set at $\pm$ the value of the outermost isophotes shown in the contour plots. White/black areas indicate regions where the model is brighter/fainter, respectively, than the data. Tickmarks are spaced by $1\farcs0$ in the contour plots, and by 1 mag in the profiles.

4 NIR observations of bright low-redshift Quasars

4.1 Introduction

Observations of low-redshift quasars are essential in understanding the physical connection between quasar nucleus and host galaxy. In recent years high-resolution imaging with both ground-based instruments and HST revealed a number of such connections. One of the most prominent was first described by McLeod & Rieke (1995b). They found that a galaxy of given luminosity can only host quasars fainter than cut-off luminosity which scales linearly with galaxy luminosity. This maximum nuclear-to-host (N/H) ratio was interpreted later (McLeod et al. 1999) as the maximum efficiency at which the central black hole can convert the gravitational energy from the accretion of matter into light.

Though this physical connection is suggestive and the majority of recent observations (e.g. Schade et al. 2000; McLeod & McLeod 2001) are well within the boundaries found by McLeod & Rieke, Percival et al. (2001) found a considerable number of quasars with N/H *higher* than the McLeod boundary. For a sample of luminous quasars with $M_{\mathrm{K,nuc}} \approx -28$, they found host galaxy luminosities of $M_{\mathrm{K,gal}} \approx -25$ only slightly brighter than a typical L^* field galaxy and typical for the low-luminous quasars of McLeod & Rieke. Their conclusion however has already been disputed by McLeod & McLeod (2001), arguing that Percival et al. (2001) introduced systematic errors by shifting the McLeod boundary to different filters.

To investigate this, we selected a complete sample of luminous quasars from the Hamburg/ESO survey (HES). The HES is a quasar survey which avoids selection effects caused by host galaxy properties (Köhler et al. 1997; Wisotzki et al. 2000). By selecting *all* objects within a certain area, with luminosities brighter than a given nuclear flux and with redshifts below a given limit, our sample is strictly representative. The Palomar Green Bright Quasar Survey, from which the McLeod samples were compiled, was shown to be essentially incomplete, biased and to miss luminous low-redshift quasars (Köhler et al. 1997). By observing in the near-infrared H with nuclear M_{B_J} magnitudes at hand, we also avoid colour-transformation terms and can compare directly to McLeod & Rieke. We will also trace the *evolved* stellar component, avoiding systematic brightening through starburst or an increased starformation rate.

Another connection frequently claimed is between quasar luminosity and host galaxy Hubble type: 'Luminous quasars prefer elliptical host galaxies' (e.g. Dunlop et al. 2003; Schade et al. 2000). With this sample of *bright* quasars and the two-dimensional modelling method we will be able to determine the host galaxy Hubble type and verify this claim, which recently was not confirmed by Percival et al. (2001) who found a large fraction of disk-like hosts in their bright quasar sample.

We will also use this *complete* and *unbiased* sample later in Chapter 6 to compute luminosity functions of quasars, host galaxies and bi-variate quasar/host galaxy luminosity functions.

In this chapter we will present the sample data and the results of the modelling process as well as results with respect to the connections between quasar luminosity and host luminosity as well as host morphology. A detailed analysis of the luminosity functions will be done in Chapter 6.

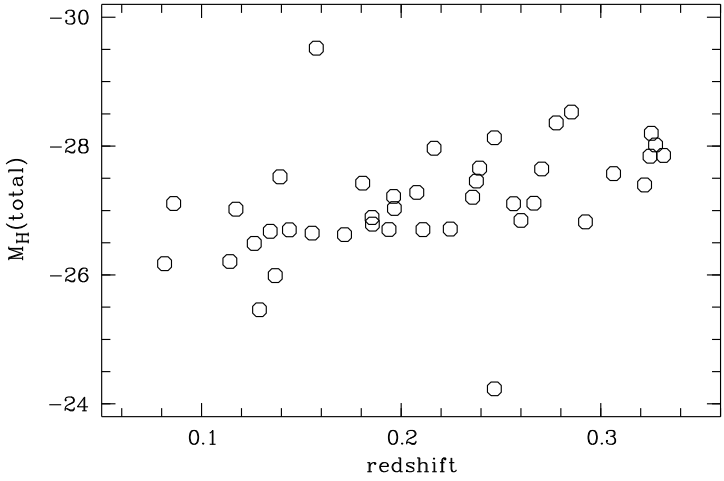

Figure 4.1. Distribution of redshifts versus total magnitudes in H.

4.2 Sample definition and observations

For the medium redshift sample we selected 44 quasars from the HES with a redshift of $z < 0.35$ and nuclear absolute magnitude of $M_{B_J} < -23$ in an area of ≈ 2200 square degrees. The distribution of redshifts and total H-band magnitudes are plotted in Figure 4.1. Special care was taken to assure that the sample is statistically complete, meaning we have clear detection for all quasars in a defined area.

The quasars were observed during two nights in February 1999 using the ESO NTT telescope with the SOFI camera in the H filter band. The seeing was generally good ($\approx 0.5''$) except for the beginning of the first night where we had a seeing $> 1''$. In order the assure constant image quality in our sample, we reduced the sample are by some 200 $\square^2$, which excludes the objected taken with bad seeing.

The sky background in the near-infrared band is both temporally and spatially variable on scales similar the quasar observations and hence has to be monitored carefully. As our objects are small and the fields being at high galactic latitudes are only sparsely populated with stars, we could determine the sky background as the median of quasar images. Each quasar observation was split up into exposures of typically 60 s with random telescope offsets with median step-width of 20 arcseconds in between using an ESO-NTT standard routine. We also took images of six NIR standard stars in the beginning, middle and end of each night. From the standard stars we derive a photometric accuracy of 0.023 magnitudes, but in the second night we had a few clouds, possibly dimming some of the objects.

During data reduction we found that the SOFI infrared array suffered from a variable bias which depends on both time since the last reset and illumination level. It also showed a spatial variation with a noticeable columnwise variation in two of the four detector quadrants. While for the flatfield we could apply the standard reduction described in the SOFI manual, we developed a special procedure for the bias subtraction. Central elements of this are: Individual sky and biasframes computed for each frame from two object frames taken before and two taken after the exposure and a quadrantwise correction of the bias residual per column.

To improve the signal-to-noise, we coadded all images of an object with each image shifted to the same centroid with prior resampling on a finer pixel grid. To fine-tune the sky background, we calculated growthcurves of the objects and adjusted the sky background level until

the growthcurves converged.

Computing absolute magnitudes requires basic knowledge of the spectral shape of both quasar and galaxy, as in our broad band H filter we observe significantly shorter rest-frame wavelengths than rest-frame H. The necessary K-correction-terms were computed assuming a simple power-law spectrum $F_\nu \propto \nu^{-0.5}$ for the quasar and a set of stellar synthesis models taken from Poggianti (1997):

$$K_{\rm nuc}(z) = -2.5(\alpha+1)\log(1+z) \quad (4.1)$$

$$K_{\rm dis}(z) = 0.1-0.25z \quad (4.2)$$

$$K_{\rm sph}(z) = 0.05-0.2z \quad (4.3)$$

with $\alpha = 0.5$. Equations 4.2 and 4.3 are linear approximations valid for $0.1 < z < 0.4$. We did not consider galactic extinction as this is small in the NIR.

4.3 Modelling

The field of view of SOFI is notably smaller than that of the DFOSC used in the low-redshift sample ($4\farcm6 \times 4\farcm6$ compared to $13\farcm3 \times 13\farcm3$) but as the images are also deeper, the number of usable stars is again typically 20 or 30 and always greater than 12. Depending on the image, a first to third order polynomial could usually represent the variation to sufficient accuracy.

The fitting of the host galaxies followed in large parts that of the low-z data. But as this sample contains objects with smaller angular extend, we initially fitted only one galactic component, either an exponential disk or a deVaucouleurs spheroid, whichever fitted the outer part of the radial profile better. For objects with ambiguous morphology or where the fit lead to systematic errors (e.g. annuli where the fit systematically over- or underestimated the data) we also tested the other option or a two-component galaxy model. The model with the lowest resulting χ^2-value while still be consistent with the morphology was finally selected. A strict χ^2-test is generally not applicable, since in the vast majority of objects both models are rejected. This is caused by the fact that host galaxies are generally more complex than can be described by a simple point-symmetric model.

In all but three cases (HE 0306−3301, HE 0311−3517, HE 0530−3755, see also Figure 4.2) the host galaxies were resolved in the decomposition process. Two of the quasars are those with particularly bad seeing. All of these belong to the sample area which was cut due to the seeing conditions. The non-detections have therefore no influence on the completeness of this sample.

As for the low-redshift Seyfert sample we tested whether determining the host galaxy luminosity from the model data and by integrating over an the nuclear-subtracted image diverge. Again we found an excellent agreement of both methods: models are only 5% fainter at a scatter of 12%. Again, we take the values derived from the models.

The results of the decomposition can be examined in Figure 4.5, as well as in Table 4.1. We also list the nuclear flux in the B-Band which we computed from the H band with an average $B_J - H = 2.8$ using the HES B_J magnitudes of our quasars and a $B_J - B = 0.1$. The scatter of the colour-transformed an measured B_J magnitudes is smaller than 0.5 mag, showing that both measurement give consistent values.

Table 4.1. The HES medium-redshift sample. Columns are: Name in the Hamburg-ESO Survey, redshift, seeing in arcseconds, total apparent magnitude in H, absolute B and H-band magnitudes of nucleus, H-band magnitudes of spheroid and disc, half-light radii of the spheroid and the disc in kpc, Hubble type (e: E–S0, l: Sa–c). Quasars set in *italics* are not part of the complete sample.

HES Name	z	s	H_T	$M_{B,\mathrm{nuc}}$	$M_{H,\mathrm{nuc}}$	$M_{H,\mathrm{sph}}$	M_{disc}	r_{sph}	r_{disc}	T
HE 0306–3301	0.247	1.1	16.62	–16.4	–19.3	–24.2		1.4		e
HE 0311–3517	0.114	1.1	12.97	–21.2	–24.1	–26.0		1.0		e
HE 0324–3652	0.211	0.8	13.96	–23.1	–26.0	–25.8		5.6		e
HE 0405–2743	0.260	0.9	14.33	–23.4	–26.3		–25.7		7.2	l
HE 0441–2826	0.155	0.6	13.35	–23.4	–26.3	–25.1		1.9		e
HE 0444–3449	0.181	0.3	12.97	–24.0	–26.7	–26.1		1.5		e
HE 0450–2958	0.285	0.5	13.03	–25.4	–28.2	–26.6		4.2		e
HE 0530–3755	0.292	0.5	14.80	–23.9	–26.7		–22.9		18.9	l
HE 0914–0031	0.322	0.6	14.46	–24.4	–27.3		–24.0		19.1	l
HE 0956–0720	0.325	0.6	13.65	–25.2	–28.0	–25.3		67.6		e
HE 1004–2144	0.331	0.5	14.01	–24.7	–27.6		–25.9		14.2	l
HE 1009–0702	0.270	0.5	13.74	–24.6	–27.5		–25.2		6.5	l
HE 1012+0048	0.185	0.5	13.38	–23.7	–26.6		–25.6		8.5	l
HE 1015–1618	0.247	0.4	13.04	–25.1	–28.0		–25.1		11.1	l
HE 1020–1022	0.197	0.5	13.51	–23.7	–26.6	–25.2	–24.6	8.2	7.9	e
HE 1029–1401	0.086	0.4	11.56	–24.0	–25.2		5.1		e	
HE 1050–2711	0.208	0.3	13.42	–24.1	–27.0		–25.5		9.3	l
HE 1101–0959	0.186	0.4	13.66	–23.4	–26.3	–25.4		3.2		e
HE 1106–2321	0.081	0.4	12.30	–22.6	–25.5		–25.2		7.6	l
HE 1115–1735	0.216	0.4	12.84	–24.8	–27.7		–26.2		15.0	l
HE 1132–0302	0.236	0.6	13.84	–24.1	–27.0		–24.7		9.2	l
HE 1149–2103	0.266	0.4	14.23	–24.0	–26.9		–24.7		4.4	l
HE 1201–2408	0.137	0.5	13.73	–22.8	–25.7		–24.3		5.0	l
HE 1205–0311	0.306	0.6	14.02	–24.3	–27.1		–26.1		22.9	l
HE 1217+0220	0.239	0.8	13.41	–24.5	–27.4		–25.6		9.8	l
HE 1222–4002	0.136	0.5	13.35	–23.3	–26.2		–24.0		5.3	l
HE 1226+0219	0.157	0.6	10.58	–26.5	–29.4		–26.3		15.2	l
HE 1228+0131	0.117	0.5	12.33	–23.9	–26.7	–25.0		1.7		e
HE 1233–2313	0.238	0.5	13.60	–24.3	–27.2		–25.3		7.7	l
HE 1236–2001	0.196	0.6	13.35	–24.0	–26.9		–25.4		8.9	l
HE 1254–0934	0.139	0.5	12.27	–24.5	–27.4		–25.0		15.7	l
HE 1255–0437	0.172	0.6	13.53	–23.0	–25.9		–25.8		10.6	l
HE 1302–1017	0.278	0.4	13.08	–25.3	–28.2		–26.1		11.1	l
HE 1312–1200	0.327	0.4	13.46	–25.3	–28.1	–26.2		2.7		e
HE 1317–0142	0.225	0.6	14.26	–23.7	–26.6	–23.9		4.2		e

continued on next page

Table 4.1. *continued from previous page*

HES Name	z	s	H_T	$M_{B,\mathrm{nuc}}$	$M_{H,\mathrm{nuc}}$	$M_{H,\mathrm{sph}}$	$M_{H,\mathrm{disc}}$	r_{sph}	r_{disc}	T
HE 1340–0038	0.325	0.5	13.96	–24.7	–27.6		–25.9		11.7	l
HE 1405–1545	0.194	0.4	13.77	–23.2	–26.1	–25.7		1.9		e
HE 1416–1256	0.129	0.5	14.12	–22.3	–25.2		–23.7		8.2	l
HE 1419–1048	0.265	0.5	14.22	–24.1	–26.9	–24.9			12.5	l
HE 1426+0130	0.086	0.7	11.41	–24.0	–26.8	–25.9			13.6	l
HE 1434–1600	0.144	0.4	13.12	–23.3	–26.2	–25.5		6.2		e
HE 1435–0645	0.126	0.7	13.06	–23.4	–26.2	–24.5		5.1		e
HE 1442–1139	0.256	0.5	13.97	–23.8	–26.6		–26.0		8.0	l
HE 1503+0228	0.134	0.6	12.99	–23.4	–26.3		–25.0		7.2	l

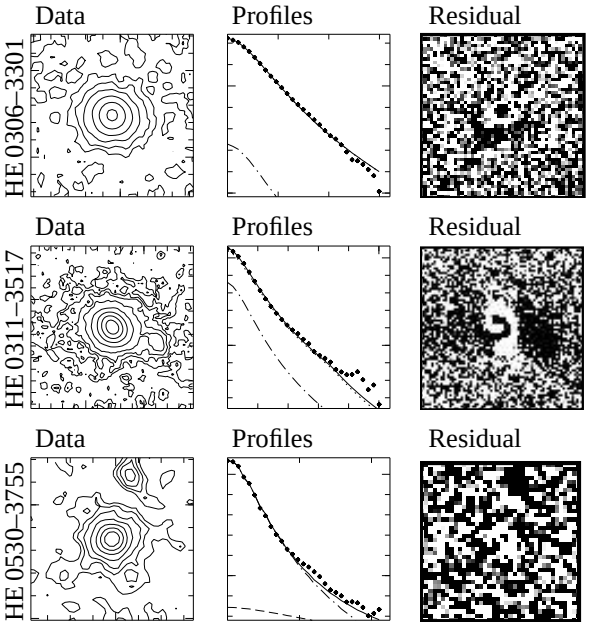

Figure 4.2. Un- or only marginally resolved objects in the HES medium redshift sample. Overplotted are the best fitting models with the notation as in Figure 3.5.

4.4 Error estimation

To estimate the systematic errors in the decomposition process we used numeric simulations, described in detail in Section 2.5 (see also Figure 2.8), which we will only briefly recapture here. The influence of the PSF determination, sky background accuracy and the decomposition were estimated by creating sets of model galaxies, created to match the data in apparent diameter, counts and background noise with various the nuclear-to-host flux relations (N/H) and were composed of a nuclear and a spheroidal component. For the sky background influence we repeated the test summarised in Figure 2.8 with a sky background typical of NIR observations. The resulting error is comparable to the optical case is still smaller than the PSF and decomposition errors.

The errors were then computed for each single object from these simulations by selecting three simulated quasars which resembled the input quasar mostly in terms of total flux and N/H and interpolating their errors. To improve the error estimate facing the significantly smaller

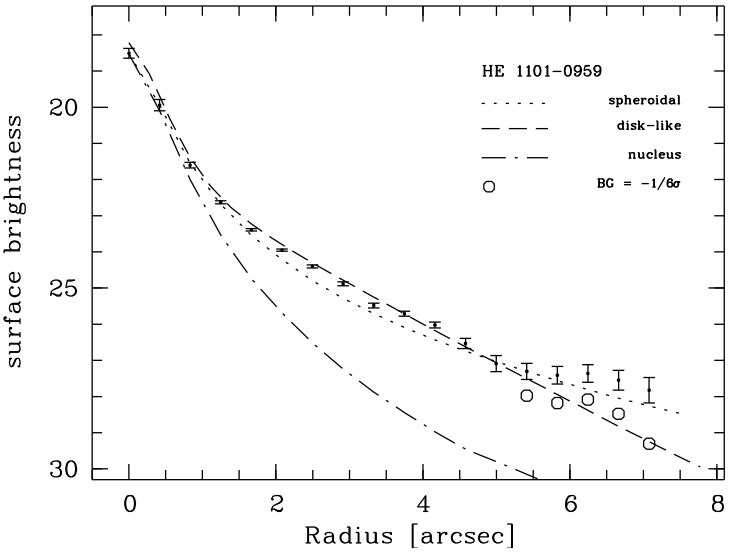

Figure 4.3. Possible mis-classification of the galactic component. We plot best-fitting composite models (nucleus and galaxy) for a spheroidal host (dotted) and a disk-like host (dashed) compared to the data (dots and errorbars) for a well resolved galaxy. For radii larger then $5''$ we also plot data points resulting from a background estimation of $1/6\,\sigma$ (5 counts) higher then the best value found (circles).

galaxies compared to the low-redshift sample, we also included errors from the determination of the PSF and sky-background. The so determined errors are plotted along with nuclear and host galaxy luminosities in Figure 4.4.

A source of errors not yet discussed is a possible wrong classification of the galactic component. For objects like HE 0914–0031 (Figure 4.5, fifth row) no clear decision can be made on the basis of a profile analysis alone. Furthermore, the background determination, while of minor importance in the decomposition process itself, can take influence on the choice of models as Figure 4.3 illustrates: The object plotted there has an exponential profile up to $5''$ radius. There the profile turns upwards like expected from a deVaucouleurs profile, but this will remain unseen if the background is only slightly misdetermined. Finally for some objects (like HE 1012+0048) neither of our analytic representations is fit to describe the radial profile.

As we do not know the true radial profile, estimation of the size of such error is not trivial. For objects for which both exponential and deVaucouleurs profiles give a reasonable description of the profile we can compare both and find that using a deVaucouleurs profile results in host galaxy luminosities brighter by ≈ 0.5 magnitudes compared to the exponential fit. However, we did not try to determine this systematic error for all of the objects but did take greatest care to use the most appropriate profile.

Ambiguities in the Hubble type determination are not unknown. McLeod & McLeod (2001) made a comparison between different schemes to detect the host galaxy Hubble type for a sample of comparable redshifts observed with HST and find large systematic differences. Percival et al. (2001) note that for their analysis of ground-based NIR imaging, the most important part of the light for the determination of the Hubble type came from large radii where the disk dominates, while for HST study it comes from small radii where a resolved spheroid dominates. From simulations they find that fitting a wrong morphological type will yield errors of only 10 %.

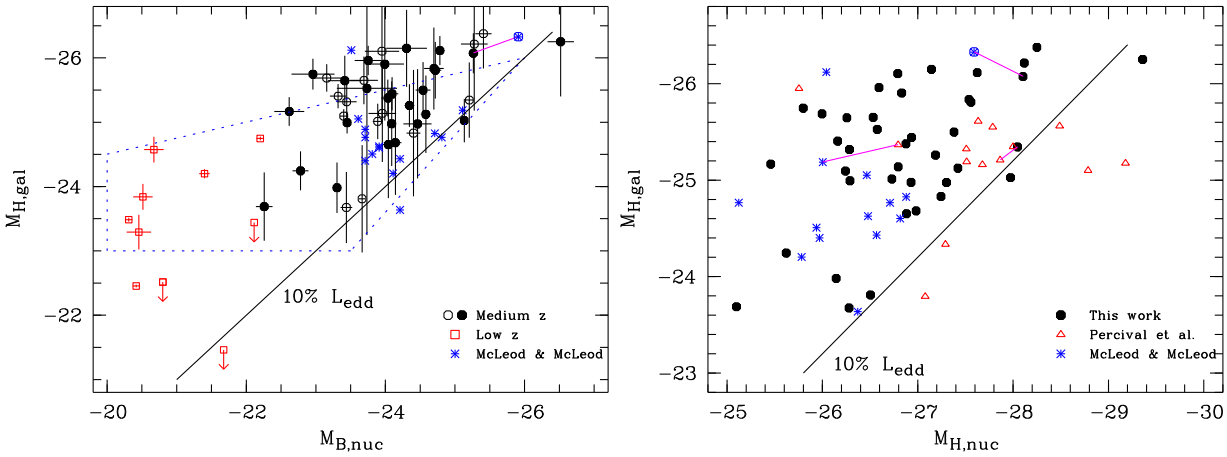

Figure 4.4. Nuclear versus spheroid luminosities in B (left) and H (right). Disks (disk-like galaxies) and circles (ellipticals) are our medium-redshift sample, boxes our low-redshift sample. Asterisks are from McLeod & McLeod (2001), circled asterisk from McLeod & Rieke (1994), the dotted quadrilateral is the range of their combined dataset. Triangles are from Percival et al. (2001) using $(H-K)_{\rm host} = 0.25$ (Poggianti 1997) and $(H-K)_{\rm nuc} = 0.95$ (Elvis et al. 1994; Glass 1981). The magenta lines connect datapoints of common objects of PERC and HES (HE 0956–0720), HES and M&M (HE 1302–1017) as well as PERC and M&M (PG 1354+213). We also plot the predicted upper bound for nuclear luminosities with $L \leq 0.1 L_{Edd}$ from McLeod & McLeod (2001) (left) and with $(B-H)_{\rm nuc} = 2.7$ from our data.

4.5 Results and discussion

4.5.1 Nuclear and galactic magnitudes

The main goal was to determine the luminosities of the nuclei and galaxies. Figure 4.4 reveals the the well-known upper bound for nuclear luminosities. Again, all of our quasars radiate below 10% of their Eddington luminosity, although it must be noted that we plot the total galaxy luminosity, not just the spheroidal or bulge part. But facing the fact that a bulge/disk separation can not be done at most of the involved redshifts, this is the best (and generally accepted) approximation.

Comparing our data to McLeod & McLeod (2001) ('M&M') and Percival et al. (2001) ('PERC'), which were recomputed to our cosmology and K-correction, we find an ambivalent picture. While in $M_{B,\rm nuc}$ versus $M_{H,\rm gal}$ we find excellent agreement with the M&M data, they find nuclei ≈ 0.8 magnitudes fainter in $M_{H,\rm nuc}$ versus $M_{H,\rm gal}$. But while the measurements of the H magnitudes were done in a similar fashion, B magnitudes by M&M are *total* B magnitudes, while the HES B magnitudes are taken only from a part of the size of the seeing disk (see Wisotzki et al. 2000 for a detailed description) and are consequently fainter. This can be seen from the example of HE 1302–1017, which is brighter in M&M by 0.7 mag in B but fainter by 0.5 mag in H. This argument is also strengthened by PERC who find a nuclei (PG 1354+213) brighter by ≈ 0.8 mag. Measurements of an object also observed by us (HE 0956–0720) on the other hand agree well to those of PERC.

While we do not fully understand the nature of these fainter nuclear magnitudes from M&M, we want to stress that the colour transformations for our data are only small due the small shift in filter bands $(H-K)$, as we have *measured* nuclear magnitudes in B and H. Percival

et al. (2001) needed a large colour transformation from R to K for which they already noted that it is very sensitive to the assumed quasar spectra. In Figure 4.4 the luminosity of their nuclei is not exceedingly bright, in particular not super-Eddington. As the HES sample overlaps with both M&M and PERC in the respective colour-colour-diagrams ($M_{B,\mathrm{nuc}}$ versus $M_{H,\mathrm{gal}}$ for M&M, $M_{H,\mathrm{nuc}}$ versus $M_{H,\mathrm{gal}}$ for Perc) without colour transformations, we want to suggest that the difference between the Percival et al. (2001) and the McLeod & McLeod (2001) data is mainly caused by the large colour transformation.

4.5.2 Morphological properties

Looking at the morphological types in our sample, we find for 37.5 % of the galaxies the early type spheroidal profile to be most appropriate. This is in good agreement with the low redshift low luminosity results and with Percival et al. (2001) who find 38 % elliptical galaxies. This it add odds with the standard picture in which luminous galaxies are predominantly elliptical galaxies (e.g. Dunlop et al. 2003). This discrepancy may be caused by different definitions and the different ability of HST and ground-based telescopes to detect the bulge resp, as argued in Section 4.4. the low surface brightness part of the disk.

We also note that we found predominantly symmetric, undisturbed host galaxies (72 %), and only small fractions of moderately (18 %) or heavily (9 %) disturbed galaxies. If major merger are responsible for nuclear activity (e.g. Toomre & Toomre 1972; Kauffmann & Haehnelt 2000), signatures of the merger should be visible in the direct images. But as opposed to our low-redshift sample the incidence of disturbed or merging galaxies in this is low. This is in accordance with studies which compare environments of samples of active and matching samples of non-active galaxies in the low-redshift regime and find no significant difference between both (de Robertis et al. 1998; Dultzin-Hacyan et al. 1999).

While this disfavours the major merger scenario (e.g. Hernquist & Mihos 1995; de Robertis et al. 1998) for medium redshifts, minor merger have have a smaller influence on the morphology of the host galaxy (Hernquist & Mihos 1995) and might be missed by us. To further investigate this, a detailed analysis of asymmetries in our samples and matched control samples as done in Corbin (2000) and Conselice et al. (2000) would be needed. Corbin (2000) do not find a significant difference between non-active galaxies and galaxies with various forms of nuclear activity in images much better resolved than ours[1]. Facing lower resolution, the low incidence of obvious asymmetries and the lack of matching control samples we do not consider our samples to be suited for such investigations.

An alternative is an analysis of the environment of the quasar in order to reveal close companions which are capable of tidally disturbing the quasar. In a large survey Salvato (2002) (summarised in section 5.2.2.3) found a significant overdensity of such companions. This however requires redshift information of all, even faint companions which we did not have at hand.

[1]The samples have $z \lesssim 0.006$.

4.6 Summary

With a complete, unbiased sample we were able to verify the McLeod boundary for luminous quasars. We argued that the super-luminosity of the quasars presented by Percival et al. (2001) may be resolved by a different colour transformation. In the data presented here, our data is both consistent with the McLeod & McLeod (2001) data as well as the Percival et al. (2001) data, which implies that they are also consistent to each other. This is even more firm as we did not have to apply colour transformations as we had both nuclear B and H magnitudes measured.

We confirm the low fraction of ellipticals among luminous quasars (38 %), previously found by Percival et al. (2001). A great majority of objects are undisturbed (70 %) and we find less then 10 % major merger.

As the sample is statistically complete and unbiased and the method of decomposition was also shown to be unbiased, this sample is suited well for the computation of quasar, host galaxy and even bivariate quasar/host galaxy luminosity functions. We will present this later in Chapter 6.

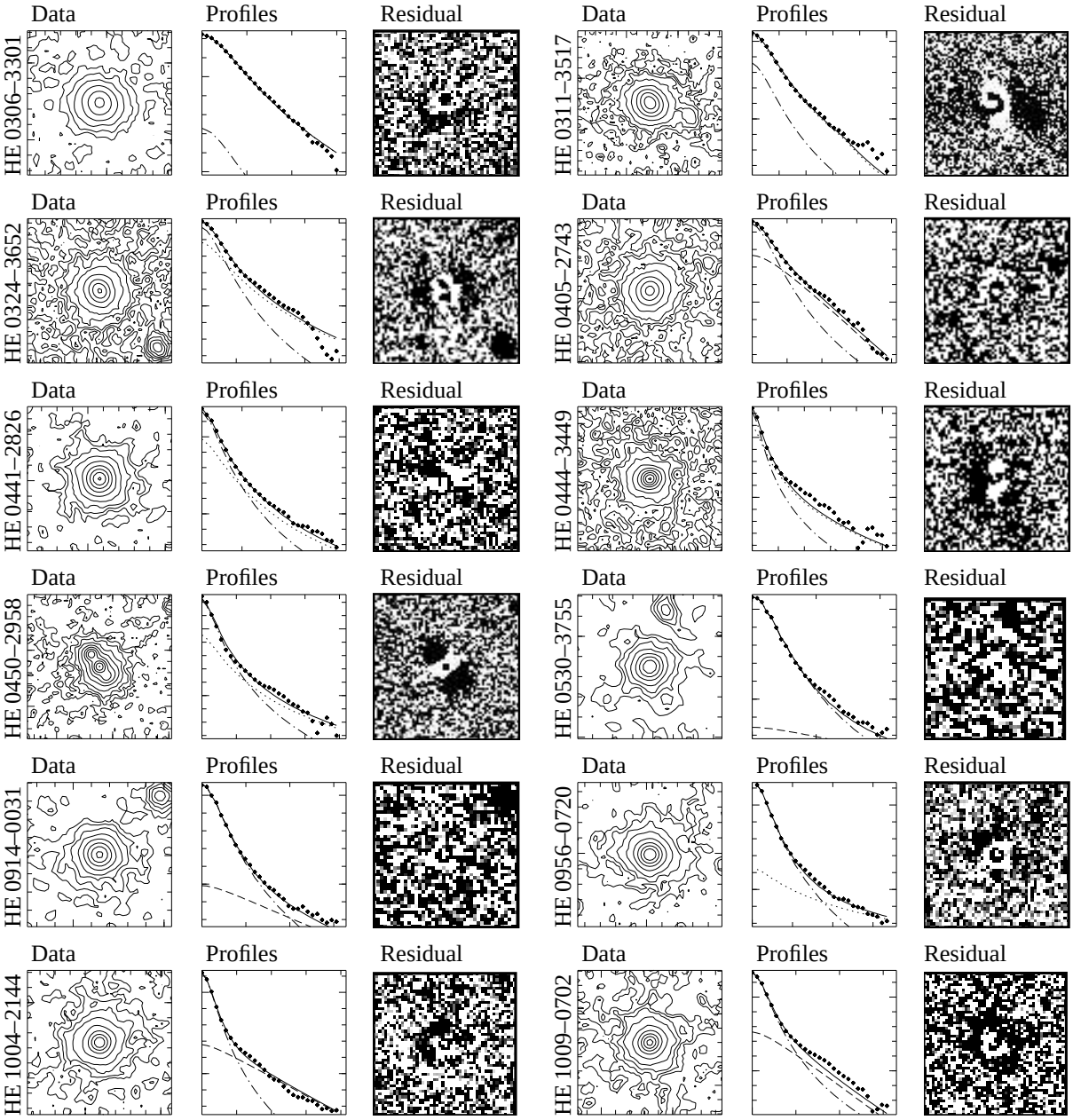

Figure 4.5. The medium-redshift sample. Left columns: contour plots, with contour spacings of one magnitude. Middle: Azimuthally averaged profiles, with dots representing the observed data and the solid line denoting the overall fit. Dashed, dotted, and dashed-dotted lines correspond to the disc, spheroidal, and nuclear model components, respectively. Right column: residual images after subtraction of all model components. Cut levels are set at $\pm$ the value of the outermost isophotes shown in the contour plots. White/black areas indicate regions where the model is brighter/fainter, respectively, than the data. Tickmarks are spaced by $1\farcs0$ in the contour plots, and by 1 mag in the profiles.

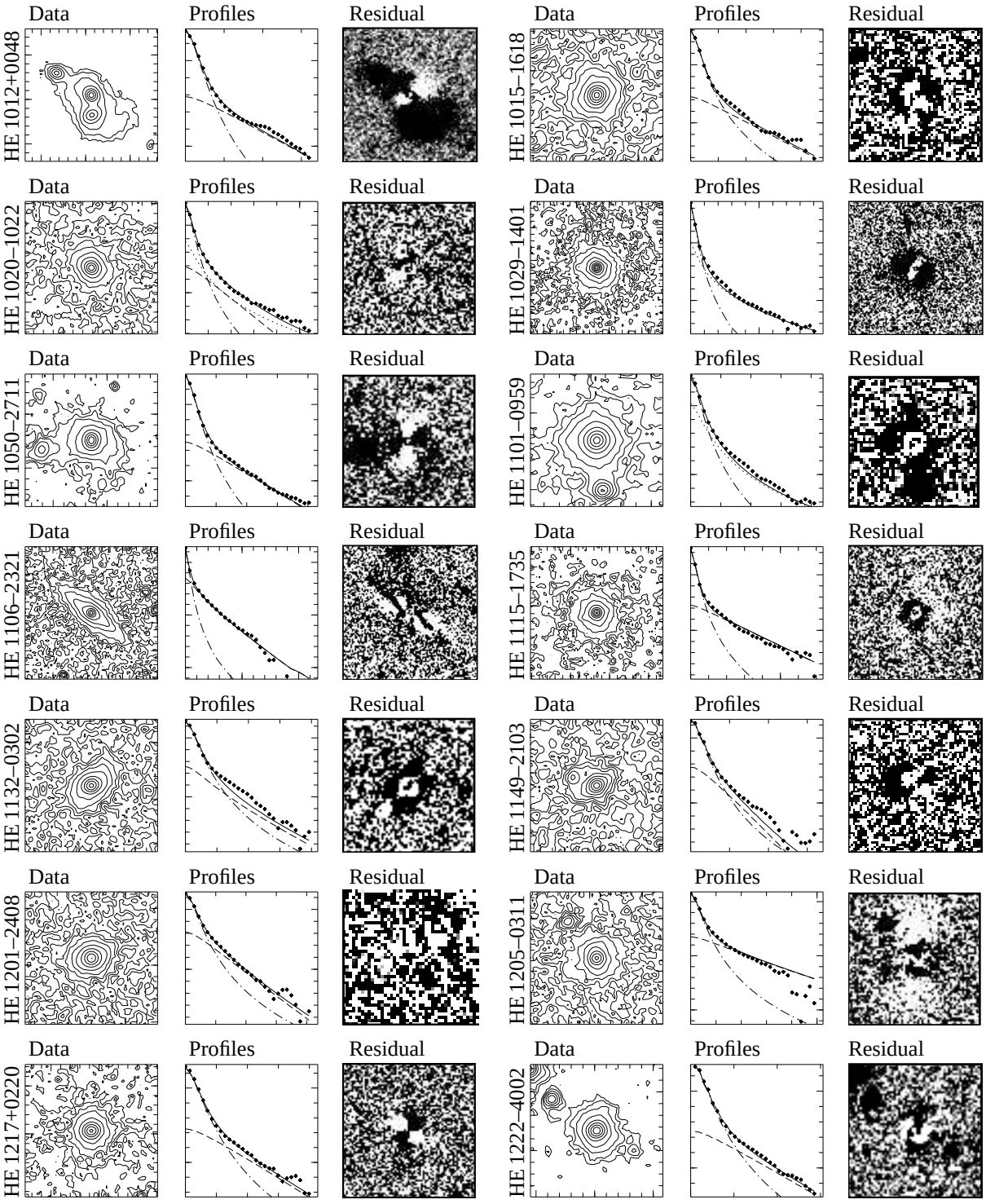

Figure 4.5. The medium-redshift sample (continued).

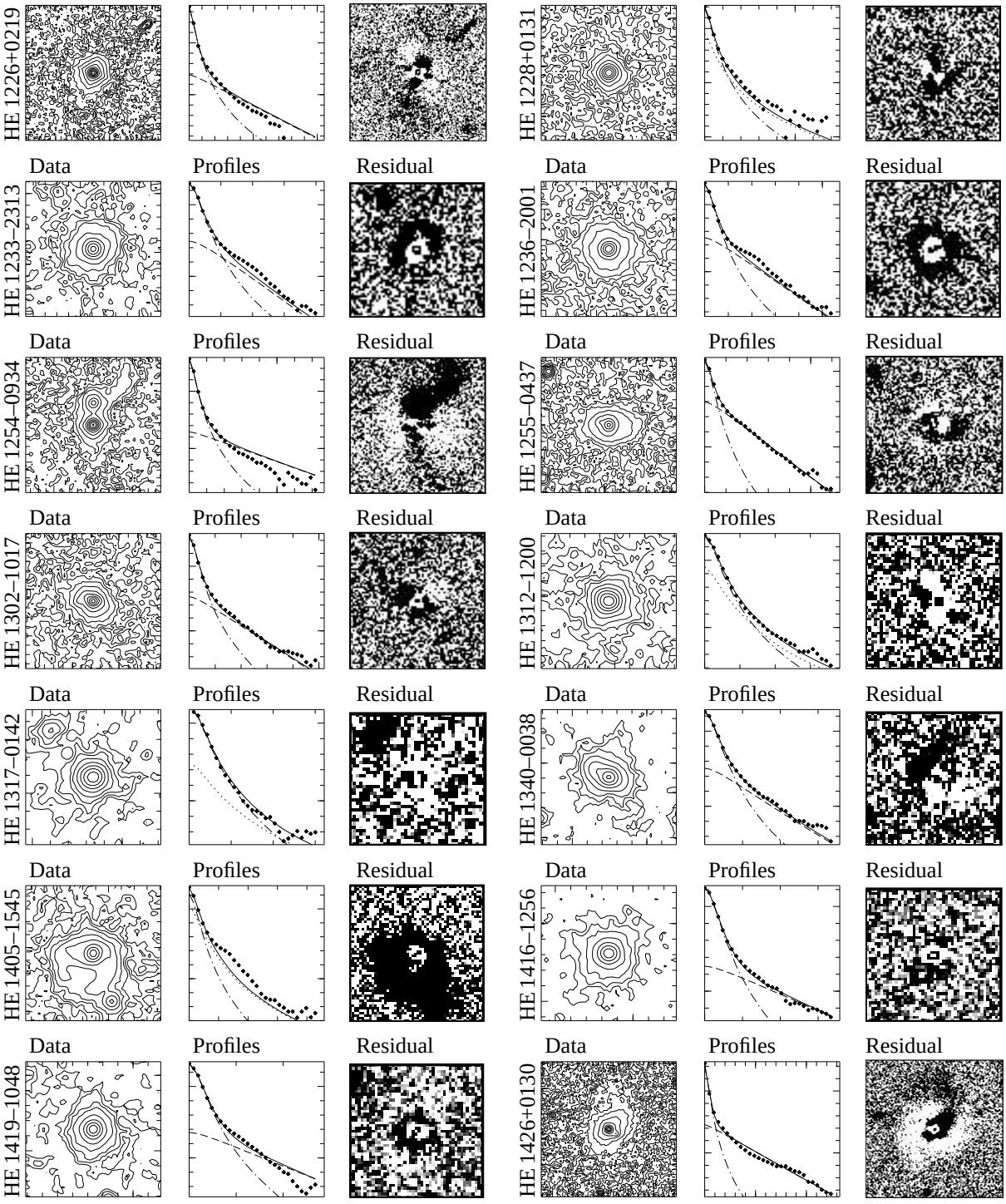

Figure 4.5. The medium-redshift sample (continued).

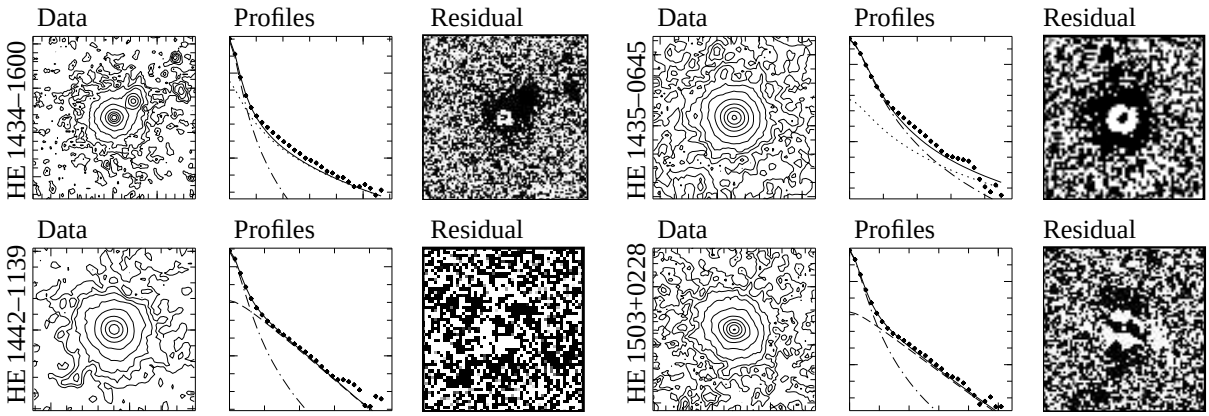

Figure 4.5. The medium-redshift sample (continued).

5 Further applications of the image decomposition

The samples presented so far are not the only ones to which the decomposition method has been applied. Here, I give a brief review of a multi-colour sample investigated by Jahnke (2002) and an X-ray selected sample analysed by Salvato (2002).

5.1 Multi-colour sample

In the past, imaging studies of quasar host galaxies were done predominantly in only one broad-bad filter, only few have a second or more filters available. From the single-colour images, luminosities and host geometry can be determined, like done in Chapters 3 and 4. A much deeper understanding of the physics of quasars can be draught from spectral information. This information, may it be in the form of a spectral energy distributions (SEDs) taken from broad or narrow-band filters or spectra, can effectively be used to determine the stellar content of the host galaxy, the age of the stellar population and to find signs of unusual star forming activity. These multi-band or spectral observation are always a lot more expensive than single-band observations, but with the advent of a new generation of telescopes many 'small' 2-m-class telescopes became available to programmes demanding extensive observing time.

With the goal of determining the stellar content of quasar host galaxies Knud Jahnke investigated such a multi-broad-band filter sample. Here I give a brief review of the results presented in Jahnke (2002). The figures and tables in this section were also taken from this work.

5.1.1 Sample and observations

The sample investigated was drawn from the HES and contains all quasars with $z < 0.2$ in an area of 611 deg^2. In order to sample a wide range of the SED all of the objects were observed in optical Johnson *B*, Bessel *V* and *R*, Gunn *i* and NIR *J*, *H* and K_s passbands. This allows us to determine the young stellar content (in the optical) as well as the old stellar population (NIR). While all of the optical passbands have an immediate diagnostic value, the three NIR band are redundant, as the typical spectral shape in that region is very smooth. But this redundancy was essential to stabilise the fits of template spectra. Furthermore for future comparison to medium or high–redshift objects, no K-correction needs to be done.

The data was acquired using mainly ESO telescopes (ESO 3.6m, NTT, 1.54m Danish). Complimentary observations (for *B*-band mostly) were taken at the 2.5m Nordic Optical Telescope. The images are similarly deep in all passbands except *B*. In this passband most of the images are acquisition images with short exposure times. We replaced them with deeper images whenever possible.

While for the short *B*-Band images we adopted standard reduction procedures, using flat-fields, a constant bias and a spatially constant sky background, we refined this for the other passbands. In *V*, *R* and *I* the sky background was computed from the objects frames themselves. The fields were sufficiently empty to compute it as the median of a set of jittered images. The sky background level was fine-tuned using growthcurves of the objects. The NIR data taken with NTT/SOFI suffered from a complicated bias variation, like the one described in Section 4.2. We were able to correct this with sky background/bias–images computed for each single image.

The dithered data, both optical and NIR, were then shifted to coincident quasar centroids on a finer pixel grid and were stacked with weighted averages. Outlier pixels created by bad columns, hotspots or cosmics were iteratively excluded.

5.1.2 Multi-colour decomposition

Processing the data in the previously described way requires some modifications beforehand. While the decomposition would run smoothly in all passbands, we want to homogeneously treat all passbands. To achieve this we used the same fitting area and the same masks (completed by unique features like cosmics or detector defects) in all passbands.

Still, an identical treatment in all passbands is hardly achievable, as the sky background drastically increases from optical to NIR. This will also lower the S/N of the host outskirts in NIR compared the S/N of the nuclear source. When fitting this, in NIR more residual error is allowed in the outskirts then in the centre. This will lead to a systematically larger error in the NIR host galaxy morphology.

To account for this we fitted all passbands with the morphological parameters as free variables, then decided for a globally valid host galaxy shape and fitted only nuclear and galactic fluxes in the second iteration. The implication that the host galaxy shape does not change in the passbands from B to K can be justified. Internally in the first iteration we find changing shapes in only two objects, all other are consistent with constant shape. Externally we can query studies of inactive galaxies (e.g. de Grijs 1998; Möllenhoff & Heidt 2001) and find that a change in galaxy shape is only common for late-type spirals, which are not known to host nuclear activity.

5.1.3 Results

5.1.3.1 Colours

Within the sample we find about half of the galaxies to be disks and half elliptical galaxies. Comparing the colours we find the ellipticals to be 0.25 magnitudes bluer in $V-K$ then the disk galaxies. Table 5.1 shows that this is not a singular datapoint, but occurs in all combinations of colours except $B-V$. As we expected to find an older, evolved stellar component in the ellipticals and a young, therefore blue, stellar population in the disks, we checked if this is an artifact of the decomposition process.

First of all we note, that the average colours are not dominated by outliers, but by the bulk of the datapoints. An effect which bluens the data must then work on each single object. Some contribution to the flux in V might we caused by quasar emission lines in the broad band filter. While we cannot exclude this, we estimate this effect to be smaller then 0.15 magnitudes.

A more suspicious factor is the decomposition itself. We have made no dedicated simulations for this data set, but it is largely comparable the simulations done in Section 2.5, where we see no systematic flux transfer between nucleus and galaxy. Also by fixing the galaxy shape for all passbands, we would expect an error equal in all colours. Such a constant flux transfer however can be shown to *redden* the spheroid.

We also compared the host galaxies to inactive galaxies, using the data assembled by Fioc & Rocca-Volmerange (1999) for the optical to NIR and NIR colours and the data by Fukugita

Table 5.1. Disk and ellipticals in the sample and comparison with inactive galaxies. For the disks intermediate type Sb is used. Sources: optical colours from Fukugita, Shimasaku & Ichikawa (1995), optical–NIR and NIR colours computed from Fioc & Rocca-Volmerange (1999) as described in the text. $I-J$ was calculated from the other colours. For $V-K$ the spread is given in parentheses.

	$B-V$	$V-R$	$R-I$	$I-J$	$J-H$	$H-K$	$V-K$
Ellipticals							
Inactive	0.96	0.61	0.70	0.77	0.71	0.20	2.99 (0.12)
QSO host sample	0.52	0.44	0.48	0.67	0.59	0.31	2.48 (0.25)
Δ	0.44	0.17	0.22	0.10	0.12	–0.11	0.50
Disks (Sb)							
Inactive	0.68	0.54	0.63	0.67	0.78	0.25	2.87 (0.36)
QSO host sample	0.55	0.53	0.53	0.87	0.57	0.24	2.73 (0.20)
Δ	0.13	0.01	0.10	–0.20	0.21	0.01	0.14

et al. (1995) for the optical colours. While disks are consistent with inactive disks, ellipticals are significantly bluer (see Table 5.1).

5.1.3.2 Stellar synthesis

To analyse the stellar content of the active galaxies, we fitted synthetic colours, derived from evolution synthesis models of single stellar populations (SSP). The corresponding spectra were convolved with the filter functions of each filter and then compared to the observed data.

By selecting one or two populations with single ages (instantaneous burst), we can estimate the age of the stars and search for evidence for starburst end eventually the time since. In Figure 5.1 we present two examples of such a fit.

For both types of galaxies we find populations of intermediate age to be the most appropriate. For the disks we need no significant young population except for two objects and none of the ellipticals requires an old evolved population.

Therefore a causal connection between starbursts and nuclear activity could not be supported, active disk galaxies are similar to their inactive counterparts. Elliptical galaxies however are significantly bluer than inactive ellipticals. Supported by measurement of emission lines from a gaseous disk in the ellipticals (described in detail in Jahnke 2002) we suggest that the ellipticals in this sample are created in the merger of two similar sized inactive disk galaxies. After a few 100 Myr the merger itself will look like a normal elliptical galaxy, but in the process enough gas is channelled to the central black hole, creating an accretion disk and the quasar.

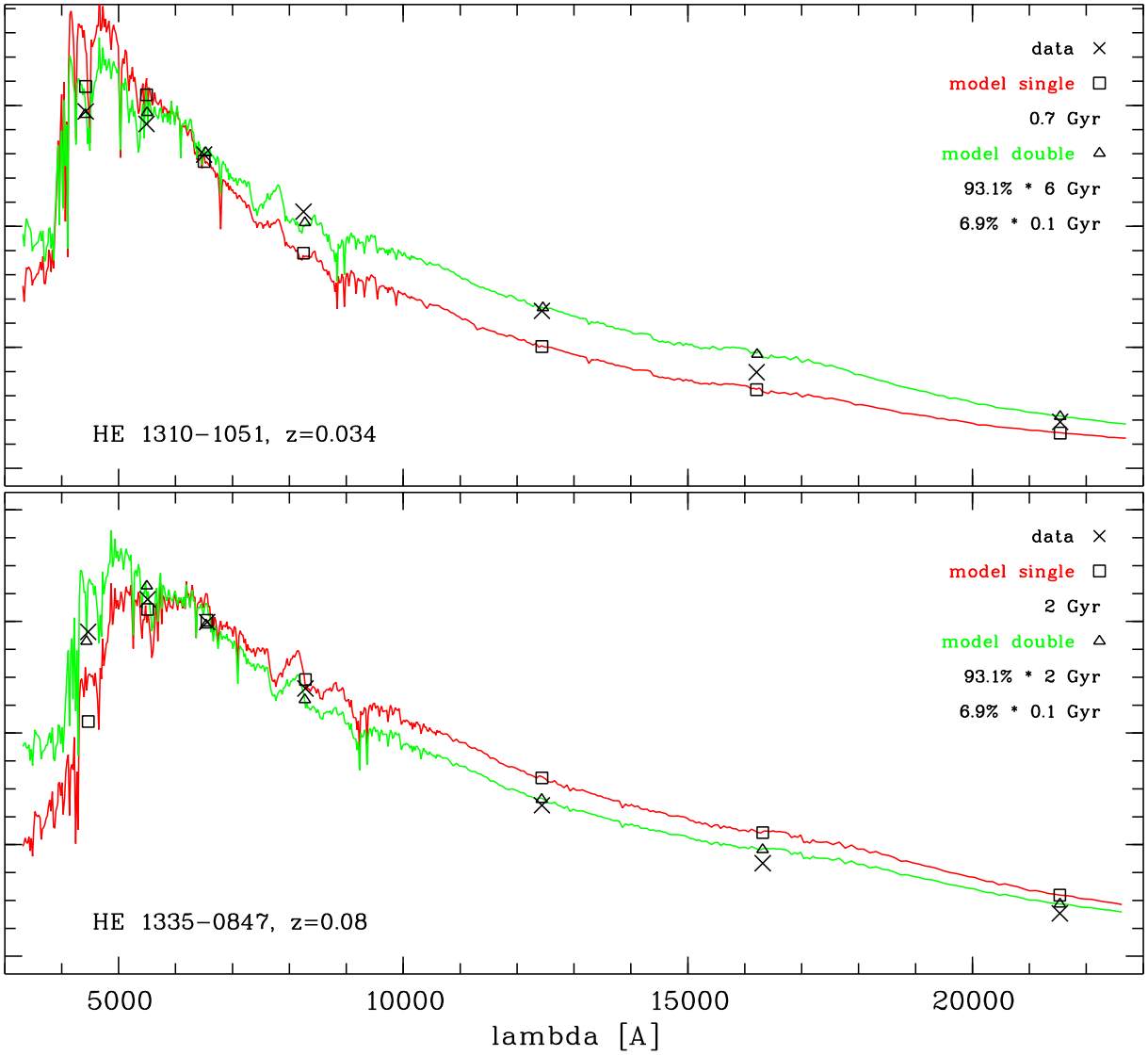

Figure 5.1. Two examples for results from model spectra fitting. Plotted are flux densities versus λ [Å] in observer frame. Data points of the *BVRIJHK* bands are marked with crosses. The SED of the best fitting 1C SSP is plotted in red, the composite 2C SED from a young, 0.1 Gyr SSP and an older population in green. The broad-band averaged fluxes of the SEDs are marked with symbols: squares for 1C, triangles for 2C. Name of the object and redshift *z* are given, as well as the ages and relative contributions of the SSPs. Top is a disk galaxy, bottom an elliptical.

5.2 X-ray selected quasars

All of the above samples were selected from the HES which selects quasars by their optical characteristics. A different approach is to use the X-ray flux emitted by quasar nuclei to detect quasar candidates. This will avoid biasing against quasars with a nucleus behind an optically thick galaxy. Optical spectroscopy is then used to detect tracers of quasar activity.

Such a sample, selected from the ROSAT bright survey, was investigated by Salvato (2002) with the goal to determine the host galaxy morphology and their environment and compare to inactive galaxies.

5.2.1 The X-ray sample

Out of the some 700 quasars found the ROSAT bright survey, Salvato (2002) selected 93 quasars with $0.009 < z < 0.1$ and a ROSAT count rate of $c > 0.3/\mathrm{s}$ in the hard band 0.5 – 2.0 keV. All objects were observed using the 1.23m telescope on Calar Alto and the ESO 1.54m Danish telescope on La Silla. For all objects *R*-Bands images were acquired with additional *V* and *B*-band images for some of the objects.

For all of the objects two-component fits as well as both single component fits for the galactic component have been carried through, using a preliminary version of the decomposition software, which did not include modelling of spatial variation of the PSF. The decision which model to use was then done on the basis of profile an residual plots as well as the final χ^2 values.

Fitting all possible galaxy models allows to test whether the nuclear component is independent of the galaxy model. Figure 5.2 shows that is is the case for most of the objects. Only faint spheroids are scattered largely. While in a single component model, the spheroid is needed to describe the entire galactic flux, in a two-component model it can be used as a correction to a sub-optimal nucleus. Flux of the nucleus can such by misassigned to the galaxy. This is not the case for the disk component, as the spheroid can more easily adopt the shape of the PSF.

Note that in the early version of the decomposition method, a spatially variable PSF has not

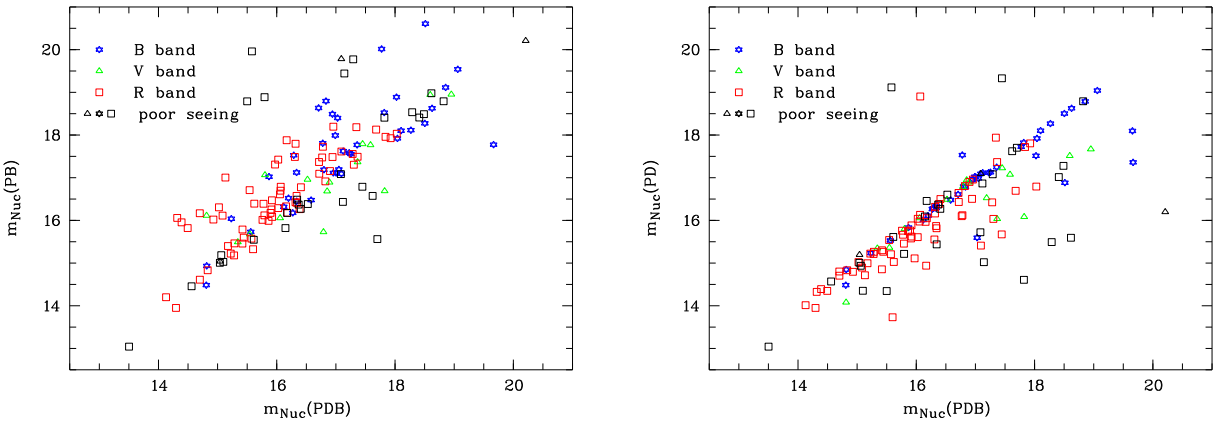

Figure 5.2. The magnitude of the nuclear component for different decompositions in different bands (see legend) is plotted. The nuclear luminosity for spheroid only (left panel) and disk only (right panel) configuration is plotted versus the nuclear luminosity in disk and spheroid configurations. The plots show that the majority of the points lie on the line of unity.

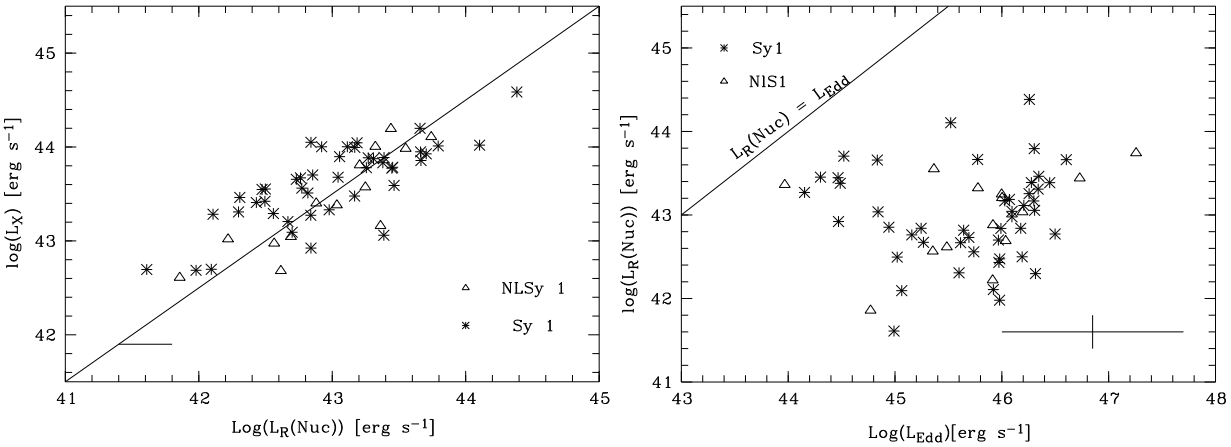

(a) Optical vs. X-ray luminosity

(b) Optical vs. Eddington luminosity

Figure 5.3. Optical luminosity versus X-ray (left) (in 0.5 – 2 keV rest-frame) and Eddington luminosity (right). $L_{\rm edd}$ has been computed with $L_{\rm edd} = 1.3 \times 10^{30} M_{\rm BH}/M_{\odot}$ erg s^{-1} using the Kormendy & Gebhardt (2002) relation $\log(M_{\rm BH}/M_{\odot}) = -0.5 M_R - 2.91$. The solid line in the left frame represents the line of direct proportionality shifted by 0.5 dex.

been implemented. As we have shown that the determined quasar PSF critically influences the accuracy of the fitted parameters, the size of the scatter is not completely unexpected, retrospectively.

5.2.2 Results

5.2.2.1 X-ray flux

In Figures 3.3 and 4.4 we plotted the line of 10% efficency in terms of $M_{\rm nuc}(M_{\rm spheroid})$. The underlying principle is that a black hole can radiate only at a maximum efficiency (the Eddington efficiency) at a large range of wavelengths (over 4 orders of magnitude). It is therefore interesting to check whether this relation holds up for nuclear X-ray or radio magnitudes.

In Figure 5.3a we can see that there is a clear relation between the nuclear luminosities in X-ray and optical passbands with $\log L_X \approx \log L_R + 0.5$ in units of erg s^{-1}. The source of this relation is unknown but it is hypothesised that the correlation could either be the influence of the X-ray flux directly on the pseudo-black-body continuum of the accretion disk or an effect of the degree of ionisation of Hydrogen which can dominate the measured R band flux through the H_α emission line. A similar relation is also found for the radio flux at 1.4 GHz.

So together with the finding in the optical that, again, quasars radiate below 10% $L_{\rm edd}$ (Figure 5.3b) it is safe to say that the McLeod boundary holds for other nuclear passbands. This is an expected result, as the basis of the McLeod boundary is a physical model of the efficiency of quasar accretion. The measurement of the nuclear luminosity is only a step in the determination of the black hole mass and should be independent from the observed wavelength.

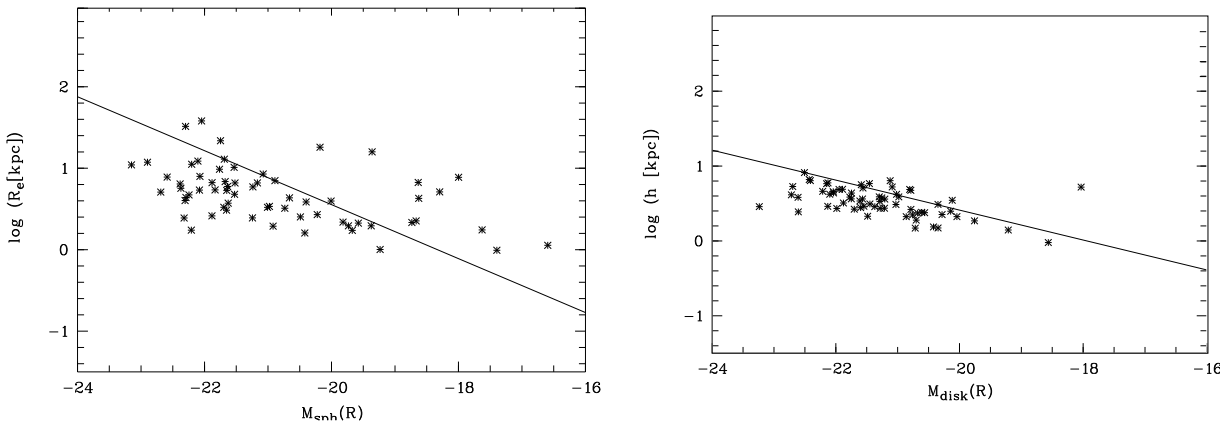

Figure 5.4. Effective radius versus absolute magnitude for spheroidal component (left panel) and scale length versus absolute magnitude for the disk component (right panel). Solid lines represent the usual correlations valid for elliptical and spiral galaxies.

5.2.2.2 Morphology

Comparing the radii of disk and spheroid to values predicted from Kormendy (1977) and Freeman (1970) (Figure 5.4) Salvato finds that the relation for the disk galaxies is well confirmed. For the spheroids the accordance is less obvious, especially as the data is not as steep as the predictions. The errors however are large, data and prediction are therefore statistically compatible.

Within the sample 49% of the galaxies are of early type, classified by their b/t ratio. This however classifies galaxies with clear bars or spiral arm as early type. A visual inspection reveals, that about 50% of all early type galaxies show such features. This underlines the importance of a thorough observation of the fitting process as described in Section 3.2. This leaves only 25% of early type galaxies, less than in the other samples presented here, but not significantly so.

5.2.2.3 Environment

In order to compute the frequency of gravitationally interacting systems among the quasars, the environment of each quasar was searched for galaxies. Using the Digitized Sky Survey candidates were selected and correlated to the NASA/IPAC Extragalactic Database. For the candidates for which no redshift was available, long-slit spectroscopy has been performed in Asiago (1.8 m telescope), Calar Alto (2.2 m telescope) and La Silla (1.54 m telescope).

Salvato defines a galaxy to be a companion when the tidal inter-galactic forces on the stars of the Seyfert galaxy are stronger than the intra-galactic forces. Computing these forces Salvato showed that the tidal forces of nearby low mass companions are comparable to that of high mass companions at larger distances. Using this criterion she found companions for 40% of the whole sample. If also candidates for merger remnants and double nuclei are considered, then the number of Seyfert galaxies which reside in interacting systems increases to 60%. This strongly supports the model of triggering the AGN activity by galaxy interaction.

6 Luminosity function of quasar host galaxies

6.1 Introduction

The luminosity function (LF) of a population is a fundamental characteristic and a powerful tool to compare different populations or estimate the evolution of a population. Luminosity functions have in computed by several groups for quasars (QLF) (e.g. Grazian et al. 2000; Wisotzki et al. 2000; Boyle et al. 2000) as well as galaxies (GLF) (e.g. Huang et al. 2003; Kochanek et al. 2001; Cole et al. 2001; Loveday 2000; Lin et al. 1999), but so far only one attempt was made to compute the quasar *host galaxy* LF (HGLF) (Hamilton et al. 2002). By combining quasar observations available in telescope archives, they compiled a sample of 71 quasars with $z < 0.46$ and $M_V < -23$. With this data they concluded that *all* bright galaxies host a quasar. From this it follows that bright quasars in the local universe are *constantly* active and *constantly* accrete matter. This would lead to large masses of the central black holes and greatly constrain quasar evolution models. But the inherent incompleteness of their sample required a complicated correction which is susceptible to large systematic errors.

With a sample of 44 luminous quasars with $z < 0.35$ and $M_{B_J} < -23$ selected from the Hamburg/ESO survey, supplemented by a sample of 66 less luminous, X-ray selected quasars analysed by Schade et al. (2000), we can test their claim with a sample which is *complete* and *unbiased*. Furthermore, we plan to extend the concept of a HGLF to a bi-variate quasar/host galaxy LF (QHGLF), which describes both QLF and HGLF simultaneously an can incorporate possible dependencies between both, of which the maximum nuclear-to-host ratio (N/H) found by McLeod & Rieke (1995b) is the most prominent. With this approach we will also test other dependencies like nuclear luminosity versus hostgalaxy luminosity.

Once the QHGLF is computed, we can compare to the GLF and determine the fraction of galaxies which shows nuclear activity. Using a simple argument we can estimate a lower bound for the time a field galaxy is active, the quasar dutycycle.

6.2 Samples

In order to compute a QHGLF the sample has to fulfil at least two criteria: it needs to be complete and unbiased. Incompleteness will yield a LF which is systematically to low, possibly coupled to quasar or host galaxy properties. For optically selected quasar samples for example, detection of low-luminous nuclei in bright galaxies gets increasingly harder. The amount of incompleteness will hence depend on the relation between quasar nuclear and host galaxy luminosity (N/H). The second effect to be considered is biasing against a class of objects during the sample selection. If a bias passes unnoticed or uncorrected the deducted results are also biased. Finally, the methods of analysis need to be free of systematic errors or shifts. A method which has been shown to yield unbiased results by several groups is the two-dimensional fitting of quasar images (see Chapter 2, Schade et al. 2000, Taylor et al. 1996).

In this chapter we consider two samples, one optically selected sample from the HES described already described in detail in Section 4 (labelled ‘HES’ for short now, tough it is only a small subset of the HES) and an X-ray selected sample from the Einstein Medium Sensitivity Survey (EMSS) which has been analysed and published by Schade et al. (2000).

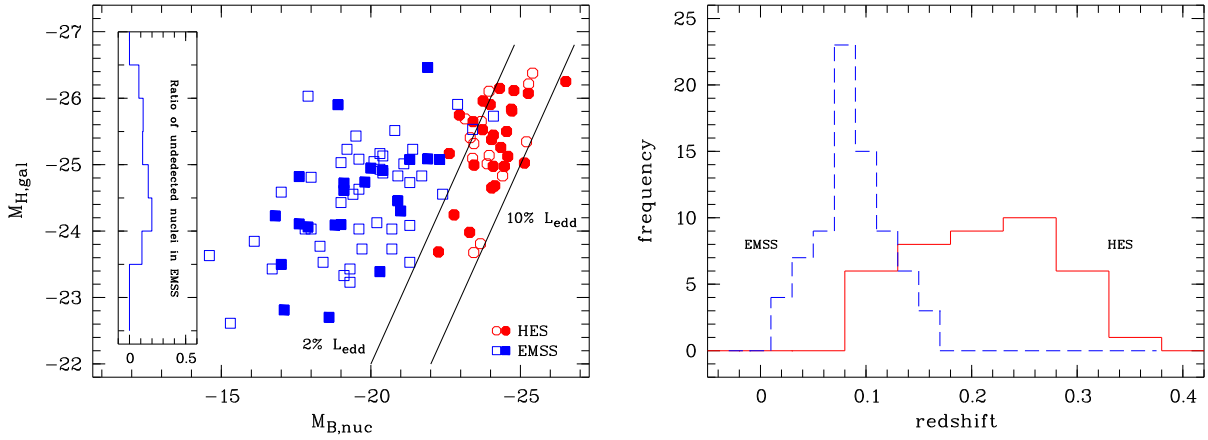

(a) Nuclear to galactic luminosity

(b) Redshift distribution

Figure 6.1. Comparison of the samples drawn from the HES and the EMSS. Left: Nuclear to galactic magnitudes, empty symbols represent early-type galaxies, filled late-types. Two lines are plotted for 2% and 13% Eddington ratio which fit the samples best. We also plot the frequency of undetected nuclei in the EMSS sample as a fraction of total number of galaxies within a host magnitude bin. Right: The redshift distribution of EMSS (dashed) and HES (solid).

The HES subsample is complete and unbiased in the sense that it contains *all* quasars from the HES with a redshift of $z < 0.35$ and nuclear absolute magnitude of $M_{B_J} < -23$ in an area of ≈ 2200 square degrees. While it was found that the HES does not miss a sizeable fraction of the known quasar population (Wisotzki et al. 2000), it is a bright quasar survey of which we selected only the brightest, yielding a range in total quasar luminosities of only 3 magnitudes (see Figure 6.1a).

The second sample we consider will significantly extend this range. Schade et al. selected sample of 93 low redshift ($z < 0.15$) quasars from the EMSS, which contains a complete X-ray selected quasar sample with optical identifications. This offers the possibility to sample quasars with lower N/H as X-ray selected quasars are not biased against (optically) dominant host galaxies. Combining fainter optical luminosities ($m_B < 20$) and the more local redshift distribution (see Figure 6.1b) results in a distribution of quasar nuclei much fainter than the HES, plotted in Figure 6.1a.

The sample however is not complete. Only 76 objects of the input list were observed with HST in snapshot mode and the ground-base telescopes JKT on La Palma, Spain and MSSS0 on Mount Stromlo, Australia in 1993 – 1998 in F814W (I), R and B passbands. Further 10 quasars are lost during the subsequent two-dimensional image analysis, as their nuclei could not be seperated from the galaxy light. The histogram in Figure 6.1a shows that the non-detections are distributed roughly evenly across the range of host galaxy luminosities.

The image decomposition method applied is comparable to our method, with two main exceptions: First, the PSF is determined from typically five stars in the field (for ground based images) or from images of a stellar cluster (HST), but spatial PSF variation is not modelled. Second, the models were fit to all passbands simultaneously, which greatly stabilises the fit.

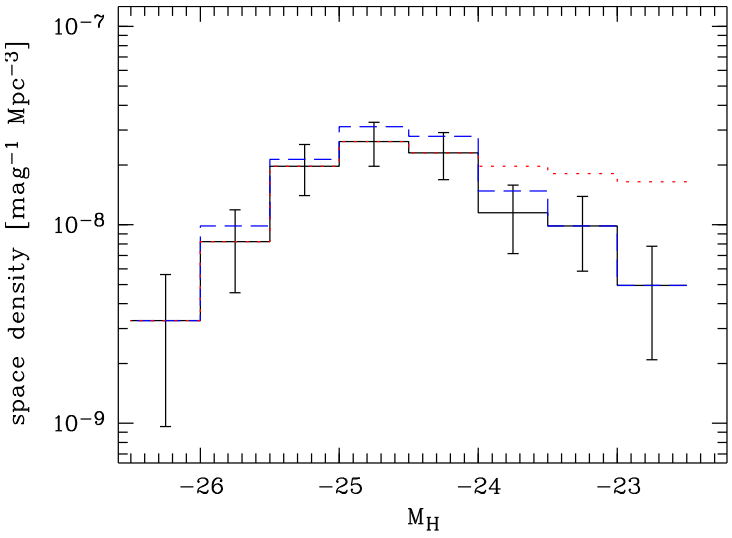

Figure 6.2. Binned LFs for the EMSS sample. Solid line is the original LF, dashed is the LF corrected for ten unresolved host galaxies, the dotted LF contained unobserved objects attributed to the faint end. 1σ Poisson errors are plotted for the original sample (solid line).

As opposed, in the multicolour sample by Jahnke (2002) we achieved a consistent model for all wavelengths by computing universally valid morphological parameters from individual fits. These parameters where then fixed during a second iteration.

To estimate the influence of these missing quasars to the luminosity function, we computed nuclear luminosities on the basis of the measured X-ray luminosity. Between both we find a good relation and compute a transformation so that the X-ray magnitudes are on average the same as the measured *B*-band magnitudes:

$$< m_x > \stackrel{!}{=} < m_B > \quad \Rightarrow \quad m_x = -2.5 \log \frac{f_X}{\mathrm{erg\,cm^{-2}\,s^{-1}}} - 11 \tag{6.1}$$

In Figure 6.2 we plot the host galaxy luminosity function. The solid line is the LF for the final sample (66 objects), dashed for that containing the unresolved objects (76), dotted for a sample where we have randomly added 17 objects so that the faint-end slope is maximally flattened (93 objects) (labelled EMSS or EMSS_{66}, EMSS_{76} and EMSS_{93} from now on). This worst case scenario implies that observations preferred the bright sources, which is not completely unreasonable.

Surface densities of several quasar samples plotted in Figure 6.3 for the X-ray and *B* luminosities illustrate that. When comparing the surface densities computed from the EMSS sample to that of the entire EMSS, we see a widening gap between both for quasars fainter than $2 \cdot 10^{-12}$ erg^{-1} cm^{-2} down to the survey limit of 10^{-13} erg^{-1} cm^{-2}. This is even more visible in the optical, where the EMSS subsample contains a considerable number of quasars less then optical selected. But this discrepancy has no influence on the host galaxy LFs, because they are normalised with the corresponding quasar LF, hence only the different number-magnitude relations of Figure 6.3a will be important.

What also can be determined from either plot, is that the area of the EMSS subsample and the EMSS are likely to be the same *for the bright objects*, as the surface density of bright quasars agrees well to both known X-ray and optical surface densities. This allows the computation of total space densities at least for the bright quasars. For faint quasars the EMSS subsample misses a number of objects, yielding space densities systematically too low.

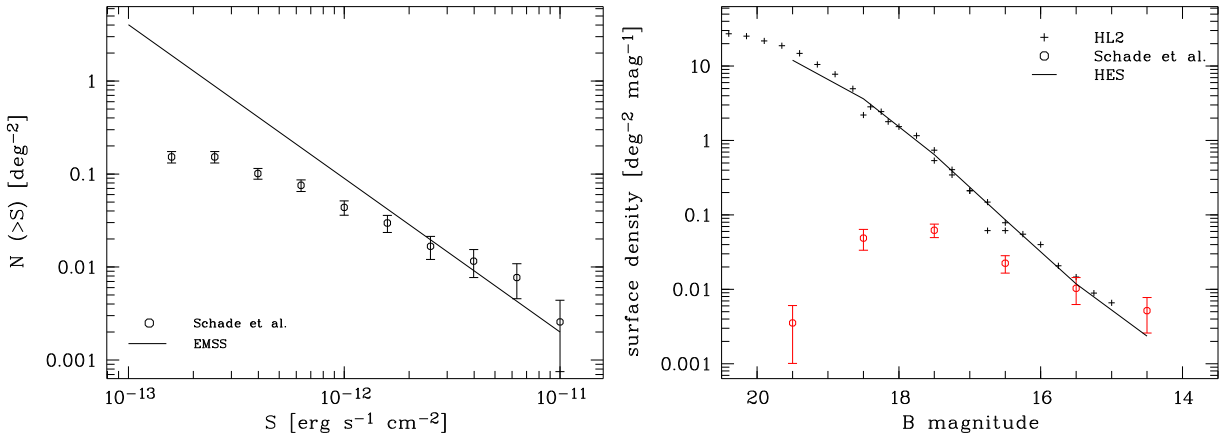

(a) Integral X-ray surface density

(b) Differential optical surface density

Figure 6.3. Quasar number – magnitude relations for the X-ray (a) and optical (b) luminosities. We also plot the relations for the entire EMSS from della Ceca et al. (1992), the combined relation for the HES, LBQS and 2dF surveys ('HL2'; Steffen Nehls, priv. comm.) and an analytic best-fit to the HES by Wisotzki (1998).

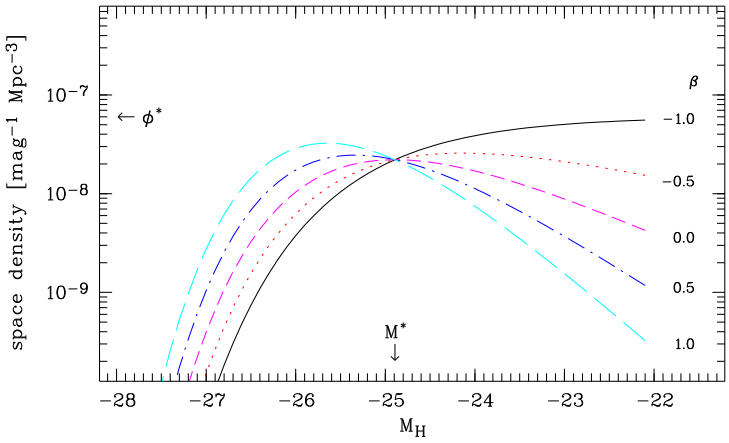

Figure 6.4. The Schechter distribution for various values of the faint-end slope β. Note that M^* is not the position of the maximum.

6.3 Computing luminosity functions

We have already shown several luminosity functions, but before we start to develop the bivariate quasar host galaxy function, we need to fully understand the mathematical principles behind them.

6.3.1 Description of the LF

The luminosity function of a class of objects, quasars or galaxies, describes their density in space as a function of their luminosity. If $\mathrm{d}N(M,x) = \Phi(M^*,x)\,\mathrm{d}V$ is the number of objects with $M = M^* \pm \mathrm{d}M$ in the Volume $\mathrm{d}V$ at the point in space x, then $\Phi(M^*,x)$ is the *differential luminosity function*, which we call simply *luminosity function* in this chapter. As we expect no dependence of $\Phi(M^*,x)$ with angle in space, at least no one we can measure, we will use $\Phi(M^*,z)$ with z as the redshift of the object. Other descriptions are common using the luminosity L instead of the total magnitude M. As we are applying this to data from optical observations we chose to use magnitudes. Aside this luminosity function there is the *integral* or *cumulative luminosity function* $\Psi(M^*,z) = \int_{M^*}^{\infty} \Phi(M,z)\,\mathrm{d}M$ giving all objects brighter than M^*.

The most simple way to express both Φ and Ψ is in binned form like done in Figure 6.2. While some of the dangers connected to binning can be circumvented, an analytic representation is of great value to actually compare different luminosity functions. A number of analytic representations exist of which four are the most important:

$$\Phi_{\mathrm{power-law}} = \Phi^* \left[10^{-0.4(M-M^*)}\right]^{\alpha+1} \tag{6.2}$$

$$\Phi_{\mathrm{broken\,power-law}} = \begin{cases} \Phi^* \left[10^{-0.4(M-M^*)}\right]^{\gamma_1+1} & : \quad M \leq M^* \\ \Phi^* \left[10^{-0.4(M-M^*)}\right]^{\gamma_2+1} & : \quad M > M^* \end{cases} \tag{6.3}$$

$$\Phi_{\mathrm{Boyle}} = \Phi^* \left[\left(10^{-0.4(M-M^*)}\right)^{-(\gamma_1+1)} + \left(10^{-0.4(M-M^*)}\right)^{-(\gamma_2+1)}\right]^{-1} \tag{6.4}$$

$$\Phi_{\mathrm{Schechter}} = \Phi^* \left[10^{-0.4(M-M^*)}\right]^{\beta+1} \exp\left(-10^{-0.4(M-M^*)}\right) \tag{6.5}$$

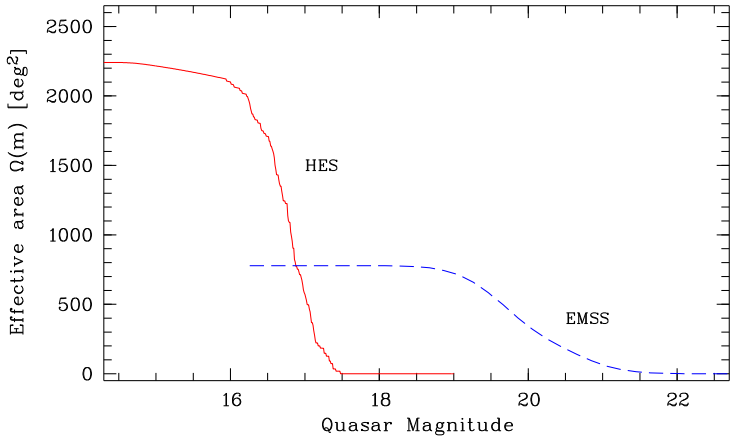

Figure 6.5. Selection functions for the HES (full) and the EMSS (dashed). Quasar Magnitude is in *B* Band for the HES and X-ray with $m_x = -2.5 \log f_x - 11$ for EMSS taken from Gioia et al. (1990). For the redshifts of our sample objects neither has a redshift dependency.

All of these serve different purposes:

- $\Phi_{\mathrm{power-law}}$ is in the normal representation of a differential LF ($\log\Phi$ against M) a straight line. It cannot be more than first estimate: The integral $N = \int_{-\infty}^{\infty} \Phi(M)\, \mathrm{d}M$ diverges, hence the total number of object is infinite. In this description M^* is arbitrary. Though simple, it can well be used for small samples as ours, Figure 6.6b illustrates that.

- $\Phi_{\mathrm{brokenpower-law}}$ is a composite of two straight lines leading to a break at M^* which better fits observed QLFs, but is unphysical due to the abrupt change in the slope. We will use this for a description of the QLF in X-ray.

- Φ_{Boyle} is a smooth version of the latter, defined by Marshall (1987) and Boyle et al. (1988) and the most frequent parametrisation of the QLF. Though not needed in the course of this work we list it due to its great importance.

- $\Phi_{\mathrm{Schechter}}$ is the Schechter-function (originally described by Schechter 1976) which is most frequently used as description of the GLF, for example in Figure 6.8, and will be used as parametrisation of the host galaxy LF later on. In Figure 6.4 we plot $\Phi_{\mathrm{Schechter}}$ for a range of different faint-end slopes β.

6.3.2 The selection function

When computing space densities of objects, a pivotal point is to know the survey volume, which is determined by the survey selection criteria. The survey volume will depend on the angle Ω of the sky surveyed and of the redshift accessible to the survey. If the quality of the survey images varies, Ω will depend on the apparent magnitude of the object and may even depend on object redshifts. We compile these selection effects in a survey function $\Omega = \Omega(m, z, \ldots)$ which gives the accessible area as a function of object magnitude, redshift and possibly other properties. The volume in which such a quasar could move around without losing the detection is then:

$$V_a = \int_{z_1}^{z_2} \Omega(m', z') \frac{\mathrm{d}V}{\mathrm{d}z'}\, \mathrm{d}z' \qquad \text{with} \quad m' = m'(M, z') \tag{6.6}$$

with $M = M(m, z)$ the quasar absolute magnitude.

Figure 6.5 shows the selection functions of the featured samples. The HES selection function was computed specially for this sample, for the EMSS sample we used the selection function of the entire EMSS from Gioia et al. (1990), as we do not know the exact selection criteria of the EMSS subsample.

6.3.3 Estimation of LF

Once the accessible volumes are computed for each quasar, a LF can easily be computed as the sum over the inverse accessible volumes (Schmidt 1968):

$$\Phi(M,z) = \sum_{M-\Delta M}^{M+\Delta M} \sum_{z-\Delta z}^{z+\Delta z} \frac{1}{V_a} \qquad \text{and} \qquad \Psi(M,z) = \sum_{-\infty}^{M} \sum_{z-\Delta z}^{z+\Delta z} \frac{1}{V_a} \tag{6.7}$$

While these are good to visualise the data, one has to bear in mind that binning always mixes different objects together. Especially in areas where the LF is steep, the binned LF will be flattened. This does not apply to cumulative LF, but that is particularity insensitive in the faint end, where the derived space densities are mutually depended.

To these empiric functions, analytic functions can be fitted using for example the χ^2-minimization which was so effective in the image decomposition. It requires however a form of binning, and hence inherits all its drawbacks.

A method to determine a best fitted analytical LF which does not require binning is the maximum-likelihood-method. The idea behind the method is to maximise the a posteri probability with which the data was observed.

If we consider sampling the LF a poissonian process, then the probability to observe k quasars in a small redshift and magnitude interval is:

$$p(k,M,z) = \frac{<n>^k}{k!} e^{-<n>} \qquad \text{with} \qquad <n> = \Phi(M,z)\,\Omega(m,z)\frac{\mathrm{d}V}{\mathrm{d}z'}\,\mathrm{d}z' \tag{6.8}$$

$<n>$ is the expected number of quasars. If the redshift and magnitude intervals are sufficiently small, k will be either 0 or 1. The probability to observe a sample of quasars with an assumed LF is then:

$$L = \prod_{\Delta M,\Delta z} <n> e^{-<n>} \Delta M_i \Delta z_i \cdot e^{-<n>} \Delta M_i \Delta z_i \tag{6.9}$$

The function L is called likelihood function. The best fitting set of parameters shall be called the set which maximises L and hence the a posteriori probability with which we have taken our data.

Instead of maximising L we rather minimise $S = -\ln L$. The change of sign is simply a matter of convenience, as most code for finding extrema are actually minimizing. Computing the maximum of $\ln L$ instead of L does not move the maximum, and greatly facilitates the computation of derivatives. Also we can drop constant terms, as these too do not change the position of the minimum.

The resulting term to be minimized is then:

$$S = \sum_i -\ln\Phi(M_i,z_i) + \int_{z_1}^{z_2}\int_{M_1}^{M_2} \Phi(M,z)\Omega(m(M,z),z)\frac{\mathrm{d}V}{\mathrm{d}z}\,\mathrm{d}z\,\mathrm{d}M \tag{6.10}$$

Finding a convenient form of Φ and evaluating S will be the task of Section 6.5.1.

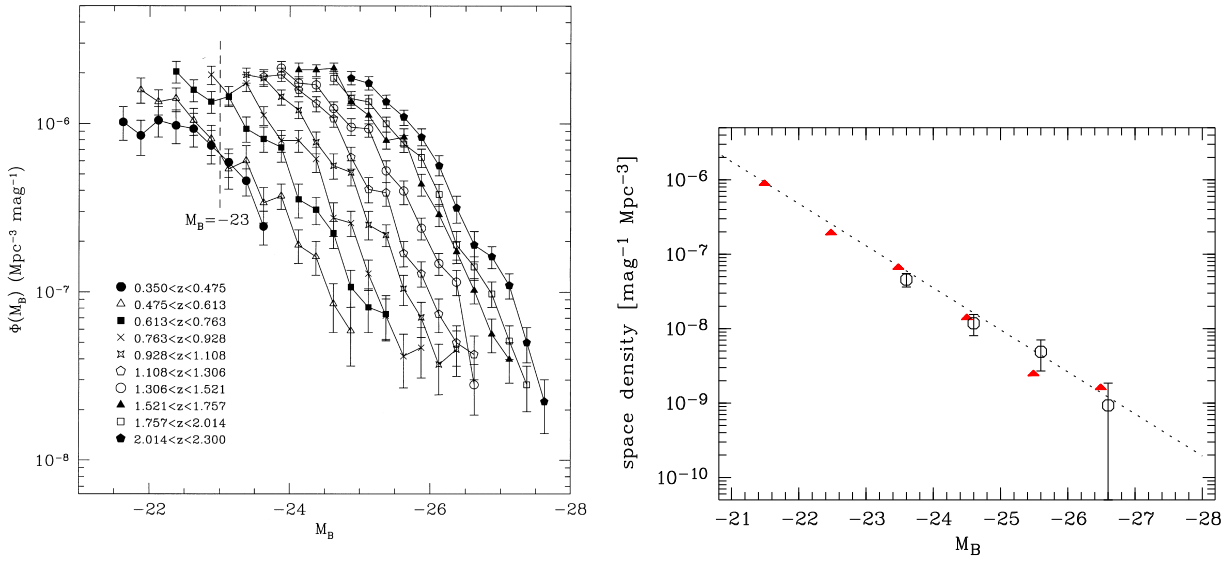

(a) QLF by Boyle et al. (2000)

(b) HES QLF

Figure 6.6. Differential quasar luminosity functions. Left: QLFs for various redshifts $z > 0.35$ from Boyle et al. (2000). Right: local QLF for $0.02 < z < 0.3$ from Wisotzki (2000) (triangles) and this work (circles). The line is the best linear fit corresponding to a single power-law QLF ($\Phi(L)\ \mathrm{d}L \propto L^{-2.4}$).

6.4 The quasar luminosity function

The quasar LF and its evolution with redshift is one of the most important diagnostics to test models of quasar evolution, and several works on the QLF exist (e.g. Boyle et al. 2000; Wisotzki 2000). Here we will briefly summarise some of the results important for the computation of the host galaxy LF.

For a large sample of over 6000 quasars Boyle et al. (2000) computed luminosity functions for a number of redshift bins. By looking at Figure 6.6 it becomes obvious that quasars evolve. With higher redshift, the QLF is shifted towards higher luminosities. This is predicted from the 'pure luminosity evolution (PLE)' model. This assumes that quasars did change in luminosity but not in comoving number density: We now have fainter, not fewer quasars.

This image has been challenged by Wisotzki (2000), who investigated a sample of 415 quasars drawn from the HES. Evolution effects found by him cannot be explained with PLE, instead he finds all shape-conserving evolution models to be incompatible with his observations. This includes the 'pure density evolution' (PDE), where quasars evolve only in number density (we now have fewer, not fainter quasars). Instead he finds a variation of the shape of the QLF with redshift. In particular, he finds no turn-off point in the $z < 0.3$ data, as others have done before (see references in Wisotzki (2000)). Instead, it is fitted well by a single power law, as done in Figure 6.6b.

A direct comparison of the QLF of the low redshift bin (160 quasars with $0.01 \leq z < 0.3$) from Wisotzki et al. (2000) with our data shows compatible results for the QLF. In Figure 6.6b the excellent agreement between both is obvious. Note also, that the 'local' HES QLF is very well fitted with a single power-law with exponent $\alpha = -2.4$ (Equation 6.2).

Consequently the evolution in this redshift regime can be approximated well with not only

PLE but also PDE, as both are indistinguishable for single-power-law LFs. To facilitate the computation we will use PDE, a (perfectly sufficient) approximation valid for only this special case.

6.5 The host galaxy luminosity function

All analytic forms of luminosity functions so far presented are space densities for a single magnitude. This is not the only possible form. If more than one magnitude is measured, the luminosity function can be expressed bivariate (e.g. optical and radio luminosities), trivariate (e.g. radio/optical/X-ray) or even multivariate (e.g. a number of wavebands).

We will use this approach to formulate a bivariate quasar/host galaxy luminosity function (QHGLF).

6.5.1 The bivariate QHGLF

With the decomposition process quasars are no longer a source with a single luminosity disturbed by a hopefully small amount of galactic light. After decomposing a quasar we have both the luminosities of nucleus and galaxy. We can therefore extend the normal luminosity function to a bivariate QHGLF $\Phi = \Phi(M_{\rm nuc}, M_{\rm gal})$. Initially we assume that HGLF and QLF are formally uncorrelated. We can then write: $\Phi = \Phi_{\rm nuc}(M_{\rm nuc})\Phi_{\rm gal}(M_{\rm gal})$ This implies that the nucleus does not influence the luminosity of the galaxy and vice versa. But in figure 4.4 we already saw one correlation: the 10% Eddington-limit boundary which states that there must be a certain host galaxy luminosity in order to host a luminous nucleus. We code this by using a Heavyside function of the form:

$$\mathcal{H}(M_{\rm nuc} + m_{\rm cut} - M_{\rm gal}) = \begin{cases} 1 & : \quad M_{\rm gal} \leq M_{\rm nuc} + m_{\rm cut} \\ 0 & : \quad M_{\rm gal} > M_{\rm nuc} + m_{\rm cut} \end{cases} \tag{6.11}$$

For the LF components we select functions which describe the respective population appropriately. For the HES QLF part we select a single power-law. The EMSS QLF taken from Boyle et al. (1993) is parametrised as a broken-power-law. For the galaxy LF a Schechter function is currently generally accepted model. We also include pure density evolution in the form $\Phi(z) = \Phi_0(1+z)^k$. So we finally have:

$$\begin{aligned} \Phi^{\rm HES}_{\rm HGLF} &= \Phi_{\rm power-law}(\alpha, M^*_{\rm nuc}, \Phi^*_{\rm nuc}, M_{\rm nuc}, z) \cdot \\ &\quad \Phi_{\rm Schechter}(\beta, M^*_{\rm gal}, \Phi^*_{\rm gal}, M_{\rm gal}, z) \cdot \\ &\quad (1+z)^{\kappa} \cdot \mathcal{H}(M_{\rm gal}, M_{\rm nuc}, m_{\rm cut}) \end{aligned} \tag{6.12}$$

$$\begin{aligned} \Phi^{\rm EMSS}_{\rm HGLF} &= \Phi_{\rm broken\,power-law}(\gamma_1, \gamma_2, M^*_{\rm nuc}, \Phi^*_{\rm nuc}, M_{\rm nuc}, z) \cdot \\ &\quad \Phi_{\rm Schechter}(\beta, M^*_{\rm gal}, \Phi^*_{\rm gal}, M_{\rm gal}, z) \cdot \\ &\quad (1+z)^{\kappa} \cdot \mathcal{H}(M_{\rm gal}, M_{\rm nuc}, m_{\rm cut}) \end{aligned} \tag{6.13}$$

with 7 (EMSS: 8) free parameters: $\alpha(\gamma_1, \gamma_2)$, $M^*_{\rm nuc}$, $\Phi^*_{\rm nuc}$, β, $M^*_{\rm gal}$, $\Phi^*_{\rm gal}$, $m_{\rm cut}$, κ. Given the sample sizes of < 70 objects, fitting all parameters simultaneously is not advisable and not necessary as we have external information about the QLF. In both optical and X-ray the QLF has been determined in samples much larger than ours. As implied previously for the optical QLF we use

the one by Wisotzki et al. (2000), from where we also draw the information about evolution, and Boyle et al. (1993) for the X-ray QLF.

Using Equations 6.12 and 6.13 in Eq. 6.10, we have a merit function which should be minimized in order to find the best fitting parameters. For this we adapted the downhill simplex minimization, with two restarts after local minima have been found. To estimate confidence intervals we also ran a full gridsearch, computing S for an array of parameters, but restricted to two free parameters only, those with the largest influence on S. The other parameters were fixed to the values found in the simplex minimization.

We also have to keep in mind that the Maximum Likelihood estimator as well as the confidence intervals only deliver the best-fitting parameters and their uncertainties, and no information about the quality of the fit. To check whether the estimated LFs are compatible with the data, we adopted a two-dimensional Kolmogorov-Smirnoff-test (Press et al. 1995) by computing a model sample from the best-fitting QHGLF with ten times as many members as the data samples. We preferred this over the comparison of data samples to analytical fits for reasons of computational speed and the ability to visualise both LF descriptions.

6.5.2 Results

To demonstrate the versatility of the bivariate QHGLF we will test several scenarios in this section:

1. The host galaxy population is uniform and can be modelled with a single distribution function, the Schechter function (model 'simple').

2. The LF of elliptical and disk-like host galaxies differ from each other and have to be modelled separately (subsamples 'early' and 'late').

3. The host galaxy distribution depends on the nuclear luminosity. In particular the characteristic luminosity M^* and the slope β of the Schechter distribution are tested for dependency (models 'm_Π I', 'm_Π II' and 'β_Π')

In Table 6.1 we list the resulting Schechter parameters for all these tests. Details are given in the following sections.

6.5.2.1 The universal HGLF

Assuming the HGLF can be modelled with a single Schechter function, does the space distribution of quasar host galaxy resemble that of the field galaxies?

Figure 6.7 shows the principal results, numerical values and KS-probabilities are listed in Table 6.1 (model: 'simple', sample: 'all'). To compute the HGLF we assumed that the QLF $\Phi_{\rm QSO}$ is known. The HGLF is then:

$$\Phi_{\rm gal}(M_{\rm gal}) = \frac{N(M_{\rm gal}-\Delta M/2 < M_{\rm gal} \leq M_{\rm gal}+\Delta M/2)}{< N_{\rm QSO}(M_{\rm gal}-\Delta M/2 < M_{\rm gal} \leq M_{\rm gal}+\Delta M/2) >}\Phi_{\rm QSO} \tag{6.14}$$

with binsize ΔM, the measured number of galaxies N and the expected number of quasars with host magnitudes in the bin $< N >$. This has to be done binwise as the number of quasars depends

Table 6.1. Best-fitting parameters for several models and samples along with ϕ^* in 10^{-7} Mpc^{-3} mag^{-1} and KS probability. $P_{KS} < 0.05$ is considered a rejection. Parameters which were fitted are set **bold**. For comparison we also list several field GLF and one cluster GLF. Here ϕ^* in 10^{-3} Mpc^{-3}.
†: using $H-K=0.25$, ‡: using $R-H=1.96$

HES	QLF: $\alpha=-2.4$, $M^*=-23$, $\phi=1.3\,10^{-7}$								
sample	model	β	M^*_{gal}	m_{cut}	m_Π	β_Π	$M_{nuc,lim}$	ϕ^*	P_{KS}
all	simple	**0.04**	**–24.8**	**0.27**	0.0	0.0	-	1.04	0.014
early	simple	**0.30**	**–24.6**	0.27	0.0	0.0	-	0.40	0.005
late	simple	**0.41**	**–24.8**	0.27	0.0	0.0	-	0.54	0.014
all	m_Π I	0.04	**–24.7**	0.27	**0.09**	0.0	**–22.7**	1.03	0.040
all	m_Π II	0.04	**–24.8**	-	**0.96**	0.0	**–23.3**	0.99	0.002
all	β_Π	0.04	**–24.6**	0.27	0.0	**–0.25**	**–21.0**	0.94	0.098

EMSS	QLF: $\gamma_1=-3.2$, $\gamma_1=-1.7$, $M^*=-20.3$, $\phi=1.4\,10^{-6}$								
sample	model	β	M^*_{gal}	m_{cut}	m_Π	β_Π	$M_{nuc,lim}$	ϕ^*	P_{KS}
all	simple	**1.00**	**–24.1**	**–2.09**	0.0	0.0	-	0.61	0.019
$EMSS_{93}$	simple	– 0.30	–24.8	–2.09	0.0	0.0	-		
early	simple	**1.40**	**–23.6**	–2.09	0.0	0.0	-	0.23	0.007
late	simple	**0.60**	**–24.3**	–2.09	0.0	0.0	-	0.39	0.081
all	m_Π I	1.00	**–24.1**	–2.09	**0.06**	0.0	**–18.0**	0.59	0.031
all	m_Π II	1.00	**–23.7**	-	**0.41**	0.0	**–17.7**	0.54	0.001
all	β_Π	1.00	**–24.1**	–2.09	0.0	**–0.44**	**–18.7**	0.55	0.391

Galaxy Luminosity Functions				
Type	β	M^*_{gal}	ϕ^*	Reference
FGLF	–1.16	$-24.8^{\dagger}$	1.50	Loveday (2000)
FGLF	–0.93	$-24.6^{\dagger}$	1.45	Cole et al. (2001)
FGLF	–1.09	$-24.7^{\dagger}$	1.45	Kochanek et al. (2001)
FGLF	–1.38	$-25.0^{\dagger}$	1.63	Huang et al. (2003)
CGLF	–1.31	$-24.8^{\ddagger}$		Yagi et al. (2002)

on the host luminosity at least over the maximum Eddington luminosity. A global normalisation as done in Hamilton et al. 2002 will lead to larger values for Φ_{gal} for bright hosts and lower values for faint hosts: If we replace $< N_{QSO}(M_{gal}-\Delta M/2 < M_{gal} \leq M_{gal}+\Delta M/2) >$ with the average $\overline{N_{QSO}}$, the denominator in (6.14) will be smaller for bright and larger for faint galaxies, as there are more bright host galaxies than the average number and fewer faint. This can explain the shape of their HGLF plotted in Figure 1.3, in particular the high fraction of luminous host galaxies.

We find both samples presented in Figure 6.7 clearly separated from the bulk of the field galaxy measurement, though the HES sample has at least the same characteristic luminosity (Figure 6.7a). Figure 6.7b reveals that the EMSS sample too has a great resemblance to the field galaxy LF: The brightest four datapoints lie well on a scaled version of the FGLF, only after that a turnoff is visible. This will at least in part be caused by the incompleteness of the sample.

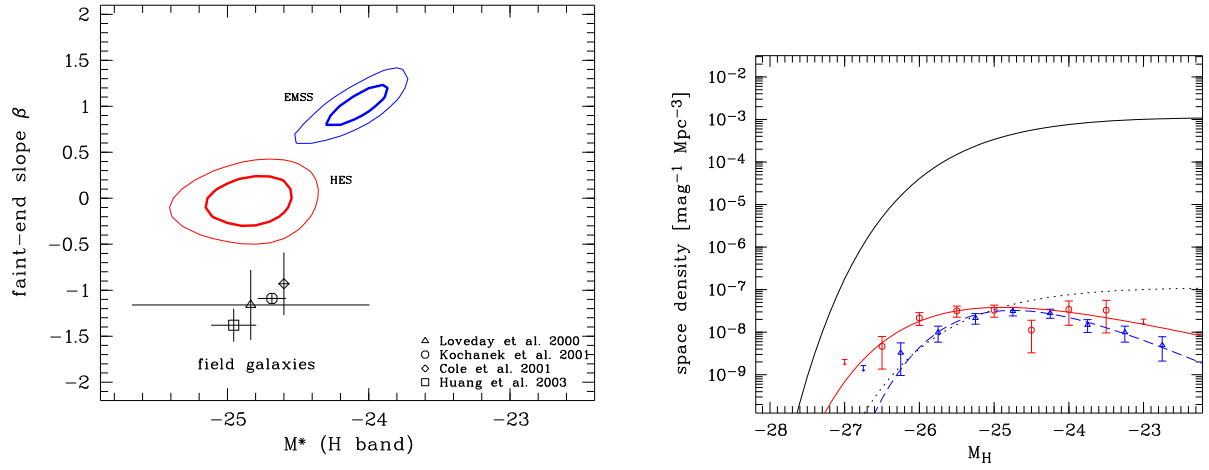

(a) Likelihood contours of the HGLF parameters

(b) HGLF and best fitting Schechter LF

Figure 6.7. Parameters and plots of the best-fitting HGLF of the total samples. Left: Likelihood contours of the HGLF parameters of both samples at 68% (bold) and 90% (thin) confidence levels. We also plot values with 2σ-errorbars for a number of field galaxy measurements. Right:Binned luminosity functions of the HES sample (circles) and the EMSS sample (triangles) with their best fit analytic functions. The upper full line is the field galaxy LF of Cole et al. (2001), the dotted is the same scaled to approximately fit the HGLFs.

There is – besides the different selection method – a second notable difference between the samples: A look at Figure 6.1 already reveals that the objects from the EMSS radiate at much lower Eddington rates than the HES objects. The same result was found by our fits. In the first run we let β, M^* and $m_{\rm cut}$ free and found that the HES objects radiate at maximal 13% $L_{\rm edd}$, while the EMSS have at max 1.46% $L_{\rm edd}$. This lower Eddington ratio is predicted by Kauffmann & Haehnelt (2000). For $z = 0$ and $M_B > -23$ they find $L/L_{\rm edd} = 0.03$. Their predicted Eddington ratios increase with both redshift and nuclear luminosity.

As we respected this maximal Eddington ratio in the fits, this does not have any influence on the other parameters. In particular we do not see fewer faint hosts because of the McLeod boundary.

The conclusion to draw is: We lack faint galaxies when comparing the HGLF to the FGLF. And we need to improve our model as for both samples KS tests reject the models ($P_{\rm KS} < 0.05$).

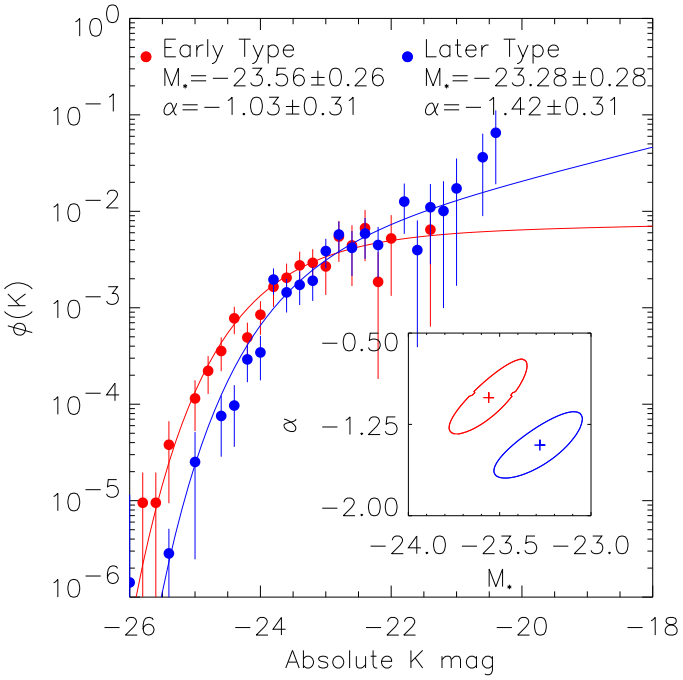

Figure 6.8. Binned LFs and best-fitting Schechter parametrisation of early- (red) and late-type (blue) galaxies along with 1σ likelihood contours of the parameters. While the one-dimensional errors overlap, the error ellipses do not, indicating a different distribution of the different galaxy types. Picture taken from Huang et al. (2003)

6.5.2.2 Dependence on host galaxy type

Trying to pinpoint the cause of the underfrequency of faint host galaxies, we want to investigate whether this is caused by a sub-population of the host galaxies. If we look at the GLF derived by Huang et al. (2003) from 224 galaxies with morphological information (Figure 6.8), we see that LFs do vary with morphological type. In formal agreement to these results are those by Kochanek et al. (2001) who had a sample of 4192 morphologically typed galaxies. There, the most prominent difference between early and late type GLFs is the different characteristic luminosity which for both samples is brighter by ≈ 0.8 magnitudes for the early galaxies (see also Figure 6.10).

Dividing our samples into early type galaxies (with bulge-to-total > 0.5) and late type galaxies increases our uncertainties, clearly seen in Figure 6.9 and 6.10: For both samples we find fewer early than late type galaxies (EMSS: 29 vs. 47; HES: 14 vs. 26) making errors larger for the early subsamples. Furthermore, in the HES sample we are left with only single objects in the galaxy luminosity bins fainter than -25.5. As those determine the faint-end slope, β is only poorly restricted.

Though the 1σ confidence limits overlap at least pair-wise for both samples, we note that early type galaxies are on average *fainter* than late type galaxies which is at odds with the field galaxy population. We also see that both subsamples have a high β and hence fewer faint galaxies. The high β of the combined samples can therefore not be attributed to e.g. a lack of faint ellipticals.

Numerical values and KS-probabilities are listed in Table 6.1 (model: 'simple', samples: 'early' and 'late'). Note that the acceptance of the models is again low, only the 'late' EMSS model is not rejected. But so far we have not adopted a dependency of the host galaxy luminosity on the nuclear luminosity other than the McLeod boundary.

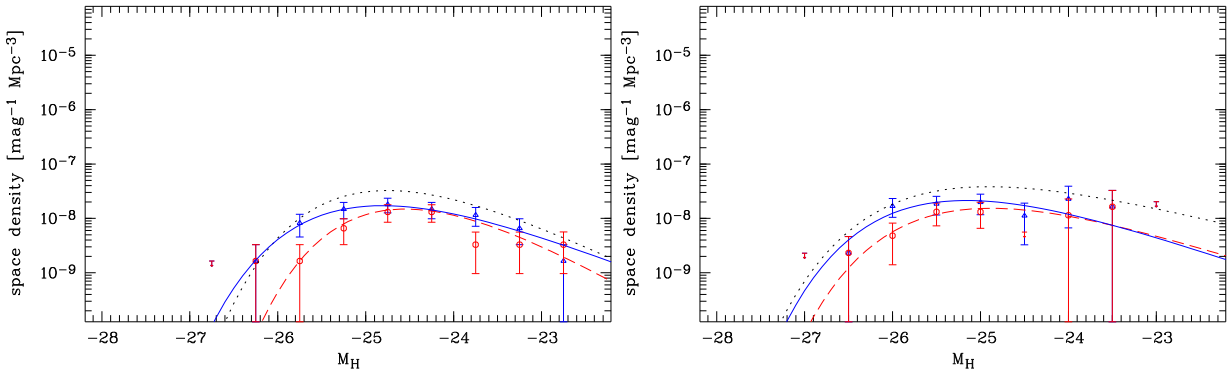

(a) EMSS sample

(b) HES sample

Figure 6.9. Binned luminosity functions of the EMSS and the HES samples, separated by galaxy type. Solid line and triangles are the analytical and binned LF of the late-type subsamples, dashed and circles of the early-type.

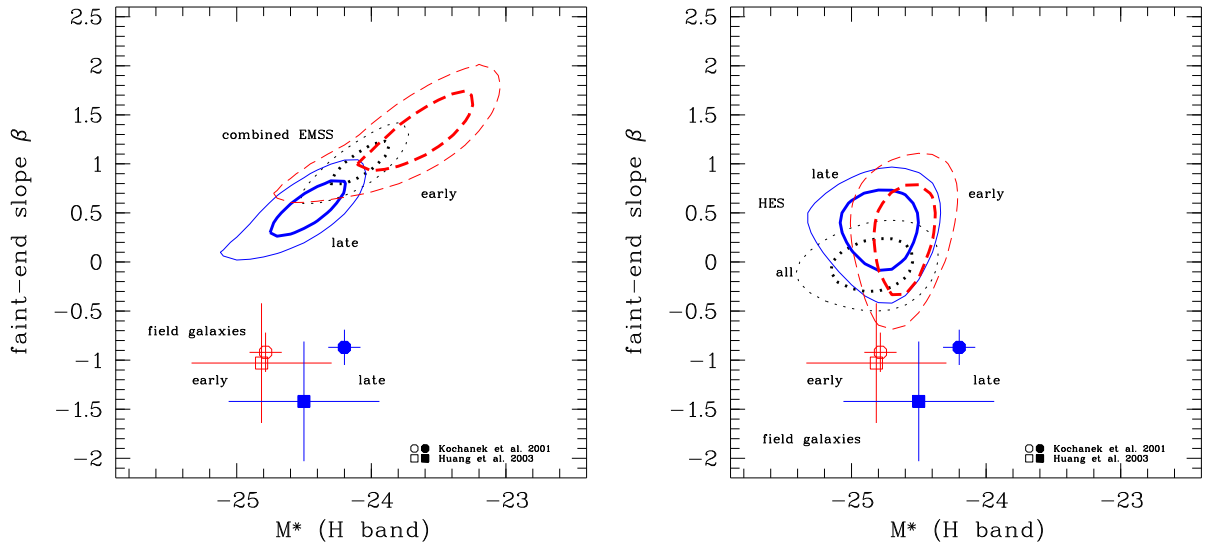

(a) EMSS sample

(b) HES sample

Figure 6.10. Likelihood contours of the HGLF parameters both samples at 68% (bold) and 90% (thin) confidence levels. Solid: late-type galaxies, dashed: early-type, dotted: combined sample.

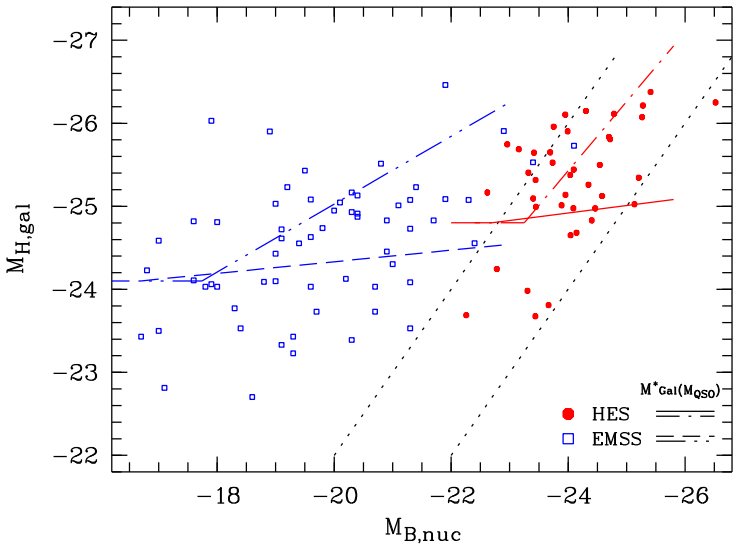

Figure 6.11. Dependence of the typical galaxy luminosity $M^*_{\rm gal}$ on nuclear luminosity. We find that $M^*_{\rm gal}$ gets brighter with brighter nucleus. This cannot be an effect of the McLeod boundaries (dotted), as this has been respected for the dashed (EMSS) and solid (HES) lines. Without this, the effect is much stronger (dash-dot-dot, dash-dot)

6.5.2.3 Variable GLF parameters

The true power of our formalism is the possibility to express dependencies between quasars and host galaxies. Most prominent is the McLeod boundary, but also other dependencies are conceivable. Two shall be investigated here.

The questions we want to investigate are: 'Is the host galaxy population which can host bright quasars *intrinsically* brighter than that of low-luminous AGN?' or 'are there just fewer faint galaxies picked for bright quasars?' yielding a change in the shape of the LF. Both is done with respect to the McLeod boundary: *We only fit the analytic LF to the data in the range which is allowed* ($L_{\rm nuc} < x\%^1 L_{\rm edd}$)

We code these dependencies as linear relations beyond a cut-off value $M_{\rm nuc,lim}$:

$$M^*_{\rm gal} = \begin{cases} M^*_{0,\rm gal} + m_\Pi \cdot (M_{\rm nuc} - M_{\rm nuc,lim}) & : \quad M_{\rm nuc} < M_{\rm nuc,lim} \\ M^*_{0,\rm gal} & : \quad M_{\rm nuc} \geq M_{\rm nuc,lim} \end{cases} \tag{6.15}$$

$$\beta = \begin{cases} \beta_0 + \beta_\Pi \cdot (M_{\rm nuc} - M_{\rm nuc,lim}) & : \quad M_{\rm nuc} < M_{\rm nuc,lim} \\ \beta_0 & : \quad M_{\rm nuc} \geq M_{\rm nuc,lim} \end{cases} \tag{6.16}$$

introducing the free parameters m_Π, β_Π and $M_{\rm nuc,lim}$. In order to stabilise the fit, other formerly free parameters are now fixed (β,$m_{\rm cut}$) to their previously determined values. $M_{\rm nuc,lim}$ was restricted to the range of observed $M_{\rm nuc}$. Beyond $M_{\rm nuc,lim}$ and $M^*_{\rm gal}$ are degenerate for $M_{\rm nuc,lim} > \max(M_{\rm nuc,i})$ and m_Π, β_Π are arbitrary for $M_{\rm nuc,lim} < \min(M_{\rm nuc,i})$.

For one model (m_Π II) the McLeod boundary was omitted, but the characteristic luminosity $M^*_{\rm gal}$ was kept variable. With this we want to test whether the McLeod boundary can be reproduced with a dependency of the intrinsic galaxy luminosity on the nuclear luminosity, or, as expected, is really cutting the bright part of an otherwise equally luminous population. In the 'm_Π I' model the McLeod boundary is included. For an equally luminous population we would expect m_Π to be close to zero.

[1] HES: 13%, EMSS: 1.5%

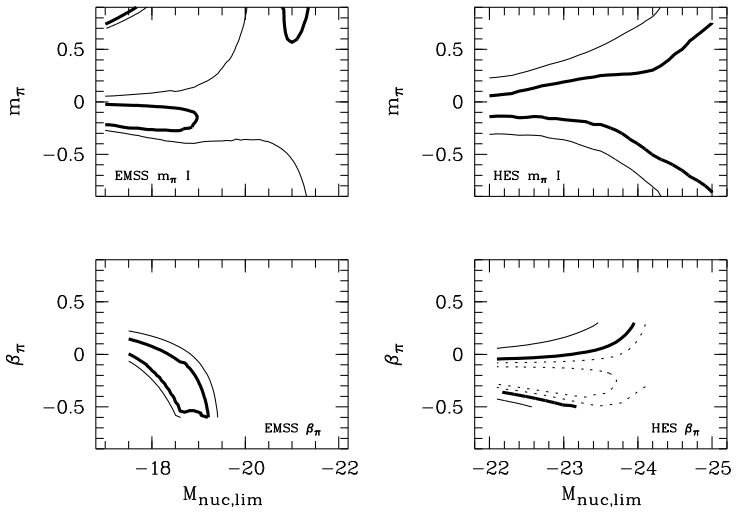

Figure 6.12. Likelihood contours of the HGLF parameters EMSS (left) and HES (right) samples for the 'β_Π' and 'm_Π I' models at 68% (bold) and 90% (thin) confidence levels. For the HES 'β_Π' we also plot 0.4 and 0.68 σ lines for orientation.

Figure 6.11 illustrates the parameters of the 'm_Π' models. The solid and dashed lines plot M^*_{gal} as a function of M_{nuc} for the model which included the McLeod boundary, while the dot-dashed and dot-dot-dashed lines represent the case without the boundary. For both samples in the latter case the slope is much stronger, trying to reproduce the cut-off. But an inspection of Figures 6.15 and 6.14 and Table 6.1 reveals that the case without boundary is very improbable. Even though M^*_{gal} varies strongly beyond $M_{nuc,lim}$, there are still too many objects modelled which do not fulfil the McLeod criterion. With the 'm_Π I' model things are different. In the both samples, the correction is close to zero and leads only to a small improvement, but is still rejected by the KS-test.

Uncertainties for these models are large and in particular include the 'simple' model (Figure 6.12). We conclude that there is only a weak, if at all, variability of M^*_{gal} with M_{nuc} and that the 'm_Π I' model probably not the best.

The last model computed ('β_Π') incorporates a dependence of the HGLF shape with nuclear luminosity by introducing β as a function of $M_{nuc,lim}$. A look at Figure 6.13a reveals that there indeed is a change of shapes, bright quasars seem to have a steeper faint-end than faint. Nothing can be seen for the HES sample, but the luminosity bins are much smaller here, as the HES samples spans only three magnitudes in nuclear luminosity while EMSS sample covers five magnitudes. This will lower the significance of any result for the HES sample, but otherwise sampling effects do not play a role as we operate on the unbinned data. The binning in Figure 6.13 is merely done for demonstrational purposes.

Computing the models we do find indications for a dependency of the slope on nuclear luminosities. The parameter for the faint-end slope β is rising with brighter M_{nuc}, i.e. bright quasars have a steeper drop in the faint end. Consequently, bright nuclei pick preferably bright host from the field galaxy population. Faint galaxies are underrepresented amongst bright nuclei, even if the nuclei radiate below 13% (EMSS: 1.5%) of the Eddington luminosity.

But how significant is this dependency?

The only models which are clearly non-rejected by a KS-test, as listed in Table 6.1, are the β_Π-models. A look at Figures 6.14 and 6.15 illustrates this. The simple models produce too many faint galaxies at faint nuclear luminosities and too few at high nuclear luminosities. 'm_Π I' models can correct this to some extent, but only for the β_Π models both distributions

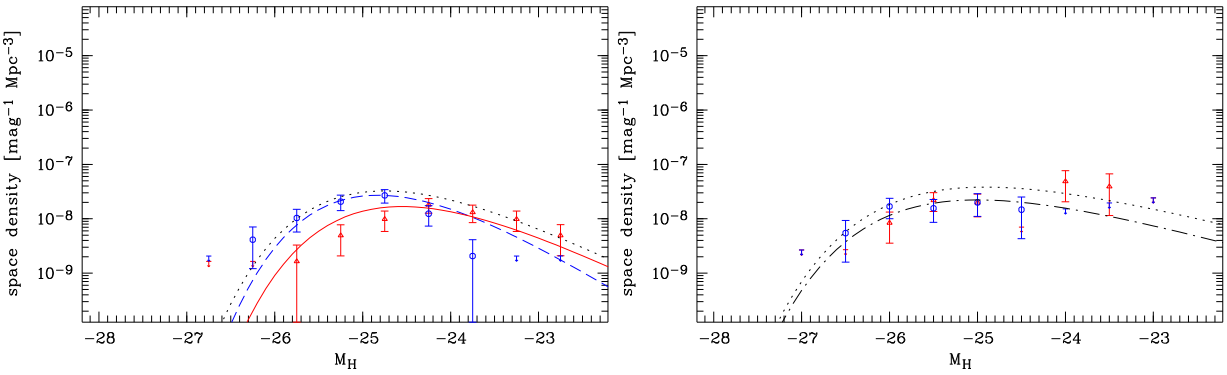

(a) EMSS sample

(b) HES sample

Figure 6.13. Binned luminosity functions of the EMSS and the HES samples, separated by nuclear luminosity. Samples are spilt in two approximately equally large subsamples at $M^B_{\rm nuc} = -24$ (HES) and $M^X_{\rm nuc} = -24$ (EMSS), circles having brighter nuclei than triangles. Dashed and solid lines are computed from the β_Π-model for average nuclear luminosities. As we see no difference in the HES subsamples, a single fit can be used (dash-dot). Dotted are the fits to the combined samples.

match. Clearly mismatching are the 'm_Π II' models in which the McLeod boundary is omitted. Note that in Figures 6.14 and 6.15 we always start with the same seed for the random number generator to allow direct comparison between the model distributions.

To compute confidence intervals for the obtained parameters, we fall back to the two-dimensional grid-search. We fixate M^*, as this is the most stable parameter, and only vary $M_{\rm nuc,lim}$ and m_Π resp. β_Π. The resulting confidence intervals have a complex structure (Figure 6.12).

We see that in all cases the 2σ contours reach the boundaries of $M_{\rm nuc,lim}$ which were selected to ensure that $M_{\rm nuc,min} < M_{\rm nuc,lim} < M_{\rm nuc,max}$. In the EMSS '$m_\Pi$ I' model we also see minima at $m_\Pi = 1$ which can be identified with the two extremes '$M^*_{\rm gal}$ is a linear function of $M_{\rm nuc}$' and '$M^*_{\rm gal}$ is constant'. The uncertainty in the HES in generally larger than the EMSS and the 'simple' model ($m_\Pi = \beta_\Pi = 0$) can not be excluded in any case, though the KS test suggests that the 'β_Π' models are the best approximations.

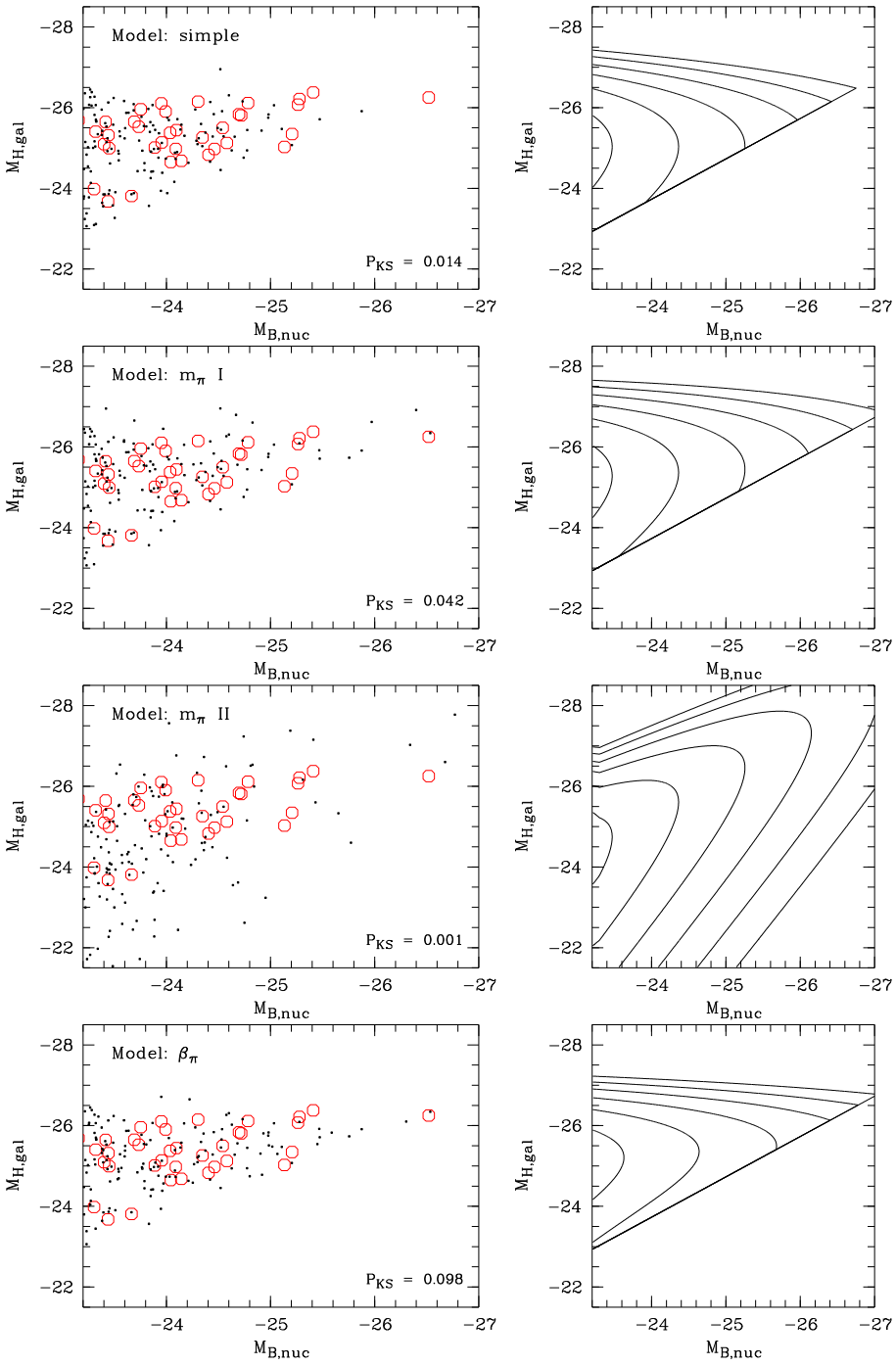

Figure 6.14. Models and measured quasar distributions and contourplots of corresponding QHGLF for the HES sample. Contourlines are spaced logarithmically at $10^{0.5}$ distance from a lowest value of 10^{-10} mag^{-2} Mpc^{-2}. Circles are datapoints, dots simulations. KS-values are computed from tenfold the datapoints. Here, we plot four modelpoints per datapoint. The models plotted are (top to bottom): Constant HGLF for all nuclear luminosities, M^* as a function of $M_{\rm nuc}$, ditto but without the McLeod boundary, slope β as a function of $M_{\rm nuc}$.

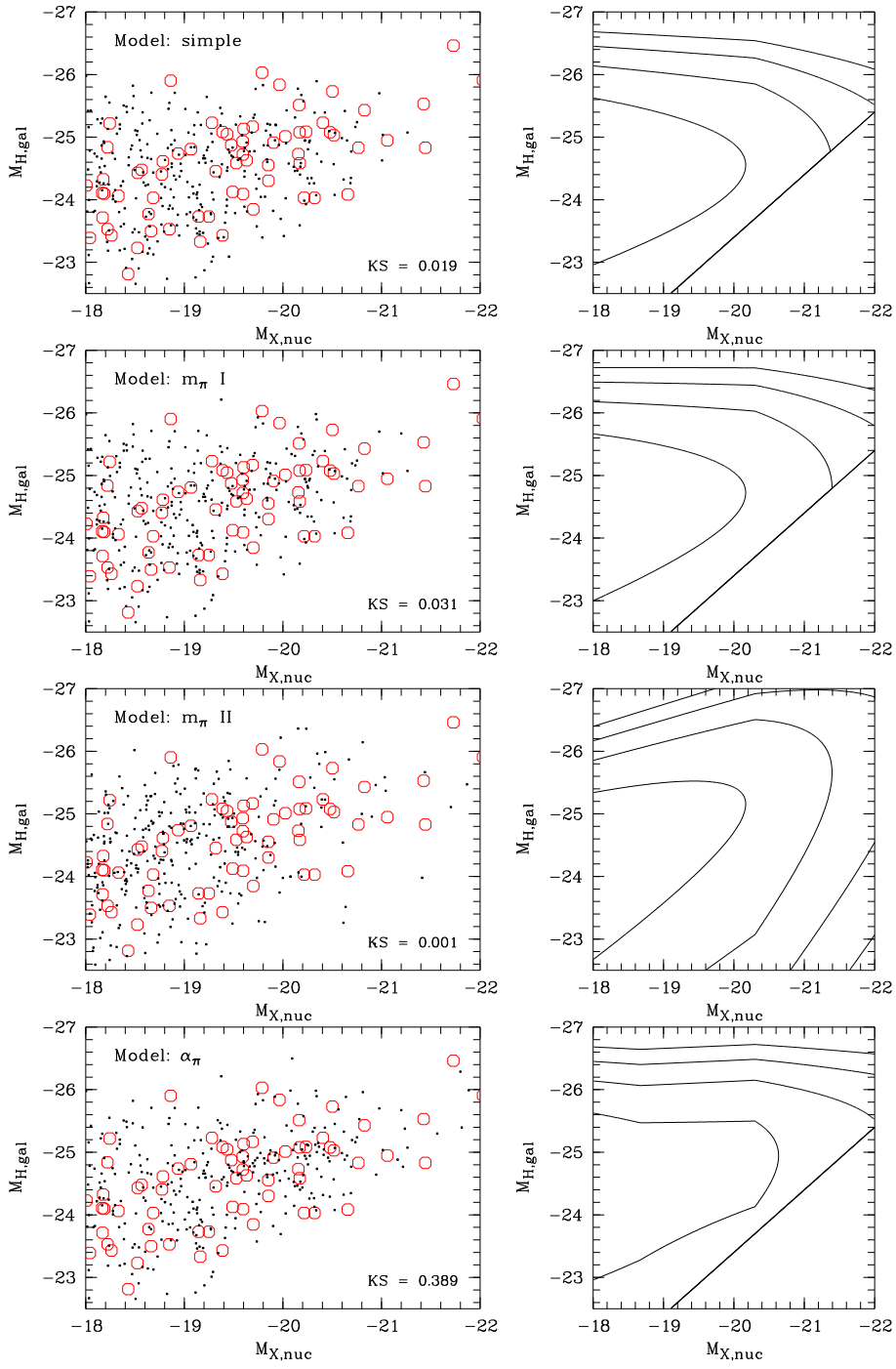

Figure 6.15. Models and measured quasar distributions and contourplots of corresponding QHGLF for the EMSS sample. Notation is as in Figure 6.14. The sharp edges occur at $M_{\rm nuc,lim}$ and $M^*_{\rm nuc}$ due to discontinuities in the functions.

6.6 Discussion

Before we discuss the results from the QHGLF estimation, we want to take a second look onto possible systematic errors and selections effects, as these can take strong influence on the statistics and final results.

During the decomposition process a possible systematic effect is an erroneous assignment of nuclear flux to the galaxy flux and vice versa. If there was a significant amount of light, in the order of one magnitude, misassinged from the nucleus to the galaxy for faint galaxies, a shape of the LF as seen would be expected. But while the uncertainties in the determination of $M_{\rm gal}$ for faint galaxies are of this order (see Figure 2.8) we see no bias. The same applies the EMSS sample as Schade et al. show. To flatten the LF, systematic errors in a large fraction of host galaxies in both sample are needed. As we don't see them, we can confidently exclude that they are responsible for the faint-end falloff.

For the HES the selection of the sample was thoroughly done. The HES is unbiased with respect to host galaxy luminosity and morphology until bright galaxies dominate over faint nuclei. But here, we see fewer quasars with faint host which are easier to detect in optical surveys. Furthermore the HES detects nuclei much fainter than the sample cut-off of $M_{B_J} < -18$ and so we do not expect boundary effects here. The HES sample itself contains *all* objects which fulfilled the criteria. The sample could however suffer from random losses. For the HES subsample we selected only luminous quasars. Luminous quasars reside mainly in luminous host galaxies. The number of faint host galaxies is therefore be small within the sample. An indication that our sample indeed missed a number of fainter galaxies is a void at $M_{\rm H,gal} \approx -24.5$, seen in both Figure 6.7b and 6.15.

The EMSS sample on the other hand is *not* complete. Schade et al. (2000) could not observe all selected objects and not all of the objects could be decomposed into nucleus and galaxy. The influence of the latter objects can be estimated by assuming that the relation between nuclear optical and X-ray luminosity (e.g. of Figure 5.3) holds. As X-ray luminosities are measured by the EMSS survey, optical, nuclear magnitudes can be computed with this relation. As Schade et al. measured total (nuclear plus host galaxy) for these objects, we can compute host galaxy magnitudes. In Figure 6.1b we did this for the ten missing objects, resulting in the EMSS_{76} sample. The missing objects are distributed along the central part of the LF and hence would further emphasise the steep gradients at both ends.

For the 18 objects which were not observed, we can esitmate that these were the objects with fainter nuclear flux using the number-magnitude relation of Figure 6.3a. The less luminous nuclei in the EMSS sample reside in host galaxies generally less luminous (see Figure 6.13) but only by a small amount. It it therefore reasonable to assume that the host galaxies of the missing objects are also distributed similiar to those in the EMSS sample. But if we assume that all missing host galaxies are faint – which is unlikely – we can maximize the faint-end slope β. The resulting HGLF is then *still* falling toward fainter galaxies and still not compatible to the FGLF.

Random losses can also play a role in the EMSS sample. In Figure 6.11 it can be seen that within the EMSS no host galaxies fainter than $M_{\rm H,gal} \approx -23$ are found. As we do not expect to find a sharp boundary, the sample must also be incomplete in the bins just brighter than -23. Where the incompletenes becomes significant can only be determined with a thorough analysis of the survey selection criteria, which is beyond the scope of this work.

In order to estimate where the samples reach completeness, we want to assume that the parent

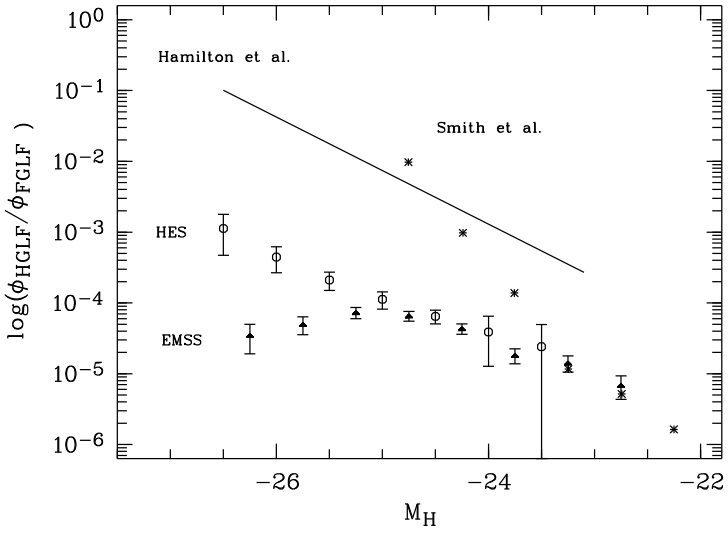

Figure 6.16. Ratio of quasar host galaxies and field galaxies. Data are from Hamilton et al. (2002) (solid line), Smith et al. (1986) (astersiks), the HES (circles) and EMSS (triangles) samples.

population of quasar host galaxies is the entire field galaxy population, which is not unreasonable, as in almost all nearby galaxies, a central massive dark object can be found (Magorrian et al. 1998), one essential prerequite for a quasar. The fraction of field and quasar host galaxies should then rise with rising galaxy luminosity and level when the quasar sample is complete.

In Figure 6.16 we have plotted this 'activity fraction' f_0 with respect to the FGLF by Cole et al. (2001) for four different samples. Out of these, only the EMSS sample levels at $f_0 \approx 5 \cdot 10^{-5}$. The HES has an activity fraction which scales roughly linear with host galaxy luminosity: $\log f_0 \approx -0.58\, M_{\rm gal} - 18.2$. The other two samples both suffer from incomplete samples. Hamilton et al. (2002) tried to correct this with a complicated scheme, but introduced extra systematic errors during the normalization (see Section 6.5.2.1). In particular their claim that all bright galaxies host a quasar, cannot be confirmed by us.

From the activity fraction we can compute the average time a quasar is turned on using the 'ensemble average = time average' argument. As we have respected quasar evolution by incorporating an evalution model in the computation of the LF, the activity fraction is valid for $z = 0$. The PDE model translates to an activity fraction which depends on redshift : $f(z) = f_0(1+z)^{6.5}$. To compute the dutycycle $t_{\rm accr}$, we need to average the activity fraction over the redshift interval of the observations and multiply with the maximum lookback time.

$$t_{\rm accr}(M_{\rm gal}) = t_{\rm lookback}(z_{\rm max})\, f_0(M_{\rm gal}) \int_0^{z_{\rm max}} (1+z)^{6.5}\, {\rm d}z \frac{2}{z_{\rm max}} \tag{6.17}$$

$$\begin{aligned} &= 4.7\,{\rm Gyr} \cdot 6.4 \cdot f_0(M_{\rm gal}) \\ &= 3.4\,{\rm Myr} \cdot 10^{-0.58(M_{\rm gal} - M^*_{\rm gal})} \\ &= 3.4\,{\rm Myr} \cdot \left(\frac{L_{\rm gal}}{L^*_{\rm gal}}\right)^{1.44} \end{aligned} \tag{6.18}$$

with $M^*_{\rm gal} = -24.8$. Note that this implies that *all* field galaxies brighter than $M_{\rm H,gal} = -23$ in $z < 0.3$ develop nuclear activity making $t_{\rm accr}$ a lower limit. In these equations we let f be a function of $M_{\rm H,gal}$ as determined for the HES sample.

This relation is not completely unexpected as $t_{\rm accr}$ is proportional to the amount of available cold gas $\mathcal{M}_{\rm gas}$ (Cattaneo 2001). We do not want to speculate on the size of the exponent in (6.18) since gas-to-total mass ratios vary strongly at low redshifts. The fact that the exponent is greater than one however suggests that the mass-to-light ratio scales with galaxy size which is somewhat at odds with recent findings (e.g. Graham 2002), but our uncertainties are high and the range of valid HGLFs within the 2σ boundaries allow exponents between 0.9 and 1.8. Also without a complete sample with larger size and luminosity range, we cannot exclude random losses of faint galaxies a source for this relation.

Is we assume a universally valid activity fraction, we expect this to be between the level of the EMSS ($f_0 \approx 5 \cdot 10^{-5}$) and the highest values found by the HES ($f_0 \approx 1 \cdot 10^{-3}$), as we argued that both samples are complete at the bright end of the LF. From this it follows that the quasar duty cyle is 2 Myr $\lesssim t_{\rm accr} \lesssim$ 40 Myr. A duty-cycle of this order of magnitude can also be estimated from the mass accretion rate and the mass of the central black hole. Doing such Beckert & Duschl (2002) estimate an upper limit for duty-cycle of some 10^7 yrs for a nucleus radiating at Eddington limit in accordance with our result.

6.7 Conclusions

For the first time we were able to compute a bivariate host galaxy luminosity function which can handle mutual influence between active nucleus and host galaxy. We have found that the HGLF is not simply a scaled field galaxy LF, but has a drop-off at the faint end. Whether this is intrinsic or caused by random lossen of faint host galaxies could not be decided. Larger samples covering a wider range of host galaxy luminosities are needed.

By assuming that the entire field galaxy population, except the irregular galaxies, is the parent population of quasar host galaxies we were able to estimate a solid lower limit for the quasar duty-cycle. We found this to be 2 Myr $\lesssim t_{\rm accr} \lesssim$ 40 Myr.

Many other applications of the bivariate HGLF are conceivable. One of the most interesting is the evolution of the HGLF, by introducing redshift-dependent parameters (e.g. $M^*_{\rm gal}(z)$) and compare this to the evolution of field galaxies.

7 High-redshift quasar hosts with adaptive optics

7.1 Introduction

The study of high-redshift quasar host galaxies has during the past few years become quite an active research field, offering new roads of insight both on the phenomenon of quasar evolution as well as galaxy formation in the early universe. The strong cosmic evolution seen in the quasar population from the peak at $z \sim 2-3$ is very likely an effect of changing environmental conditions. Together with the evolution in the star formation rate from $z \sim 2$ to present-day this implies a strong link between the formation and subsequent evolution of galaxies and the processes that trigger and maintain the quasar activity (e.g. Franceschini et al. 1999). This is reflected in the correlation between black hole mass and host spheroid luminosity found for local massive ellipticals (Magorrian et al. 1998; Kormendy & Gebhardt 2002), recently shown to hold for quasars (Laor 1998; McLure & Dunlop 2002). Observations of host galaxies over a range of redshifts are necessary to set limits on the fuelling efficiency of quasars and the masses of their central black holes at different epochs.

Since nearly all present-day stellar spheroids house a massive black hole, it is not unreasonable to expect that most bright galaxies were active at some point during their history. In addition, host galaxies form a subset of the galaxy population which is selected without any dependence on spectral shape (i.e. stellar populations) or the presence of emission lines (i.e. star formation rate). This subset is not necessarily a random sample of field galaxies but at least has different selection biases than those normally found in galaxy surveys. Thus, determining the characteristics of high-redshift hosts will broaden the picture on the properties of early galaxies and how they formed. Together with lower-redshift data the significant evolution of the properties of the hosts in terms of star formation and stellar populations will be uncovered.

Ground-based and HST studies have established the result that host galaxies of luminous quasars at low to intermediate redshifts predominantly have spheroidal morphologies and luminosities $\geq L^*$ (e.g. Taylor et al. 1996; Kotilainen et al. 1998; Bahcall et al. 1997; Boyce et al. 1998; McLure et al. 1999; McLeod & McLeod 2001). The properties of host galaxies at higher redshifts have been harder to determine, owing to the difficulty of detection. Results from investigations utilising ordinary subtraction of the point spread function (PSF) as well as two-dimensional modelling show objects brighter than low-redshift hosts by $2-3$ magnitudes (Heckman et al. 1991; Lehnert et al. 1992, 1999; Aretxaga et al. 1995, 1998) and a widening difference in luminosity between the hosts of radio-loud and radio-quiet quasars, where those inhabited by radio-loud quasars have become about a factor of three brighter at redshift $\simeq 2$ (Dunlop et al. 2003; Falomo et al. 2001). These objects have luminosities exceeding several times L^*, whereas the radio-quiet hosts only reach $\simeq L^*$ (Hutchings 1995; Kukula et al. 2001; Ridgway et al. 2001). However, exceptions can be found, as shown by the detection by Aretxaga et al. (1998) with adaptive optics of a high-redshift radio-quiet host as bright as those of the most luminous radio-loud quasars, supported by Hutchings et al. (2002) similar result from HST data for two radio-quiet quasars. On the other hand, Lowenthal et al. (1995) failed to resolve the radio-quiet hosts in their $z \simeq 2.5$ sample. The high-redshift objects detected to date are more compact than their low and intermediate redshift counterparts, having scale lengths of only $3-5$ kpc as compared to the ~ 10 kpc of less distant hosts (Falomo et al. 2001; Ridgway et al. 2001;

Aretxaga et al. 1998).

The technique of adaptive optics (AO) has been used with increasing success for imaging of galactic objects like protoplanetary disks and binary star systems. So far, though, few have tried to use AO for quasar host galaxy studies, even though this is a discipline which benefits from high spatial resolution in combination with the great light-gathering power of ground-based telescopes. One reason for such studies being scarce is surely that the method's fundamental advantage of producing diffraction-limited images with large telescopes is paired with new challenges in correctly differentiating between the compact nucleus and the extended host galaxy, considering the constantly changing point spread function (PSF).

Previous investigations of host galaxies with AO have all been carried out in the near-infrared, where the contrast between host and quasar light is largest. Atmospheric turbulence also has less influence on longer wavelengths for a given AO correction, permitting the use of fainter guide stars and providing a larger isoplanatic patch in the near-infrared. The focus of the earlier work has either been on low to intermediate redshifts, where the host galaxies are resolved and the determination of the PSF is not crucial to the detection of the objects (Stockton et al. 1998; Márquez et al. 2001), or probed higher redshifts (Hutchings et al. 1998, 1999, 2001; Aretxaga et al. 1998). In general, outright removal of the nuclear contribution was refrained from, instead concentrating the efforts on investigating substructures in the host galaxies. For studies of low-redshift quasar hosts AO shows an improvement over traditional imaging in the resolution of clumps and companions, but apart from that the results obtained are rather similar to studies made using standard observational techniques.

The true power of AO appears in the analysis of high-redshift quasars. Because of the very compact appearance even of giant elliptical galaxies at $z > 1$, the most important factor for a successful study in the presence of a PSF shaped active nucleus is a PSF as narrow as possible. Here the superb image quality of AO systems with very narrow PSFs enables – potentially – a much better distinction between nucleus and extended host than uncorrected, seeing-limited imaging.

In Section 7.2 we describe the object selection strategy, observations and reductions. Section 7.3 outlines the fundamentals of our analytical tool, and in Section 7.4 this tool is applied to our sample. The results are discussed in Section 7.5.

7.2 Targets

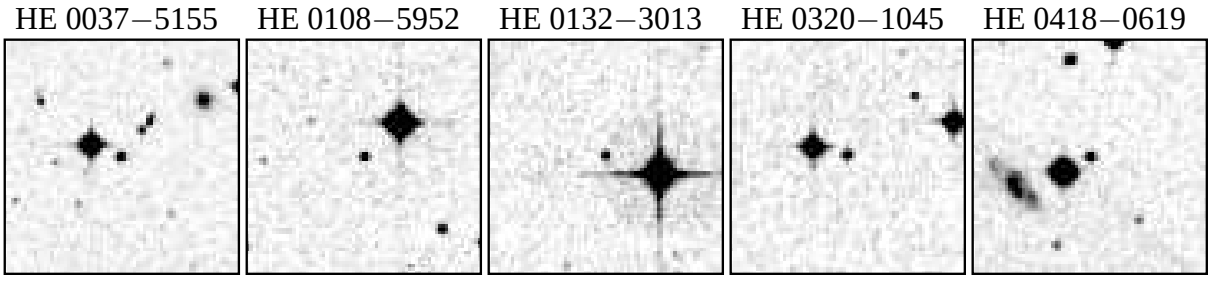

Figure 7.1. $2' \times 2'$ DSS images around the five featured quasars (the central object in each panel), together with their corresponding AO guide stars. North is up, East is to the left.

Table 7.1. Basic properties of the input target sample and the corresponding adaptive optics guide stars.

Object name	R.A. (J2000.0)	Dec	z	B_J	Guide star	dist.	$V_\star$
HE 0037−5155	$00^h\,40^m\,17\overset{s}{.}1$	$-51^\circ\,38'\,49''$	2.127	17.7	0803000529	$16\overset{''}{.}8$	12.9
HE 0108−5952	$01^h\,10^m\,52\overset{s}{.}0$	$-59^\circ\,36'\,21''$	1.971	18.9	0847901239	$25\overset{''}{.}2$	12.0
HE 0132−3013	$01^h\,34^m\,33\overset{s}{.}8$	$-29^\circ\,58'\,15''$	2.229	18.0	0642801994	$28\overset{''}{.}8$	11.0
HE 0320−1045	$03^h\,22^m\,24\overset{s}{.}5$	$-10^\circ\,35'\,12''$	2.282	17.0	0529800301	$18\overset{''}{.}0$	13.0
HE 0418−0619	$04^h\,21^m\,24\overset{s}{.}2$	$-06^\circ\,12'\,04''$	2.010	19.0	0473301854	$15\overset{''}{.}6$	11.9

7.2.1 Target selection

The number of high-redshift quasars bright enough to allow on-axis adaptive wavefront correction is extremely small, basically zero for the more venerable AO systems such as ADONIS on the ESO 3.6 m telescope used by us (see below). In line with other researchers, we have therefore searched for targets with a nearby bright star that can be used for wavefront sensing. For ADONIS, the uttermost limits for meaningful AO imaging in the K band are: a red (R or I) stellar magnitude $\lesssim 13$, and a distance between quasar and star of $\lesssim 30''$; to be practical, these two criteria should not be carried to their extremes together. Even then, the low surface densities of both agents involved make the number of such targets necessarily small in any survey. Other groups before us have already used the available quasar catalogues to identify possible targets, and at the time of preparing our observations in 1999, these catalogues seemed to be more or less exhausted, at least to the limits of systems such as ADONIS.

We therefore performed a new search using a largely unexplored database. The HES survey (Wisotzki et al. 2000) contains several thousand bright quasars and quasar candidates at all redshifts up to $z \simeq 3.2$, and the survey magnitude limit of $B_J \lesssim 18$ (on average) makes it a rich source of high-luminosity quasars. We went through the full database, selecting all quasars with redshifts $z \gtrsim 1.8$, and included also quasar candidates where a tentative redshift had been assigned based on their digitised objective prism spectra (for details, see Wisotzki et al. 1996, 2000). We then paired the list with the *HST Guide Star Catalogue* (GSC) and searched for pairs matching the above given criteria for possible ADONIS guide stars. Since for the stellar magnitudes we had only blue B_J, the limit was set to $B_J < 14$. Altogether, we arrived at 12 candidate targets selected by these criteria. Of these, seven objects strained both the magnitude and the distance limits to an unacceptable degree and were eliminated from the list. We were then left with five remaining targets that we eventually took to the telescope. Table 7.1 contains their basic properties, including those of the adopted AO guide star. Given that the quasars are drawn from an objective prism survey, no radio flux measurements of the sources exist. Figure 7.1 shows little 'postage stamp' images of the quasars together with their nearby AO guide stars.

7.2.2 PSF calibrators

One of the fundamental drawbacks of adaptive optics observations is the difficulty to establish knowledge about the PSF. On the one hand, the need for high pixel sampling necessarily limits the field of view to not much more than a few arcseconds around any given target. On the other hand, even within the formally defined isoplanatic patch the PSF varies strongly over the field,

basically showing a decreasing Strehl ratio with increasing off-axis distance. While this might be a mere dirt effect in applications such as resolving binaries or searching for faint point-like companions, a good quantitative understanding of the PSF is essential for the study of quasar hosts.

In our case with an ADONIS field of view of only $12\farcs8 \times 12\farcs8$, the quasars were practically always totally isolated. We thus needed to obtain our PSF from external stellar calibrators, to be observed non-simultaneously with the quasars. We decided that this task was so critical that we needed two PSF calibrators for each quasar, to enable cross-validation. Each of these PSF calibrator stars needed to have one wavefront sensing guide star of magnitude and distance as closely matching to that of the quasar as possible. The PSF stars themselves were chosen to be substantially brighter than the quasars, typically around $B_J \simeq 14-15$, allowing for a high S/N PSF definition with short exposure times. Following these criteria, we selected several stellar pairs from a $\sim 5^\circ$ surrounding of each quasar.

7.2.3 Observations

Observations were performed in short *K* band on the nights of 1999 November 27-29, using the ADONIS system on the ESO La Silla 3.6m telescope. The SHARPII+ camera was equipped with a 256×256 Nicmos III array with a pixel scale of 40 μm. The resolution was set to 50 milliarcsec/pixel resulting in a field of view of $12\farcs8 \times 12\farcs8$.

During the course of the first night it was found that all selected PSF stars for the object HE 0418–0619 were too faint in *K*. Since quick reduction and analysis performed on-site also indicated the possible detection of host galaxies for the objects HE 0037–5155 and HE 0132–3013 while the weather conditions became less favourable, the observing strategy was changed to concentrate only on the three brightest objects.

For every target the quasar itself was first observed in a cycle of 10×60 or 15×60 seconds, followed by the corresponding two PSF stars in a cycle of 3×60 seconds each. Standard stars were obtained at the beginning and end of each night, and evening skyflats acquired. The seeing as computed from the wavefront sensing data by the performance estimator software was stable at $\simeq 0\farcs6$ during the first night, but varied between $0\farcs7-1\farcs1$ and $0\farcs8-1\farcs2$ respectively during the following two nights.

Imaging in the *K* band is limited by the thermal emission background radiation, which suffers from temporal as well as spatial variations and has to be monitored constantly for an adequate background removal. As our objects are only marginally extended and embedded in fields only sparsely populated by stars, we switched the quasar position by not more than $\sim 8\farcs$*w*hen using the chopping mirror, thus including the object also in the off-target sky-acquisition frames but in the opposite quadrant (see Figure 7.2). Since the chopping can be done without leaving the AO optimisation loop the target integration times were doubled in this way, with sky estimates still received. Total integration times thus amount to 160 minutes for HE 0037–5155, 170 minutes for HE 0132–3013 and 230 minutes for HE 0320–1045, while the PSF stars with brightnesses of $K \approx 15.4-13.2$ magnitudes were integrated for typically 36 minutes.

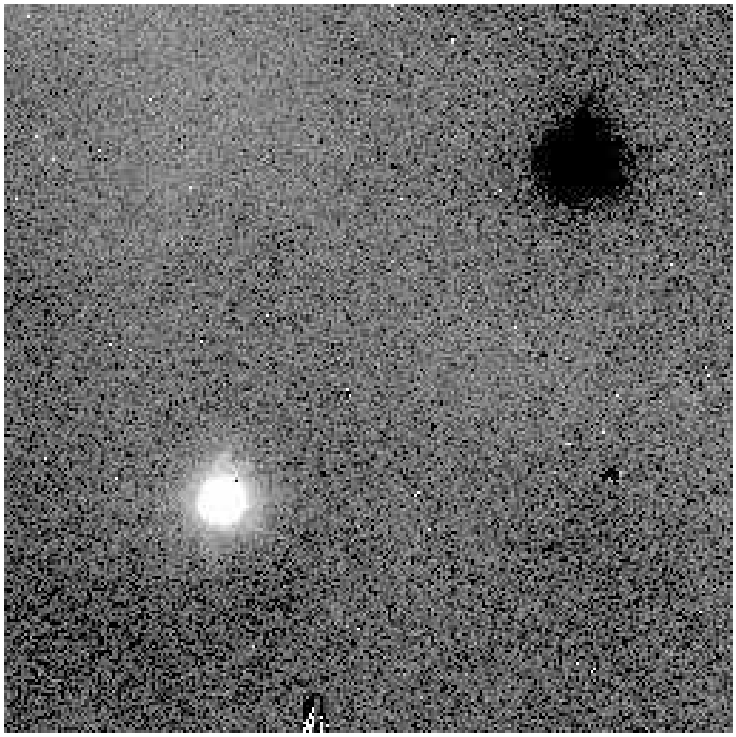

Figure 7.2. Example of a background corrected image from an image cube of HE 0037–5155. The on-target quasar observation is located in the lower left corner, and in the opposite corner a residual remains of the quasar in its off-target frame position (see the reduction process described in the text).

7.2.4 Reduction

When estimating the background the on- and off-target frame sets of each image cube were combined separately. After making a global background correction to zero median value, the frames were averaged. Next, the averaged on-target frame was subtracted from all individual off-target frames and vice versa. Since the averaged frame contains the quasar image, the subtraction creates a negative imprint of the quasar in the opposite quadrant in all individual frames. This poses no problem because only the data in the object's quadrant is needed (Figure 7.2). Defining the background for a given frame with information from the data cube itself guaranteed using the temporally closest background estimate, thus well accounting for the temporal variations. In this way most of the background pattern could be removed.

After subtraction of the background frame some lower level residual structures remain, created by different thermal emission patterns from the two positions of the chopping mirror (see Eisenhauer 1997). Since only the small detector area covered by the quasar's light distribution is needed for analysis, we assumed the background to be locally constant. This local background was adjusted to a level where the radial growth curve of the quasar became constant between $1\overset{''}{.}a$ and $1\overset{''}{.}5$ radius. Some object flux ($\lesssim 1\%$) is still present inside this range, but beyond it the sky shows local non-corrigible bumpiness containing a number of counts comparable to the local object flux. As a consequence the sky background value is systematically overestimated, but tests show that this leads to an average underestimation of the magnitudes of the extended emission by only 0.06 mag.

For all reduced frames we created bad pixel maps from skyflats using the 'flat' task from the ECLIPSE data reduction package (Devillard 2001). It was found that bad pixel areas changed in size within image cubes, so the global bad pixel map was therefore complemented with individual maps for each frame where also cosmics were marked. The remanence effect common for

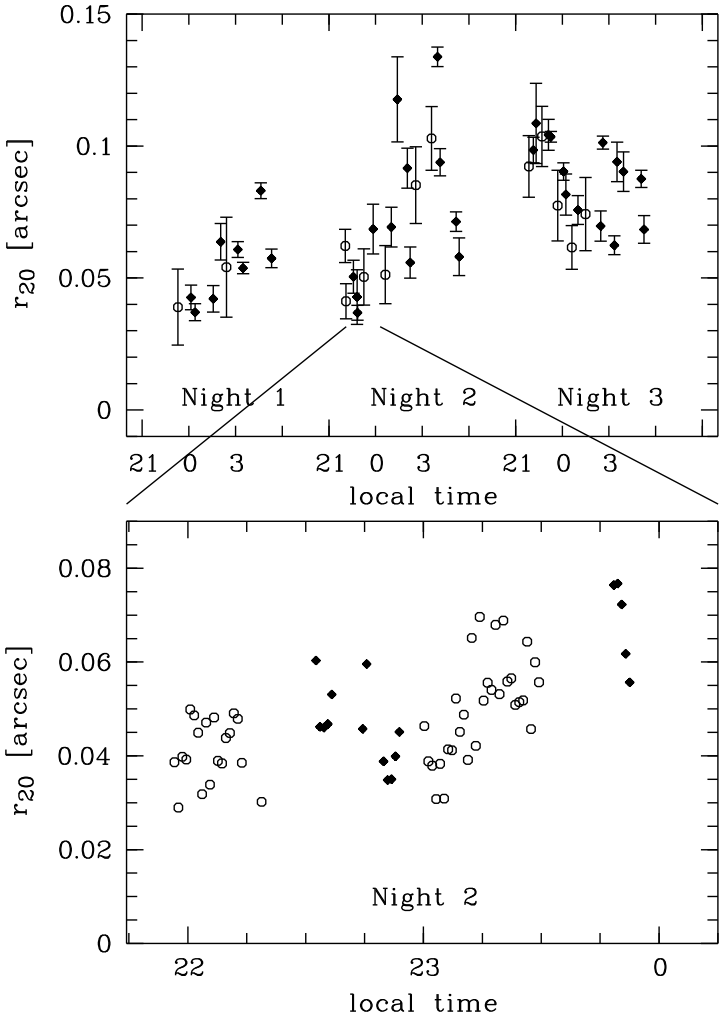

Figure 7.3. Progression of core width with time. In the top panel we plot average values and 1σ errorbars for each image cube for both PSF calibrator stars (filled diamonds) and quasar observations (circles). We expand the beginning of the second night in the lower panel, plotting values for every image of the first five cubes. The variation between two consecutive images can be as large as 30 %.

Nicmos III arrays (which alters the sensitivity of pixels over- or underexposed in the previous frame) was found to be negligible for both quasar and PSF star images. The images were flat-fielded using skyflats taken in the beginning of each night and computed with the 'flat' task, and calibration was performed by aperture photometry on the standard stars. The uncertainty of the calibration is 0.05 magnitudes. Finally, a cut-out image of the quadrant containing the quasar was made.

The reduction procedure outlined above was applied in its entirety to the PSF stars to guarantee an identical treatment. During the course of reduction we found that some single images or whole image cubes (of both quasars and stars) showed problems of the AO optimisation loop or the guiding. These had to be excluded from subsequent analysis.

7.3 Analytical tool development

The goal of an analysis tool in the given context is to discriminate between point sources and extended sources and to quantify the amount of extended emission. This has to be done in the light of a variable PSF shape, which changes with the ambient conditions and the level of adaptive optics correction.

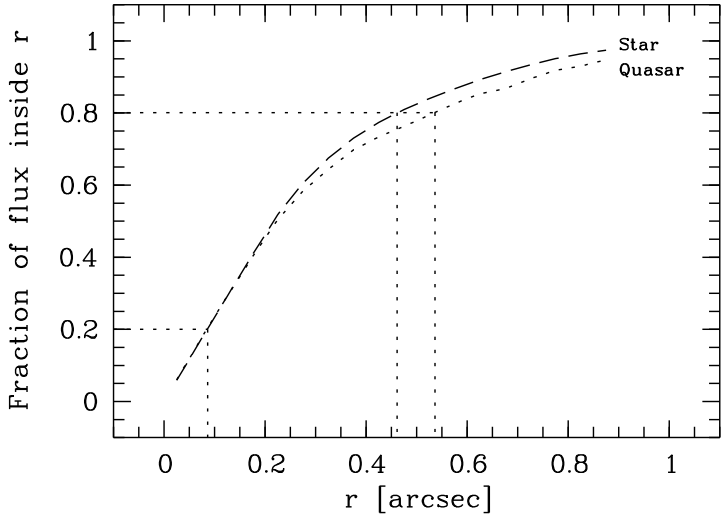

Figure 7.4. Growth curves for a star (dashed line) and a quasar (dotted line), taken from the first cubes of the second night (lower panel in Figure 7.3). The determination of r_{20} and r_{80} radii allows a distinction between the two types.

To monitor this temporal variability the observations of PSF-calibrator stars and quasars were nested. Unfortunately, we found the PSF to be variable even within one image cube. Figure 7.3 illustrates this on time-scales of nights (upper panel) and minutes (lower panel). The adopted quality indicator is r_{20}, the radius encircling 20 % of the total flux, which for stars and high-redshift quasars is closely related to the Strehl ratio. The conditions shown in Figure 7.3 are typical of our observations as we find both the r_{50} (FWHM) and the two-dimensional isophotal shape of the PSF to be variable on short time-scales.

The reason for the variability of the PSF is the rapid change of the atmospheric turbulence characteristics, inducing different responses from the AO system. This in turn is leading to variation in the centroid, higher FWHM, lower Strehl ratios and higher speckle noise. An increase in integration time would in general reduce this variation but will at the same time decrease resolution and hence the benefits of AO observation (for further insights see Le Mignant et al. 1998). In the *K* band exposure times are in any case limited by the strong sky background emission in order to avoid non-linearity or saturation effects. Since the changing shape even extends to PSF star images displaying similar Strehl values, thus suggesting very similar correction quality of the AO system, we have to conclude that the PSF in the quasar image is essentially unknown.

This poses a serious problem. For all methods of PSF subtraction and deconvolution commonly used in optical and near-infrared imaging of quasar hosts, a precise knowledge of the PSF is crucial for all cases of compact host galaxies. Thus these methods can only be applied to AO data when the hosts are very extended and the knowledge of the exact shape of the PSF is less important. This is the case i.e. for low-*z* objects, when structures outside of the centre are to be resolved, but not for high-*z* quasars. It is clear that another approach is needed to evaluate whether the quasars observed by us are extended or not, and to determine the characteristics of the possible host galaxies.

While the PSF variation in general is non-predictable, we found that a well-defined relation exists for the stars between the width of the core and the width of the wings, as measured by the radii including 20% and 80% of the flux. We chose these values since we here expect the greatest contrast between stars and quasars at reasonable pixel and background noise respectively. In the core stars and quasars are dominated by the PSF and its varying width, but at larger radii the host galaxy contributes flux, thus flattening the curve of growth. This situation is shown in Figure 7.4.

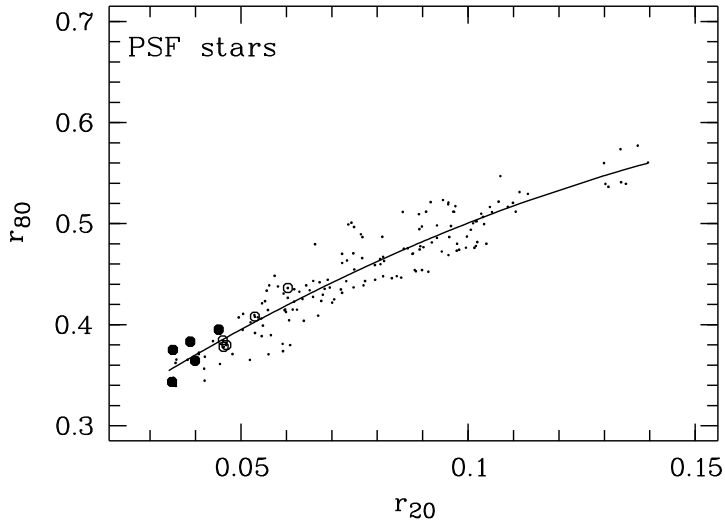

Figure 7.5. The r_{20}-r_{80} diagram for the PSF stars. The radii are in arcseconds, and each point corresponds to a single image from an image cube. The solid line is the best fit to the PSF star points, named by us "PSF-line". Filled and empty circles mark two stellar data cubes taken just after 23 hrs on the second night (see Figure 7.3).

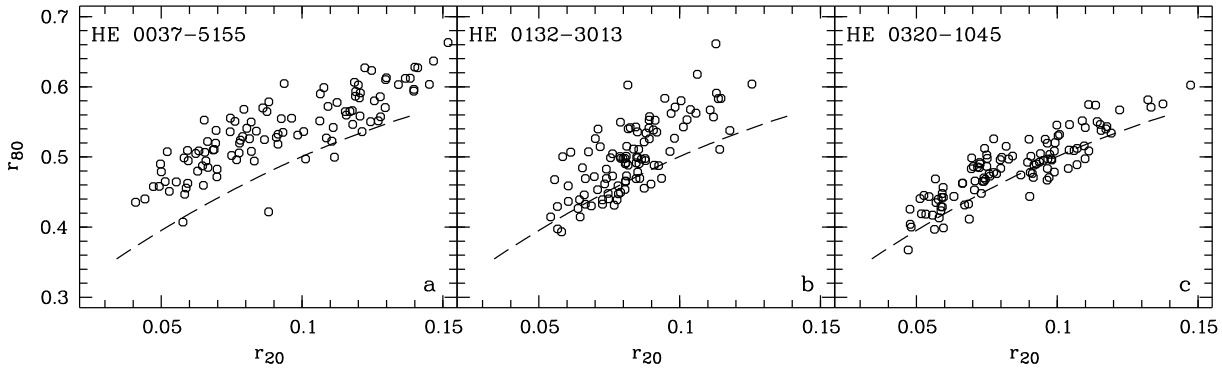

Figure 7.6. The r_{20}-r_{80} diagrams for the quasars. The radii are in arcseconds, and each point corresponds to a single image from an image cube. The dashed line is the reproduced "PSF-line".

For the PSF stars plotted in Figure 7.5 we parameterise the variation of r_{80} with r_{20} using a polynomial fit to obtain what we will call the "PSF-line", which marks the track in the diagram along which all point sources without extended flux are distributed. The particular shape of the PSF-line is created by all atmospheric and instrumental variability combined, and the individual PSF stars scatter around this relation due to photon shot noise and varying two-dimensional asymmetries in the PSF shape. The r_{20} and r_{80} parameters are mainly dependent on seeing but also on the general ambient conditions, though any PSF shape variation will be hidden in the noise around the PSF-line.

In Figure 7.6 the r_{80} values are plotted against r_{20} as determined for all individual quasar images, using the data obtained during the three nights of observation. We show parameters for all three quasars respectively (7.6 a–c), where it can be seen that the objects each fall into distinct areas of the r_{20}–r_{80} diagram. In Figure 7.6 the PSF-line has been superimposed on the parameters measured for the three quasars. The regions occupied by these objects are in general systematically shifted away from the PSF-line, in two cases by quite a large distance. The different amount of scatter between the PSF stars in Figure 7.5 and the quasars in Figure 7.6 is due to their different brightnesses, since the stars are typically ten times brighter than the

quasars. Thus the scatter induced by S/N limitations is less for the observed stars.

The shift of the quasars away from the PSF-line in these diagrams is immediately suggestive of influence from a host galaxy, but in order to quantitatively confirm a detection, we need a better understanding of the principles which create the distribution of points in the diagram. To this end we will in the following attempt to reconstruct the distribution of quasar points using our knowledge about the distribution of PSF star points under the hypothesis that the presence of a host galaxy is responsible for the observed shift. This is done in three steps, by investigating the following questions:

- Can the larger r_{80} of the quasar images be explained by adding host galaxy flux to a point source?
- Is one galaxy model able to explain the average r_{20}–r_{80} relation for a given quasar?
- Can the entire distribution of quasar data points be represented with a set of simulations created to match the actual conditions of observation?

7.3.1 Simulation of a single observation

To simulate one observation, we created artificial quasar nuclei with surrounding host galaxies as being observed under different external conditions, and studied their behaviour in the $r_{20} - r_{80}$ diagram. The artificial objects were composed of the observed image of a PSF star to represent the nucleus, plus a model galaxy. The numerical model we use is the well-known spheroidal law by de Vaucouleurs (1948):

$$F_{\mathrm{sph}}(r) = F_{\mathrm{sph},0} \exp\left[-7.67 \left(\frac{r}{r_{50}}\right)^{1/4}\right], \tag{7.1}$$

where r_{50} is the radius which encircles half the total flux.

We chose the spheroidal model since it is not unreasonable to expect finding elliptical hosts at redshift $z > 2$. At these redshifts only the brightest quasars are sampled, and only elliptical host galaxies are able to support high-level nuclear activity, at least at lower redshifts (McLeod & Rieke 1995a; Taylor et al. 1996; Dunlop et al. 2003). At high redshift the host galaxies are more disturbed, but the de Vaucouleurs–profile still seems appropriate as a description of the main part of the flux (e.g. Hutchings et al. 2002).

We varied the half-light radius r_{50}, but restricted the tests to E0 galaxies for simplicity. The models were numerically convolved with an empirical PSF as defined by the image of the PSF star, to create a light distribution consistent with the external conditions. Star and convolved object were then added using different ratios of point source to galaxy flux.

The outcome can be seen in Figure 7.7. The solid lines (overplotted over the data for HE 0037–5155) connect simulated quasars that were created having an identical flux ratio between nucleus and host galaxy. These simulated images thus only differ in which PSF star image was used in their creation, and hence only in external observing conditions. After creation, the simulated data was processed in a manner identical to the real data to extract the two parameters. This simulation shows that the artificial quasars cover the same region in the r_{20}-r_{80} diagram as the real object.

7.3.2 Simulation of the average

Since neither the nucleus nor the host galaxy vary during the observation time span, *one* galaxy model, combined with different stars representing different observing conditions, must be able to represent the average distribution of a quasar observation.

In Figure 7.7 we show the result for model galaxy radii of 2.4, 7 and 20 kpc, using fifteen stars along the PSF-line and six different flux ratios, plotted on top of the data for HE 0037–5155. Note that we do not use fifteen different stars but fifteen single images from different data cubes, drawn from the eleven PSF stars observed during the run: these images were chosen because of their proximity to the PSF-line and their roughly equidistant spacing along that line. The tickmarks in the plot show the set of r_{20}-r_{80} values extracted for each artificial object and they are connected by lines of constant point source to host flux ratio.

With increasing host galaxy flux, the slopes of the constant flux ratio lines flatten and they move upwards and to the right in the r_{20}-r_{80} diagram. The flattening can be understood when considering the locus of the extreme case of a pure galaxy without any nucleus. In the limiting case of infinitely bad seeing (high r_{20} values) the galaxy locus and the PSF-line join, since galaxy and star become indistinguishable. As the external conditions improve and the r_{20} values become smaller, the galaxy starts to become more resolved and the difference in r_{80} between point source and galaxy becomes larger and larger, making the galaxy line flatter than the PSF-line. Since the different nucleus to host flux ratios are in between the two extreme cases, they fill the envelope between the PSF-line and the galaxy line and flatten with increasing relative flux contribution from the host.

At this stage we can make our first quantitative statement: Small host galaxies with a half-light radius of only 2.4 kpc are not able to explain the extended flux we measure in HE 0037–5155. Answering the initial question if *one* host galaxy can explain the average distribution is harder. Since we do not know how large the individual errors are and what direction they have, averaging the distribution is not readily done. For this reason it is not possible to uniquely determine a flux ratio and host galaxy radius which best describes the actual data, but by looking at Figure 7.7 we can at least say that it is not unlikely that one of those lines could provide a good fit. At this point we can only select a median line, implying that the as yet unknown noise scatters the datapoints to both directions with the same probability, and use this as input in our most demanding test: the comparison of a simulated distribution to the observed one. Thus, the second question asked cannot be answered until the full description of the problem is utilised.

7.3.3 Simulation of the distribution

In the previous part of the analysis noise was not included, in order to cleanly derive the differing behaviour of point sources with and without a host galaxy in the r_{20}-r_{80} diagram. To incorporate the effects of noise, artificial objects were created in the same manner as before, but were also scaled down to have the mean intensity of a quasar observation. The scaling factor used was determined by the average flux of the quasar data cube inside the central pixel isophote. Next, Gaussian noise was added to give the artificial objects the same S/N as a real quasar observation. The noise level was taken from the object-free quadrants in each image, with the final estimate of the real background being the mean value from the quasar cube frames. Obtaining the background from an annulus is not useful due to the difference in slope inside the annulus between

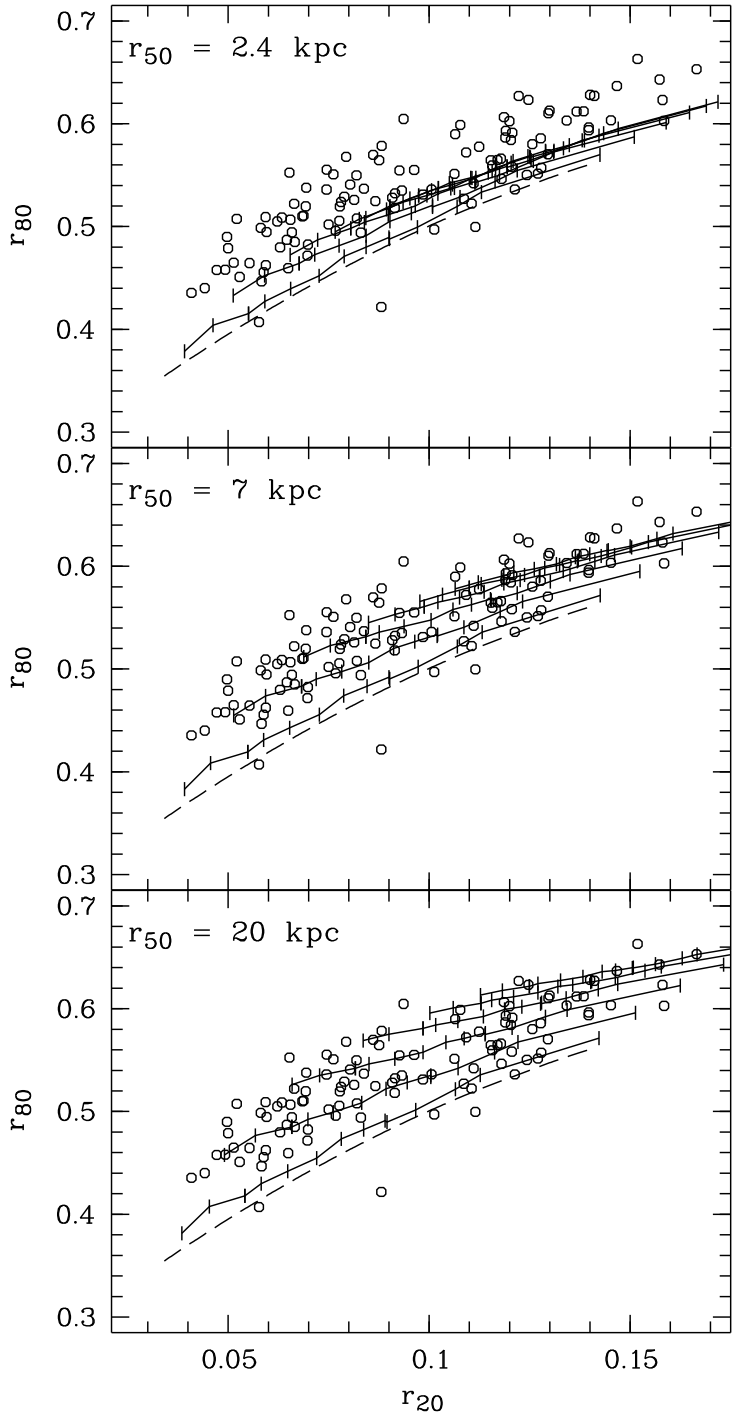

Figure 7.7. Loci for artificial objects with three different model galaxy scale lengths, plotted on top of the data for HE 0037–5155. The scale lengths were computed at the redshift of the quasar. The dashed line is the PSF-line, and the solid lines represent different ratios of nucleus to host flux with the tickmarks showing the location of each object. The flux ratios generating the model quasars were 7.7, 1.5, 0.66, 0.38, 0.23 and 0.16 counting from the line closest to the PSF-line, and the radii are in arcseconds.

the quasar and the brighter star.

It is now possible to investigate the scatter in the distribution introduced by noise around any line of constant flux ratio. To this extent we chose five intervals in r_{20}, which typically contained $7-8$ stellar images. In doing so we selected stars which have a scatter around the PSF-line caused both by noise in the image and by a variation of the PSF shape. When scaled down to mean quasar intensity the noise in the stellar images becomes negligible, while the noise created by shape variation is fully introduced into the artificial quasars. By adding Gaussian noise to each artificial object in a slice, thus recreating the mean S/N of the quasar images in the same slice, the artificial quasars are made to contain both the background noise and the PSF shape variation.

For each object in a slice one hundred noise realizations were computed, and the average value of r_{20} and r_{80} for that slice determined as well as the slope of the major axis of the error ellipse, giving us the errors in r_{20} and r_{80} for the slice. This process is shown schematically in Figure 7.8. The error ellipses were computed both for the assumed best-fitting galaxy and for a zero-galaxy with no flux for all three quasars. This was necessary since the S/N ratios of the quasars differ significantly and since we did not know a priori if the shape of the error ellipses would be dependent on the S/N or flux ratio, which however is not the case.

The narrow scatter we found is dominated by the S/N in the quasar images and can thus be characterised by its large major axis, while the spread in r_{20} mainly is attributable to the width of the stellar slices. Scatter along the minor axis can therefore be reduced by increasing the number of stellar images used, whereas scatter along the major axis only can be diminished by acquiring quasar observations with larger S/N. The variation with r_{20} of the position angles of the slopes of the error ellipses was modelled using all the slices, and the main error diffusion direction over the r_{20}-r_{80} diagram found in this way. We did not model the size of the errorbars, because as long as the minor axis is much smaller than the major axis, the direction of the scatter will be well defined.

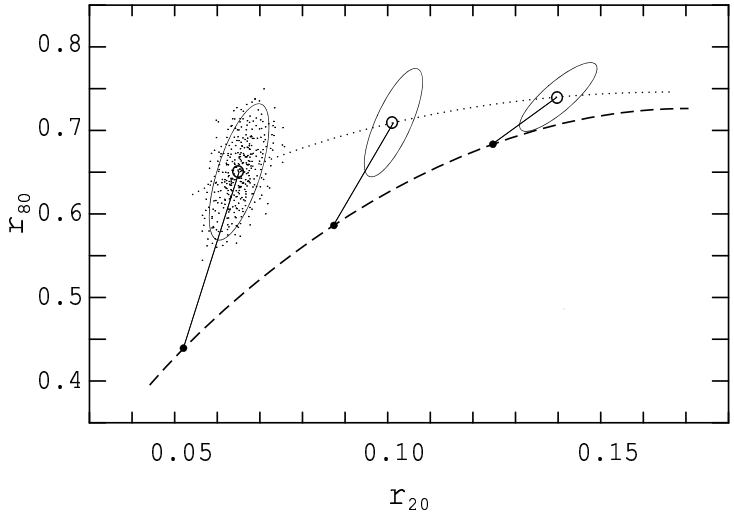

Figure 7.8. Determination of error ellipses. The dashed line is the PSF-line, and the dotted line the line of constant flux ratio. A stellar image on the PSF-line (filled circle), can be made into an artificial object (empty circle). The cloud of points constitute a number of different noise realizations for the artificial object, and the ellipses show the size and slope of the derived 2σ error ellipses.

Knowing the general direction in which noise will move any point on a constant flux ratio line away from that line, the error ellipses can now be used to backtrace the movement performed on each real data point by noise, bringing it back to the most probable location on the flux ratio line from where it was scattered. Combined with the knowledge of which PSF image gave rise

to the error ellipse centred at this location we can assign a unique r_{20} value to each quasar data point, representing the observing conditions under which the data was most probably taken. We stress that the reason for this exercise is not to try to remove noise from an actual observation, which is impossible, but to reveal the underlying distribution in r_{20}-r_{80} space of the point sources which were folded into the quasar images.

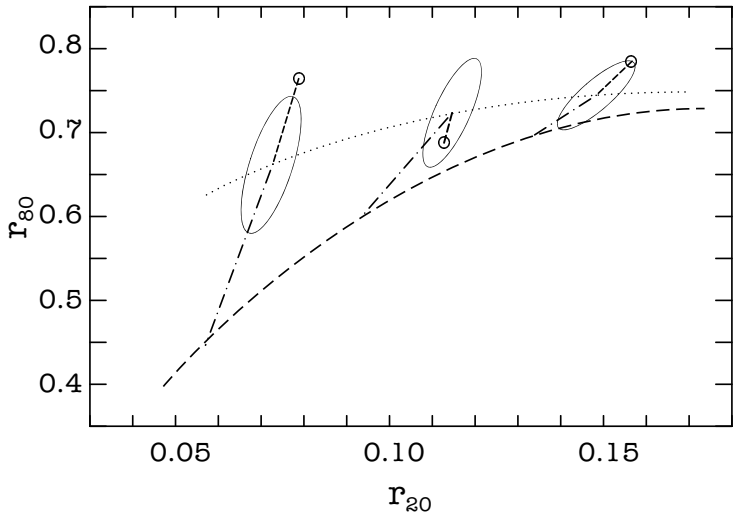

Figure 7.9. Finding the distribution of point sources underlying the quasar images. The circles are real data points, and the dashed and dotted lines as defined in Figure 7.8. For each quasar point there is one error ellipse with the major axis pointing towards it. The dash-dotted line represents tracing the object back to its point source on the PSF-line using the connections established in Figure 7.8.

In Figure 7.9 this task is performed schematically. The first objective is to find the position on the constant flux ratio line which the data point most probably was scattered away from. Each data point can be part of a cloud of noise realizations belonging to any of a number of error ellipses, but there only exists a single error ellipse which has its major axis directed towards the data point in question. The centre of that ellipse represents the r_{20} value which the quasar image was moved away from by noise, assuming no scattering occurs around the minor axis. Secondly, having identified the ellipse centre we can now retrace the known movement of a point source as it is turned into an extended source to find the corresponding position on the PSF-line, which is the PSF of the quasar image. The r_{20} value of this point is defined as the reduced r_{20} value of the quasar image.

With the distribution of the quasars' reduced r_{20} values determined, we can now create simulations having the same flux, the same noise and the same variation of the PSF as the real quasars. A random sample of stellar images with the same distribution in r_{20} as that of a quasar in reduced r_{20} was selected (shown in Figure 7.10), representing the PSF:s prevailing during the observations.

Selecting a matching random sample requires that we have enogh stars to choose from. We therefore had to confine the models to a range of reduced r_{20} which contained enoguh stars, marked by a bar in Figure 7.10.

The resulting distribution of stars match very well to the or the example in Figure 7.10 the null hypothesis (the two samples are *not* drawn from the same distribution) is rejected at 23% probability. Similar matched distributions of stars can be found for the other quasars. At the high end of the range we find stars with matching r_{20}, but they are few and may not represent the true PSF distribution, so we clip at $r_{20} = 0.13$.

However, in the furthest ends of the distribution the stellar r_{20} values do not match the reduced r_{20} values as well. This is owing to an insufficient number of stars in these ranges

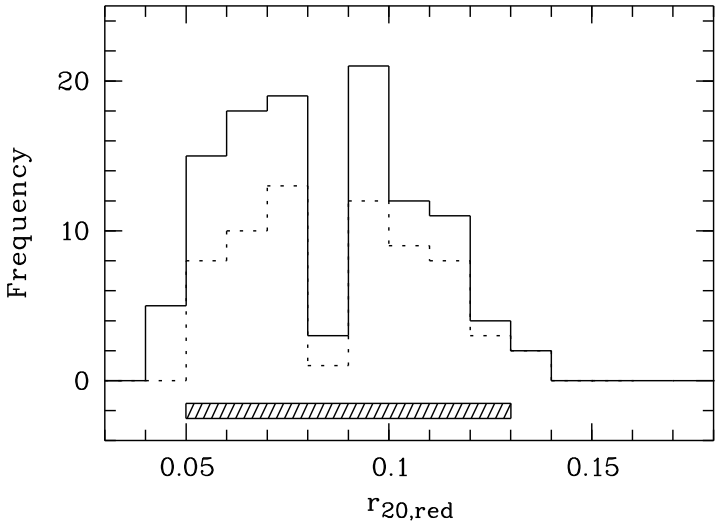

Figure 7.10. The distribution of reduced r_{20} values for HE 0320–1045 (solid line) compared to the distribution of r_{20} values for the selected sample of stellar images (dashed line). The distributions match very well in the area which contains a sufficient amount of stellar images distributed equally around the PSF-line, marked by the hashed bar.

of r_{20}, leading to few stars which have appropriate values for them to be included in the sample. The extreme ends were therefore deselected before modelling the stars into artificial objects having a flux ratio and host galaxy effective radius assumed appropriate for the true quasar images from plots such as Figure 7.7. Noise was added to each computed object, producing ten different numerical realizations per image. The noise level was determined from the object-free quadrants of the quasar images, and was set constant for each quasar since the background noise showed no significant trend or scatter with time or r_{20}.

We have now arrived at a position where it is possible to compare the distribution of quasar data points to the set of simulated images, using Kolmogorov-Smirnov tests. This process is applied to the brightest three quasars in our sample and discussed in the following section.

7.4 Analysis of the individual quasars

The half-light radius is a poorly constrained parameter, as discussed in Section 7.3.2. It is therefore possible to find sets of model quasars which satisfactorily fit the median distribution of quasar images for a broad range of radii. We show in Figure 7.11 for each of the three quasars the loci of three reasonable models, where the position and 2σ errorbar of the model quasar image with the best seeing have been marked with filled symbols. The three model sets were computed using the previously obtained matched samples of stellar images together with galaxy models which have small, medium and large radii respectively. A closer inspection of Figure 7.11 reveals that the degeneration between galaxy radius and N/H ratio is not complete. The position of the model quasar with the best seeing and the size of the scatter both depend on the host galaxy size and can thus be used as constraints when estimating the half-light radius.

We first consider the varying positions of model quasars which were made from the PSF image with the best seeing but with different galaxy models. Since we observed PSF stars and quasars alternatingly it is improbable that the distributions of the underlying $r_{20,\mathrm{red}}$ values differ strongly from the stellar r_{20}-distribution. To make this argument even more firm, we postulate that it is improbable that we observed a quasar at an $r_{20,\mathrm{red}}$ significantly smaller or larger than any r_{20} value we find among all the stars.

To quantify this we compare the r_{20} values of the real quasars to those of the model quasars,

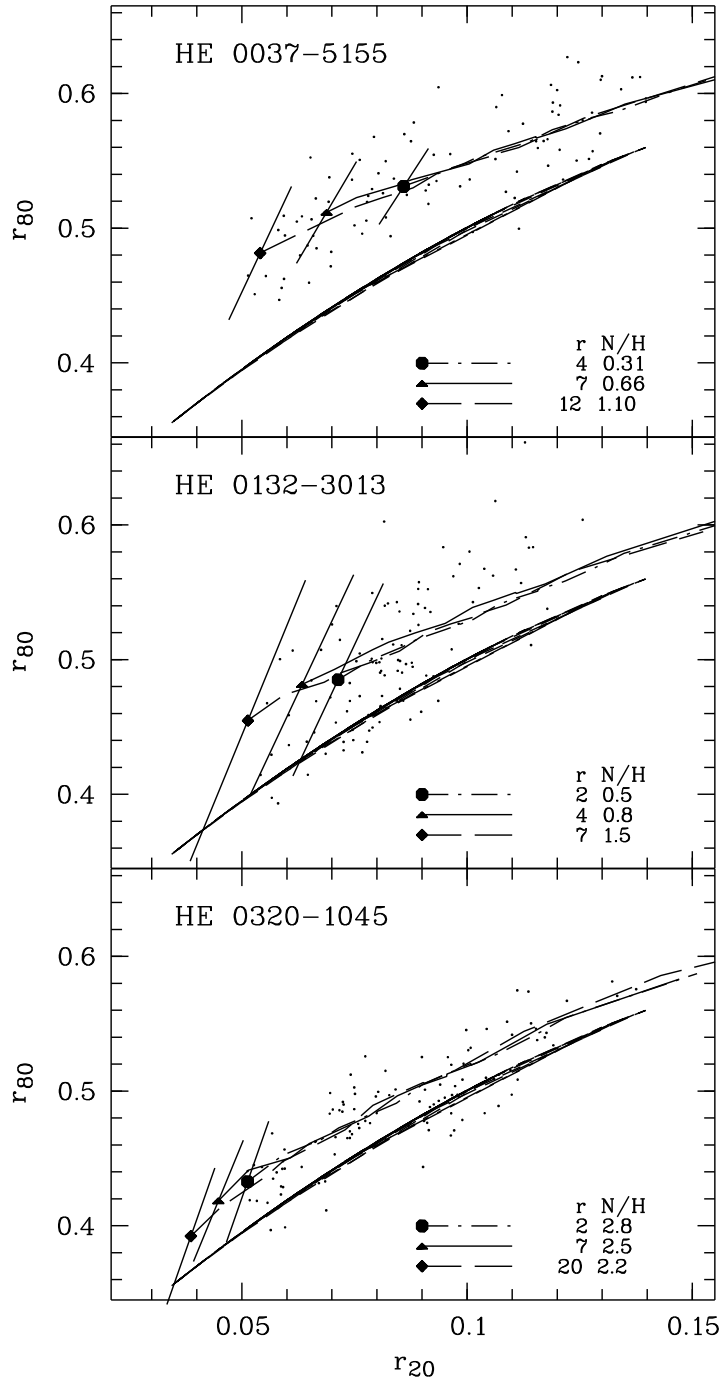

Figure 7.11. Error estimation for the objects. The lines represent the loci of the chosen best model and the two next-to-best models with bracketing values of the half-light radius. Note the moving starting point of the simulations, which for all half-light radii represents the model image created from the best PSF image. N/H is the best-fitting nuclear to host flux ratio and the radii are in kpc.

as this measure is most sensitive to a change in galaxy radius. Small galaxy radii are expected to lead to a lack of model quasars having small r_{20}, since we are unable to find stars which are sufficiently narrow to create such quasar models. The same holds for large galaxy radii, but here we expect a less clear signal since the cutoff in observed PSF stars is not as sharp. Any realistic model should be found in between these two extreme values.

As an illustration we plot in Figure 7.12 the cumulative distributions of the r_{20} values for the object HE 0132–3013 and for model quasars made with different galaxy radii. We can indeed see that for the small galaxy radius too few models are created which have a low r_{20}, leading

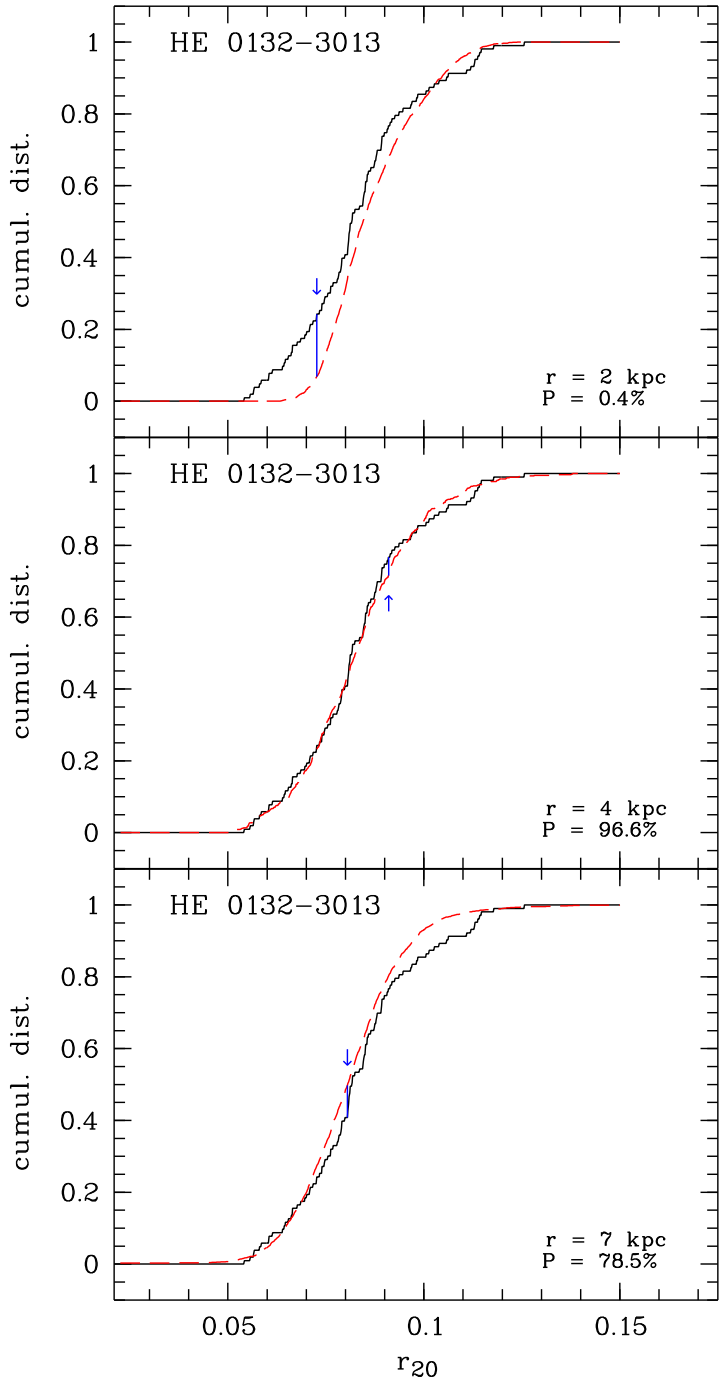

Figure 7.12. Comparison of the r_{20} values of models (dashed red) and observed data (black) for one object and three different galaxy radii, where the greatest difference between the two cumulative distributions is marked by an arrow. The KS statistics found when comparing the cumulative distributions (P) are listed in percent.

to a rejection of this quasar model in a Kolmogorov-Smirnov (KS) test at the 96.2% probability level. For the large galaxy radius the main difference is found at large r_{20}, but as expected it is not significant. In a similar manner we can exclude the small galaxy radius models for the other two objects at the 96.2% (HE 0037–5155) and the 98.1% (HE 0320–1045) probability level. No constraints were found for the large galaxy radius models, however.

Here the second observation from Figure 7.11 comes into play, namely that the size of the scatter also varies with galaxy size. Even if the distributions of r_{20} values for quasars and large galaxy models are compatible, their *two-dimensional* distributions in r_{20}-r_{80} space might not

Table 7.2. Two-dimensional KS-probabilities in percent for the models having half-light radii as listed in Figure 7.11 as well as no host galaxies. A probability below 5% was considered a rejection.

	host galaxy			
Object	small	med.	large	none
HE 0037 – 5155	1.5	7.1	2.1	$1.8 \cdot 10^{-10}$
HE 0132 – 3013	1.2	6.7	1.8	$2.0 \cdot 10^{-3}$
HE 0320 – 1045	0.9	5.6	1.4	$3.3 \cdot 10^{-6}$

be. By comparing these distributions with a two-dimensional KS-test we found in fact that the largest quasar models were rejected for all three objects.

In Table 7.2 we list the two-dimensional KS-probabilities found for all models, where a probability below 5% is considered a rejection. Since the scatter scales monotonically with galaxy radius, we can conclude that any acceptable model must lie within the range of the tested model radii. However, the importance of these Kolmogorov-Smirnoff tests should not be overrated: their main function is not to constrain the value of the half-light radius but to confirm that the chosen (medium size) model is realistic.

The resulting distributions for sets of simulated quasar images made with the chosen models as well as with no host galaxies are plotted in Figure 7.13 together with the real data. For all quasars we find a model so that the hypothesis 'quasars and simulations are *not* drawn from the same distribution' can be rejected (marked 'med.' in Table 7.2), whereas the hypothesis 'quasars and simulations without host contribution are *not* drawn from the same distribution' ('none') cannot be rejected in any case. This implies that our simulations match the data, while the non-detection case can be rejected for all quasars.

We point out that the rejection of non-detections is independent of assumptions of the host galaxy and is derived using only the observational data with their given S/N, since this procedure only compares the PSF stars to the quasars.

The uncertainty in the estimation of the radius is coupled with an uncertainty in the N/H determination. In Figure 7.11 the radii are listed together with the corresponding N/H. By converting the acceptable N/H values to host magnitudes using the average total flux of each quasar image cube and defining the difference $\max(m_K) - \min(m_K)$ as the 4σ interval of the host magnitudes, we can give the error estimates tabulated in Table 7.3. These are solid estimates as we were able to reject the extreme models at a probability lower than a 2σ event ($\approx 5\%$).

Finally we computed high S/N images for each quasar by coadding those individual images used for the above analysis which formed the better half of the set (in terms of seeing) To approximate the composite PSF of the coadded images, we coadded those stellar images which were selected to represent the r_{20} distribution of the quasar images (e.g. for HE 0320–1045 those stars which contributed to the dashed histogram in Figure 7.10 and fulfilled the radial limits indicated by the bar). The PSF was scaled to quasar nuclear flux and subtracted. Luminosity profiles and coadded images are shown in Figure 7.14.

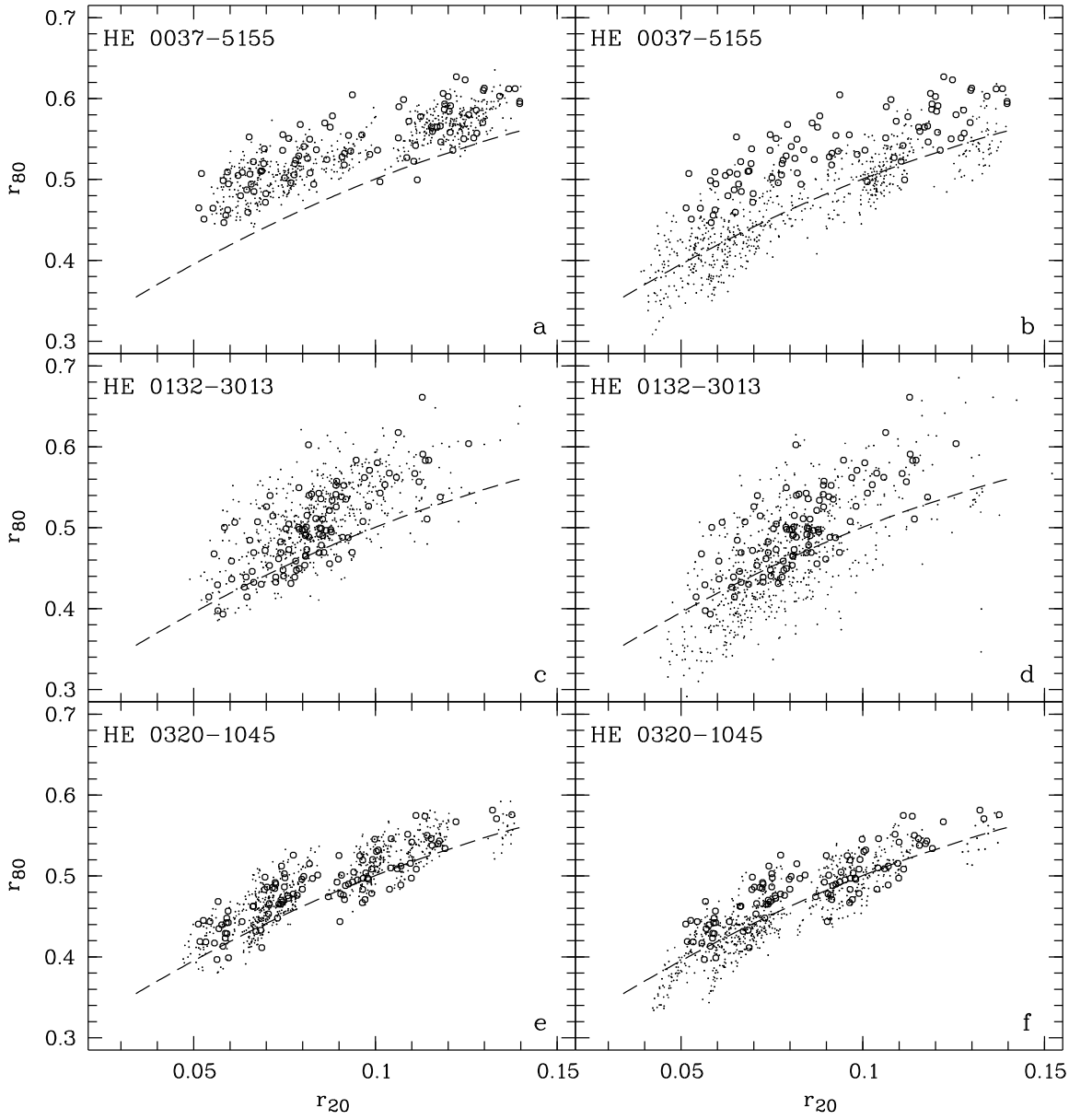

Figure 7.13. Comparison of true and model data. Quasar images are marked by circles, simulated data with dots. The models were computed from a stellar image sample selected to match the actual data as exemplified in Figure 7.10. The left panel side shows the result for models having host galaxy flux and half-light radii as specified in Table 7.3, whereas the panels to the right show models having zero host galaxy flux.

7.5 Discussion

The statistical method we applied has been successful in detecting host galaxies around all of the analysed objects. Magnitudes and scale lengths can be found in Table 7.3. Since the rest-frame *R* band is shifted to observed *K*, the absolute magnitudes were computed without K-correction, but with zero-point and a $(z+1)$ dimming correction to obtain magnitudes in the Vega system.

Table 7.3. Results of the analysis. N/H is the flux ratio between nucleus and host; the r_{50} values are the host galaxy's best-estimate half-light radius in kpc; σ_m is the 1σ magnitude error interval; $m_K^{\rm N}$ and $m_K^{\rm H}$ the nucleus and host apparent magnitudes in K band; $M_R^{\rm N}$ and $M_R^{\rm H}$ the nucleus and host absolute magnitudes in R band; L/L^* the host luminosity in fractions of the Schechter luminosity.

Object name	z	N/H	r_{50}	σ_m	$m_K^{\rm N}$	$m_K^{\rm H}$	$M_R^{\rm N}$	$M_R^{\rm H}$	L/L^*
HE 0037 – 5155	2.127	0.7	7^{+5}_{-3}	0.13	16.35	15.90	−26.87	−27.32	19
HE 0132 – 3013	2.229	0.8	4^{+3}_{-2}	0.14	16.74	16.50	−26.63	−26.87	11
HE 0320 – 1045	2.282	2.5	7^{+13}_{-5}	0.05	15.15	16.14	−28.29	−27.30	15

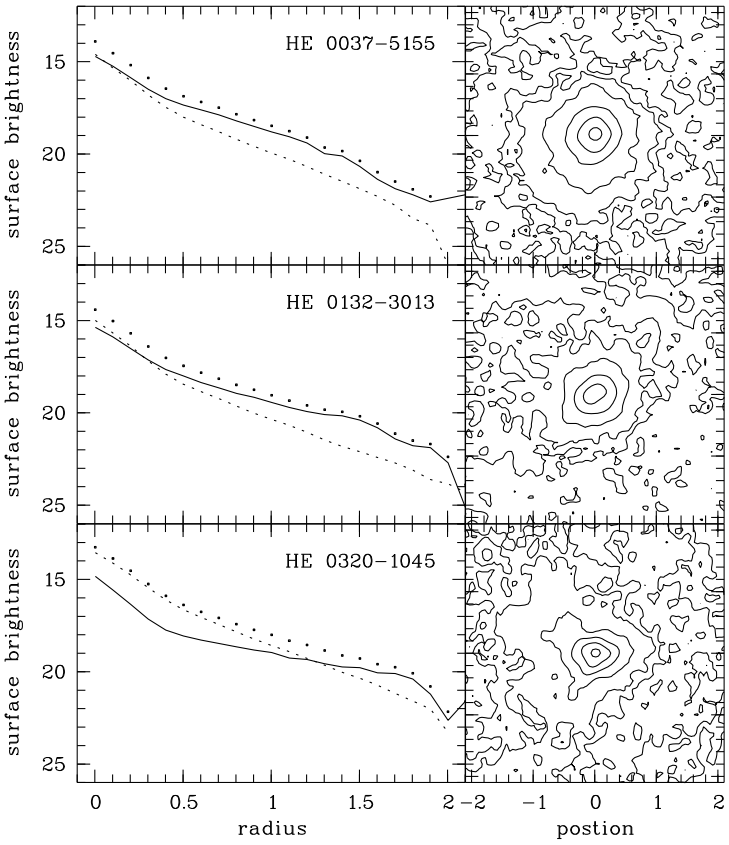

Figure 7.14. Coadded images. To the left are the luminosity profiles of the data (points), the scaled coadded PSF (dotted line) and the remaining flux after subtraction of the PSF (solid line). To the right are contour plots of the residual at 1 mag spacing. The lowest isophote is 20 mag/□″ and the radii are in arcsec.

Due to the very strict selection criteria of the adaptive optics system, the sample objects could not be confined to redshift bins which are free of emission lines. Most notably, the Hα emission line lies within the filter profile for all objects. One possible source of extended Hα emission is scattered light from the quasar nucleus. In radio galaxies at $z \sim 1$ the scattered component has been shown to be $\leq 10\%$ in K band by near-IR polarimetry (Leyshon & Eales 1998) and multicolour imaging (Rigler et al. 1992). Assuming a scattered nuclear light fraction of this size results in a negligible contribution to the host galaxy magnitude for the objects having N/H < 1. In the case of HE 0320–1045 the strength of the nuclear emission could contribute to the extended flux, though the actual amount of scattered flux cannot be quantified without access to colour information.

Star-forming regions are another source of extended Hα emission. Moorwood et al. (2000) investigated a sample of $z \approx 2.2$ Hα-emitting galaxies and found that $L_{\mathrm{H}\alpha}/L_K \approx 1/5$ with L_K the galaxy's luminosity in the K band. If the results are portable to our galaxies which are on average five magnitudes brighter (which is not unreasonable, see Vílchez & Iglesias-Páramo 1998), line emission from star-forming regions will increase the host galaxy luminosity by up to 0.2 magnitudes. As we have no spectral information in the region of interest nor means to predict the Hα luminosities, we cannot correct for this shift.

Another significant contribution to the host galaxy luminosity could come from close companions or foreground objects. In other studies of host galaxies at high redshift this is a relatively common feature, being the case for $\simeq 40\%$ of the sample in the investigations of Lehnert et al. (1999), Ridgway et al. (2001) and Hutchings (1995). Since the effective field size used here is only 6.4×6.4 arcsec^2 due to the chopping between quadrants, no conclusions can be drawn on the density of field galaxies in the vicinity of our objects. However, in the direct images (Figure 7.14) we see no signs of foreground galaxies or companions for two of the quasars. HE 0320–1045 on the other hand has two extended features to the NE and SE which contain $\approx 50\%$ of the host galaxy flux as measured at $r = 0\farcs6$. In combination with the very pronounced core in the host galaxy luminosity profile (solid line in Figure 7.14) this clearly indicates a host galaxy which is disturbed or accompanied by other galaxies. Without any redshift information, we cannot evaluate the importance of foreground contamination.

All these effects will systematically brighten our host galaxies, but we estimate that the cumulative effect will be smaller than 0.5 magnitudes. Even within these error limits all three host galaxies are bright, but not surprisingly so. As the HES is a bright quasar survey we will detect only the brightest members ($M_{\mathrm{tot}} \lesssim -28.2$ in J band) of the quasar population at $z = 2.2$, which according to the studies of McLeod & Rieke (1995a) and McLeod & McLeod (2001) should reside in highly luminous host galaxies (but see the discussion below).

To compute the luminosity of the hosts in multiples of L^*, we use a characteristic Schechter magnitude of $M_R^* = -21.8$ at $z = 0$ (Lin et al. 1996). Accounting for the effect of passive evolution which makes an elliptical galaxy about 2.5 magnitudes brighter in rest-frame R band at $z = 2$ (Fioc & Rocca-Volmerange 1997) results in $K^* = 19.0$. Thus we find that the luminosity of our host galaxies is $11 - 19\ L^*$.

Luminosities observed by other authors range from a few L^* (Kukula et al. 2001; Ridgway et al. 2001; Hutchings et al. 2002) up to $15 - 45 L^*$ (Aretxaga et al. 1998,?; Lehnert et al. 1992). Since the selection criteria and pass-bands in which these samples were observed as well as the method of analysis vary strongly, a direct comparison is not straightforward. The study most closely resembling ours both in terms of redshift and passband used is that of Lehnert et al. (1992) who observed radio-loud quasars in K band at $z = 2 - 3$. The mean total magnitude of the three objects in their investigation which have $z \simeq 2.2$ is $K = 15.7$ while the residuals have a mean magnitude of $K = 17.6$. In contrast, our total mean magnitude is $K = 15.3$ and our mean host magnitude is $K = 16.2$. It should however be noted that Lehnert et al. perform flat-top PSF subtraction within a 2 arcsec^2 box, resulting in significant flux transfer from host to nucleus which makes their host magnitudes upper limits only.

In Figure 7.15 we plot nuclear luminosities against host luminosities for our objects and also include the $z \sim 2$ sample of Kukula et al. (2001), which was recomputed to R band using the colour relations $(B-R)_{nuc} = 0.71$ (Schade et al. 2000) and $(V-R)_{sph} = 0.57$ (Fioc & Rocca-Volmerange 1997). The line in Figure 7.15 marks the locus of quasars radiating at 10% of the

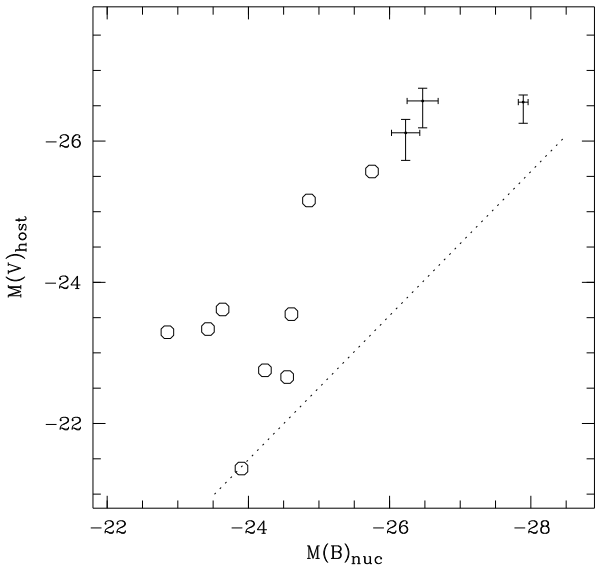

Figure 7.15. Nuclear versus host luminosities. Dots mark our data and circles mark hosts from the $z \sim 2$ sample of Kukula et al. (2001). The dotted line is the 10% Eddington-limit for $z = 0$ from Schade et al. (2000), converted to Vega magnitude system. The errorbars are asymmetric due to possible Hα contamination.

Eddington luminosity, derived at low redshift (Schade et al. 2000). The connection between the Eddington accretion rate and the mass of the nuclear black hole driving the quasar activity is expressed in an upper bound to the luminosity found for low-redshift quasars, so that there is a limit to the maximum nuclear luminosity sustainable in a host of given brightness (McLeod & Rieke 1995a; McLeod & McLeod 2001). At low redshifts the accretion rates range between a few percent up to $\sim 20\%$ of the Eddington rate. At high redshifts the exact location of Eddington limits in the nuclear-to-host luminosity plot are essentially unknown since they depend on the mass-to-light ratio and on the relation between bulge mass and black hole mass, neither of which is well determined at high redshifts. The line in Figure 7.15, though suggestive, can therefore not form the basis of further analysis.

The determination of the host galaxy radii is also fraught with difficulties. We have assumed a spheroidal morphology when modelling the hosts since local high-luminosity galaxies preferentially are of this type, but at high redshifts this may however not be the case. Furthermore, since the observations are not free from Hα emission we do not track the evolved stellar component typical for early-type galaxies. Finally, foreground objects or close companions may seriously disturb the shape. While HE 0037–5155 and HE 0132– 3013 are well-behaved, the value of the half-light radius found for HE 0320–1045 may be influenced upwards by the presence of the extended features.

In general though, the typical host galaxy scale size of $\sim 4-7$ kpc is not much larger than the $3-5$ kpc found for the high-redshift objects detected by Ridgway et al. (2001), Falomo et al. (2001) and Aretxaga et al. (1998). Compared to host galaxies at low and intermediate redshifts where scale sizes range between $8-15$ kpc (McLure et al. 1999; Kotilainen et al. 1998) the higher redshift hosts are thus more compact.

7.6 Conclusions

Careful determination of the PSF is required when adaptive optics is used for the analysis of host galaxies, or any kind of extended object on which a point source is superimposed. The statistical method presented in this chapter satisfactorily manages to overcome the difficulties of

non-simultaneous PSF calibrator observations which normally are needed for AO observations, and can be used in any number of applications provided that the underlying extended source can be represented by models.

The method was applied to three bright high-redshift quasars observed in the near-infrared. For each of these we have shown that the distribution of individual images can be represented by a single set of host galaxy parameters. Images of PSF stars matched to the conditions prevailing during quasar observation were combined with a best-estimate host galaxy model resulting in distributions which successfully simulate those of the data, while the non-detection case can be rejected for all quasars.

The detected host galaxies are bright and compact. The mean absolute magnitude in the R band is -27.2, which translates to a luminosity of $11-19\times L^*$, and the scale lengths are typically $4-7$ kpc. In direct images only one object appears undisturbed (HE 0132– 3013), while the others show non-concentric isophotes (HE 0037–5155) or even a severely disturbed geometry (HE 0320–1045).

The inclusion of the Hα emission line in the filter profile introduces an uncertainty in the host magnitudes which is not easy to quantify. Spectral information is essential for investigation of the importance of star-forming regions in these objects, while also making it possible to determine whether the disturbed appearance of HE 0320–1045 is due to foreground objects or if an actual merger is taking place. The on-nuclear two-dimensional modelling of the nucleus and host spectrum developed by Jahnke (2002) will allow a detailed such analysis.

The choice of galaxy model is certainly a pivotal point in the quantification of the host galaxy detection. However, until we have a better understanding of the processes which lead to quasar activity at high redshift, or have a larger sample with which to analyse the residual host galaxy after subtraction of the nuclear component, a simple, low-order model is easier to control and will lead to more stable results than any high-order model.

Further improvement is expected for data with superior quality. Quasar observations restricted to good or excellent seeing conditions would make it easier to exclude host galaxies with large radii in the one-dimensional KS-test. To achieve higher significance of the two-dimensional test we either need less scatter, which calls for a larger telescope, or more data-points. As our method is independent of temporal variations of the PSF the latter can easily be attained.

The collected number of high redshift quasars suitable for AO observations is as yet not very large. But since the angular extension of a host galaxy will remain roughly constant beyond $z\sim 1.2$ (slowly increasing beyond $z\sim 2$ due to the falling half-light radius but the growing angular size), the main constraint in moving to even higher redshifts is the luminosity of the sources, not resolution. A search for suitable quasars in catalogues with fainter limits (e.g. in the Sloan Digital Sky Survey, Schneider et al. 2002) should reveal a greater number of targets. Still, until laser guide stars system are operative, the number of targets will be limited.

Quasar host observations with adaptive optics and with the Hubble Space Telescope are thus complementary to each other. While both suffer from a complex PSF determination, HST has the advantage of a complete sky coverage. But for sources with a nearby bright star, AO can go much deeper than HST which is important in order to understand the morphological features of host galaxies at high redshifts.

This chapter is based on a paper soon to be submitted written by Björn Kuhlbrodt, E. Örndahl, Lutz Wisotzki and Knud Jahnke

8 Conclusions

8.1 Summary

The importance of proper application of statistical methods when making general statements about an ensemble can not be overrated. Without this, any statement, no matter how large the sample may be, is irrelevant. Consequently, in this work we have concentrated on developing a mathematically correct method with known limitations to make firm statements about the population of luminous quasars and their host galaxies.

The basis of a quasar host galaxy analysis, by the means of optical or near-infrared imaging, is the removal of nuclear light. As the angular extent of the nucleus is very small compared to theoretical resolution of optical instruments, it will be a point-source and thus be mapped like a star. An a priori determination of the point-spread function (PSF) and hence the quasar nuclear light distribution will greatly facilitate any attempt to decompose the image into nuclear and galactic light and will help to to minimise the confusion between both.

The PSF however is subject to both temporal and spatial variation on the detector. By assuming that the PSF can be approximated with a single stellar image or by averaging of several stars, inaccuracies in the PSF shape are risen. These inaccuracies were shown the have – in our implementation – a much stronger influence on the errors of the retrieved host galaxy parameters than the notorious background determination. As this error propagation is induced by the most basic principle – the nucleus can be represented by the PSF – we suspect that the size of the induced errors will be of the same order for all methods based on that principle and suggest that other methods are tested for their sensitivity to the PSF errors.

The cornerstones of our method of decomposition are:

- A computation of the quasar PSF with a spatially variable analytic model which is complemented with radial and two-dimensional empiric lookup tables.
- Determination of a best-fit two-dimensional quasar model which is composed of one or two analytic point-symmetric galaxy components, convolved with the PSF and a PSF image for the quasar nucleus.
- Extensive Monte-Carlo-simulations tailored to resemble each sample observed.

The PSF part was written in the attempt to optimise the QSO PSF approximation for common ground-based telescopes. To model the spatial variation of the PSF, an analytic point-symmetric model is most useful, as the parameters can be made a function of the location on the detector. This is combined with a radial LUT which compensates differences between the detector PSF profile and the analytic representation. Any non-point-symmetric features can be accounted for with a two-dimensional LUT. In such fashion we are also able to treat HST images, to which we currently adept our methods.

The number of stars in the image is a crucial factor in the accuracy of the reconstructed PSF. While the method runs optimally for a number of stars large enough to characterise the spatial variation, we always use all information available, i.e. all non-saturated stars and even faint stars. We therefore believe that our method is close to an optimal PSF estimation method and will also useful to other decomposition and deconvolution applications.

The such determined PSF is then used to convolve the galaxy model and as a model for the quasar nucleus. The determination of the best-fitting parameters is done with an adapted downhill simplex minimization.

By making extensive simulations we have shown that our implementation of host galaxy image decomposition is robust and unbiased. With this approach, we are now able to analyse data in a large range of redshift consistently with known uncertainties.

The initial sample was a small but complete sample of 12 nearby Seyfert galaxies. The analysis has shown that the host galaxies are mostly (by 64 %) disk-like galaxies with a slight tendency for an overfrequency of tidal interaction when compared to inactive galaxies. The spiral galaxies were also found one magnitude brighter then field galaxies, while early type galaxies agreed with their inactive counterparts.

In order to make statements about the quasar host galaxy luminosities and possibly the lifetime of a quasar, we analysed a low- to medium-redshift sample with 44 luminous quasars objects from the HES at $z < 0.35$, complemented with a sample of 66 less luminous quasars at $z < 0.16$ published by Schade et al. (2000). We have shown that all of the objects radiate below the Eddington luminosity. Recent claims of super-luminous quasars by Percival et al. (2001) were shown to be compatible to sub-Eddington rate if we apply the nuclear $B-H$ colour transformation measured by us. We confirm however the large rate (63 %) of disk-like galaxies among the host galaxies of luminous quasars.

The true innovation in the following analysis was the application of the concept of bi-variate luminosity functions onto the quasars and their host galaxies. With these QHGLFs we can easily implement the boundary of maximum Eddington efficiency and look for dependencies between nuclear and galactic luminosities. With this we computed the host galaxy luminosity function and found considerably less faint galaxies than expected from the field galaxy LF. Further analysis with dependencies between the nuclear luminosity and host galaxy typical luminosity or the slope of the faint end of the HGLF showed indications for a dependency between nuclear luminosity and the fraction of faint galaxies, as the faint-end slopes drops even steeper for bright nuclei. It could not be decided whether this is an intrinsic effect or if it is caused by random losses of faint host galaxies.

Assuming that the host galaxy luminosity function is a scaled version of the field galaxy luminosity function, we translate the fraction of active galaxies into a lower limit for the quasar dutycyle of 2 Myr $\lesssim t_{\rm accr} \lesssim$ 40 Myr.

For a small sample of three high-redshift objects observed with adaptive optics our decomposition method is not optimal. Due to the highly variable PSF and the small fields of view, individual PSFs for single images are not available. Instead we used the argument that in interleaving observations the quasar PSFs and the PSFs determined from dedicated stellar observation should statistically be the same. With this we were able to model the observations and estimate the host galaxy brightnesses of three quasars. The recovered host galaxies are bright ($M_V \lesssim -26$) but compact with scale lengths amounting to typically $4-7$ kpc. Two of the three host galaxies show asymmetric isophotal shapes.

8.2 Outlook

In this study we developed fast and robust methods to analyse quasar image and study their statistical properties. The methods of PSF determination, image decomposition and bivariate QHGLF computation are versatile and expandable and we plan to use them in several projects:

- We already finished observations of an extension of the previously described 'HES' sample. We selected a second – complete – sample of quasars at $0.35 < z < 0.45$. By going to higher redshifts we sample more bright quasars, a regime of nuclear luminosities which was yet covered only marginally. Extending the range of nuclear luminosities will help specify the suspected dependence of nuclear and galactic luminosity more clearly. And an increased sample size will reduce the uncertainties.

- We also observed a second set of 40 multicolour images in *BVRH* and some images in *I* and *K* of low-redshift quasars selected from the PG survey (Schmidt & Green 1983). By including *B* band in the filterset we can more reliably determine the young populations in quasar host galaxies, an important tracer of recent gas accretion events.

- We are currently working on the extension to HST images, which requires to move the focus of the PSF determination from the modelling of the spatial variation to the treatment of non-pointsymmetric features. This would open the possibility to analyse the extensive data from the HST archive.

- We also plan to analyse data from other telescope archives, most notably the VLT. Application of the QHGLF computation on archive data is however hampered by unknown selection effects. Only the combination of samples with known completeness limits can lead to sound statistical statements.

- With larger samples we plan to analyse the evolution of host galaxies by introducing redshift-dependent parameters (e.g. $M^*_{\rm gal}(z)$) into the QHGLF.

The most interesting project is the analysis of COMBO-17 ('Classifying Objects by Medium-Band Observation in 17 Filters', Wolf et al. 2003) wide-field images. COMBO-17 is a deep multicolour-survey in 5 broad-band filters, *UBVRI*, complemented by 12 medium-band filters, which allow the computation of precise photometric redshifts. Within an area of $1\square^{\rm o}$ redshifts of ≈ 50000 galaxies and several hundred quasars will be available. This will give us the unique chance to analyse quasars at redshifts $1 < z < 5$ (Wolf et al. 2003) and galaxies up to $z = 1.2$ (Wolf et al. 2003) *in the same survey*, greatly facilitating the comparison between active and inactive galaxies. Combined with multi-colour information, the identification of the parent population of quasars or even subclasses of quasars is feasible.

For an area of 900 $\square'$ within a COMBO-17 field (the Chandra Deep Field South) HST images in two filters (F606W and F850LP) are available through the GEMS ('Galaxy Evolution From Morphology And SEDs') project (Beckwith et al. 2002). Owing to the high resolution of HST, this offers the possibility to decompose quasar images up to even higher redshifts.

With this amount data, we will be able to compute LFs for active and non-active galaxies for a large range of redshifts in a well-defined and large sample and test these results against predictions of quasar formation scenarios. This will greatly increase our understanding of the quasar phenomenon.

Bibliography

Abraham R. G., Crawford C. S., McHardy I. M., 1992, ApJ, 401, 474

Antonucci R., 1993, Ann. Rev. A&A, 31, 473

Aretxaga I., Boyle B. J., Terlevich R. J., 1995, MNRAS, 275, L27

Aretxaga I., Le Mignant D., Melnick J., Terlevich R. J., Boyle B. J., 1998, MNRAS, 298, L13

Aretxaga I., Terlevich R. J., Boyle B. J., 1998, MNRAS, 296, 643

Baggett W. E., Baggett S. M., Anderson K. S. J., Hamabe M., 1992, American Astronomical Society Meeting, 24, 1223

Bahcall J. N., Kirhakos S., Saxe D. H., Schneider D. P., 1997, ApJ, 479, 642

Beckert T., Duschl W. J., 2002, A&A, 387, 422

Beckwith S. V. W., Rix H.-W., Peng C., McIntosh D., Caldwell J., Meisenheimer K., Wolf C., Wisotzki L., Borch A., Haeussler B., Barden M., GEMS Collaboration 2002, American Astronomical Society Meeting, 201, 0

Binney J., Merrifield M., 1998, Galactic Astronomy. Princeton University Press

Boyce P. J., Disney M. J., Blades J. C., Boksenberg A., Crane P., Deharveng J. M., Macchetto F. D., Mackay C. D., Sparks W. B., 1998, MNRAS, 298, 121

Boyle B. J., Griffiths R. E., Shanks T., Stewart G. C., Georgantopoulos I., 1993, MNRAS, 260, 49

Boyle B. J., Shanks T., Croom S. M., Smith R. J., Miller L., Loaring N., Heymans C., 2000, MNRAS, 317, 1014

Boyle B. J., Shanks T., Peterson B. A., 1988, MNRAS, 235, 935

Brandt S., 1992, Datenanlyse, 3 edn. BI Wissenschaftlicher Verlag, Mannheim

Bronstein I. N., Semedjajew K. A., 1991, Taschenbuch der Mathematik, 21. edn. B. G. Teubner, Stuttgart/Leipzig

Cattaneo A., 2001, MNRAS, 324, 128

Cole S., Norberg P., Baugh C. M., Frenk C. S., Bland-Hawthorn J., Bridges T., Cannon R., Colless M., Collins C., Couch W., Cross N., Dalton G., De Propris R., Driver S. P., Efstathiou G., et al., 2001, MNRAS, 326, 255

Collin S., Boisson C., Mouchet M., Dumont A.-M., Coupé S., Porquet D., Rokaki E., 2002, A&A, 388, 771

Conselice C. J., Bershady M. A., Jangren A., 2000, ApJ, 529, 886

Corbin M. R., 2000, ApJL, 536, L73

da Costa L. N., Willmer C. N. A., Pellegrini P. S., Chaves O. L., Rité C., Maia M. A. G., Geller M. J., Latham D. W., Kurtz M. J., Huchra J. P., Ramella M., Fairall A. P., Smith C., Lípari S., 1998, AJ, 116, 1

de Grijs R., 1998, MNRAS, 299, 595

de Robertis M. M., Yee H. K. C., Hayhoe K., 1998, ApJ, 496, 93

de Vaucouleurs G., 1948, Ann. Astrophys., 11, 247

della Ceca R., Maccacaro T., Gioia I. M., Wolter A., Stocke J. T., 1992, ApJ, 389, 491

Devillard N., 2001, in ASP Conf. Ser. 238: Astronomical Data Analysis Software and Systems X Vol. 10. pp 525+

Duda R., Hart P., 1973, Pattern Classification and Scene Analysis. Wisley

Dultzin-Hacyan D., Krongold Y., Fuentes-Guridi I., Marziani P., 1999, ApJL, 513, L111

Dunlop J. S., McLure R. J., Kukula M. J., Baum S. A., O'Dea C. P., Hughes D. H., 2003, MNRAS, 340, 1095

Eisenhauer D., 1997, SHARP II+ User Guide. http://www.ls.eso.org/lasilla/Telescopes/360cat/-adonis/docs/SharpUserManual.ps.gz

Elvis M., Wilkes B. J., McDowell J. C., Green R. F., Bechtold J., Willner S. P., Oey M. S., Polomski E., Cutri R., 1994, ApJS, 95, 1

Eskridge P. B., Frogel J. A., Pogge R. W., Quillen A. C., Davies R. L., DePoy D. L., Houdashelt M. L., Kuchinski L. E., Ramírez S. V., Sellgren K., Terndrup D. M., Tiede G. P., 2000, AJ, 119, 536

Falomo R., Kotilainen J., Treves A., 2001, ApJ, 547, 124

Filippenko A. V., Sargent W. L. W., 1989, ApJ, 342, L11

Fioc M., Rocca-Volmerange B., 1997, A&A, 326, 950

Fioc M., Rocca-Volmerange B., 1999, A&A, 351, 869

Franceschini A., Hasinger G., Miyaji T., Malquori D., 1999, MNRAS, 310, L5

Freeman K. C., 1970, ApJ, 160, 812

Fukugita M., Shimasaku K., Ichikawa T., 1995, PASP, 107, 945

Gioia I. M., Maccacaro T., Schild R. E., Wolter A., Stocke J. T., Morris S. L., Henry J. P., 1990, ApJS, 72, 567

Glass I. S., 1981, MNRAS, 194, 795

Graham A. W., 2002, MNRAS, 334, 721

Grazian A., Cristiani S., D'Odorico V., Omizzolo A., Pizzella A., 2000, AJ, 119, 2540

Green R. F., Williams T. B., Morton D. C., 1978, ApJ, 226, 729

Hamilton T. S., Casertano S., Turnshek D. A., 2002, ApJ, 576, 61

Heckman T. M., Miley G. K., Lehnert M. D., van Breugel W., 1991, ApJ, 370, 78

Hernquist L., Mihos J. C., 1995, ApJ, 448, 41

Ho L. C., Filippenko A. V., Sargent W. L. W., 1997, ApJ, 487, 568

Hoyle F., Fowler W. A., 1963, MNRAS, 125, 169

Huang J.-S., Glazebrook K., Cowie L. L., Tinney C., 2003, ApJ, 584, 203

Hutchings J. B., 1995, AJ, 110, 994

Hutchings J. B., Crampton D., Morris S. L., Durand D., Steinbring E., 1999, AJ, 117, 1109

Hutchings J. B., Crampton D., Morris S. L., Steinbring E., 1998, PASP, 110, 374

Hutchings J. B., Frenette D., Hanisch R., Mo J., Dumont P. J., Redding D. C., Neff S. G., 2002, AJ, 123, 2936

Hutchings J. B., Morris S. L., Crampton D., 2001, AJ, 121, 80

Jahnke K., 2002, PhD thesis, Universität Hamburg

Jørgensen I., Franx M., Kjærgaard P., 1996, MNRAS, 280, 167

Kauffmann G., Haehnelt M., 2000, MNRAS, 311, 576

Kembhavi A. K., Narlikar J V., 1999, Quasars and Active Galactiv Nuclei. Cambridge University Press

Kochanek C. S., Pahre M. A., Falco E. E., Huchra J. P., Mader J., Jarrett T. H., Chester T., Cutri R., Schneider S. E., 2001, ApJ, 560, 566

Köhler T., Groote D., Reimers D., Wisotzki L., 1997, A&A, 325, 502

Kopka H., 1996, LaTeX: Einführung, 2. edn. Addison-Wesley, Bonn

Kormendy J., 1977, ApJ, 217, 406

Kormendy J., Gebhardt K., 2002, in Martel H., Wheeler J. C., eds, The 20th Texas Symposium on Relativistic Astrophysics

Kotilainen J. K., Falomo R., Scarpa R., 1998, A&A, 332, 503

Kristian J., 1973, ApJ, 179, L61

Kukula M. J., Dunlop J. S., McLure R. J., Miller L., Percival W., Baum S. A., O'Dea C. P., 2001, MNRAS, 326, 1533

Laor A., 1998, ApJ, 505, L83

Le Mignant D., et al., 1998, in , ESO/OSA Topical meeting on Astronomy with Adaptive Optics: Present Results and Future Programs

Lehnert M. D., Heckman T. M., Chambers K. C., Miley G. K., 1992, ApJ, 393, 68

Lehnert M. D., van Breugel W. J. M., Heckman T. M., Miley G. K., 1999, ApJS, 124, 11

Leyshon G., Eales S. A., 1998, MNRAS, 295, 10

Lin H., Kirshner R. P., Shectman S. A., Landy S. D., Oemler A., Tucker D. L., Schechter P. L., 1996, ApJ, 464, 60

Lin H., Yee H. K. C., Carlberg R. G., Morris S. L., Sawicki M., Patton D. R., Wirth G., Shepherd C. W., 1999, ApJ, 518, 533

Loveday J., 2000, MNRAS, 312, 557

Lowenthal J. D., Heckman T. M., Lehnert M. D., Elias J. H., 1995, ApJ, 439, 588

Lucy L., 1974, AJ, 79, 745

McLeod K. K., McLeod B. A., 2001, ApJ, 546, 782

McLeod K. K., Rieke G. H., 1994, ApJ, 431, 137

McLeod K. K., Rieke G. H., 1995a, ApJ, 441, 96

McLeod K. K., Rieke G. H., 1995b, ApJ, 454, L77

McLeod K. K., Rieke G. H., Storri-Lombardi L. J., 1999, ApJ, 511, L67

McLure R. J., Dunlop J. S., 2002, MNRAS, 331, 795

McLure R. J., Kukula M. J., Dunlop J. S., Baum S. A., O'Dea C. P., Hughes D. H., 1999, MNRAS, 308, 377

Magain P., Courbin F., Sohy S., 1998, ApJ, 494, 472

Magorrian J., Tremaine S., Richstone D., Bender R., Bower G., Dressler A., Faber S. M., Gebhardt K., Green R., Grillmair C., Kormendy J., Lauer T., 1998, AJ, 115, 2285

Márquez I., Petitjean P., Théodore B., Bremer M., Monnet G., Beuzit J.-L., 2001, A&A, 371, 97

Marshall H. L., 1987, AJ, 94, 628

McLure R. J., Dunlop J. S., Kukula M. J., 2000, MNRAS, 318, 693

Metcalfe N., Ratcliffe A., Shanks T., Fong R., 1998, MNRAS, 294, 147

Moffat A. F. J., 1969, A&A, 3, 455

Möllenhoff C., Heidt J., 2001, A&A, 368, 16

Moorwood A. F. M., van der Werf P. P., Cuby J. G., Oliva E., 2000, A&A, 362, 9

Morton D. C., Williams T. B., Green R. F., 1978, ApJ, 219, 381

Patton D. R., Carlberg R. G., Marzke R. O., Pritchet C. J., da Costa L. N., Pellegrini P. S., 2000, ApJ, 536, 153

Percival W. J., Miller L., McLure R. J., Dunlop J. S., 2001, MNRAS, 322, 843

Poggianti B., 1997, A&AS, 122, 399

Press W. H., Teukolsky S. A., Vetterling W. T., Flannery B. P., 1995, Numerical recipes in C, 2nd edn. Cambridge University Press

Ravindranath S., Ho L. C., Peng C. Y., Filippenko A. V., Sargent W. L. W., 2001, AJ, 122, 653

Ridgway S. E., Heckman T. M., Calzetti D., Lehnert M., 2001, ApJ, 550, 122

Rigler M. A., Stockton A., Lilly S. J., Hammer F., Le Fevre O., 1992, ApJ, 385, 61

Salvato M., 2002, PhD thesis, Universität Potsdam

Schade D., Lilly S. J., Le Fevre O., Hammer F., Crampton D., 1996, ApJ, 464, 79

Schade D. J., Boyle B. J., Letawsky M., 2000, MNRAS, 498, 516

Schechter P., 1976, ApJ, 203, 297

Schlegel D. J., Finkbeiner D. P., Davis M., 1998, ApJ, 500, 525

Schmidt M., 1968, ApJ, 151, 393

Schmidt M., Green R. F., 1983, ApJ, 269, 352

Schneider D. P., Richards G. T., Fan X., Hall P. B., Strauss M. A., Vanden Berk D. E., Gunn J. E., et al., 2002, AJ, 123, 567

Shields G. A., 1978, Nature, 272, 706

Simien F., de Vaucouleurs G., 1986, ApJ, 302, 564

Smith E. P., Heckman T. M., Bothun G. D., Romanishin W., Balick B., 1986, ApJ, 306, 64

Starck J. L., Pantin E., Murtagh F., 2002, PASP, 114, 1051

Stetson P. B., 1987, PASP, 99, 191

Stockton A., Canalizo G., Close L. M., 1998, ApJ, 500, L121

Taylor G. L., Dunlop J. S., Hughes D. H., Robson E. I., 1996, MNRAS, 283, 930

Toomre A., Toomre J., 1972, ApJ, 178, 623

Vílchez J. M., Iglesias-Páramo J., 1998, ApJL, 506, L101

Wadadekar Y., Robbason B., Kembhavi A., 1999, AJ, 117, 1219

Weedman D. W., 1986, Quasar Astronomy, 1. edn. Cambridge astrophysics Series, Cambridge University Press, Cambridge

Wisotzki L., 1998, Astronomische Nachrichten, 319, 257

Wisotzki L., 2000, A&A, 353, 853

Wisotzki L., Christlieb N., Bade N., Beckmann V., Köhler T., Vanelle C., Reimers D., 2000, A&A, 358, 77

Wisotzki L., Köhler T., Groote D., Reimers D., 1996, A&AS, 115, 227

Wolf C., Meisenheimer K., Rix H.-W., Borch A., Dye S., Kleinheinrich M., 2003, A&A, 401, 73

Wolf C., Wisotzki L., Borch A., Dye S., Kleinheinrich M., Meisenheimer K., 2003, submitted to Astronomy & Astrophysics, astro-ph/0304072

Yagi M., Kashikawa N., Sekiguchi M., Doi M., Yasuda N., Shimasaku K., Okamura S., 2002, AJ, 123, 87

Yee H. K. C., Morris S. L., Lin H., Carlberg R. G., Hall P. B., Sawicki M., Patton D. R., Wirth G. D., Ellingson E., Shepherd C. W., 2000, ApJS, 129, 475

Acknowledgements

I would like to thank Prof. Reimers for his support and for accepting me as a member of his group.

Special thanks belong to Lutz Wisotzki for tutoring me from before my Diploma to my Doctorate, for inspiration and motivation and for successfully applying and prolonging my grant money from the Deutsche Forschungsgemeinschaft. Without his sharp and critical mind and his brilliant ideas this work would not have been feasible.

Many thanks go to Knud Jahnke for the long and fruitful cooperation and discussions. Many parts of the decomposition projects were conceived and written together with him.

I would also like to thank Eva Örndal for the nice collaboration on the adaptive optics data and the fun we have at the Observatories of Chichen Itzá or La Palma.

The first version of the decomposition method was tested (and used!) by Mara Salvato, who I wish to thank for the feed-back.

Finally I want to thank my colleagues from the Villa, namely Hans Hagen, Dieter Engels and Steffen Nehls for continuesly listening to my complaints about a certain software.